Electron Cryo-Tomography of Vitreous Cryo-Sections: Towards Imaging Biological Nanomachines in their Cellular Environment

Jason Michael Pierson

Electron Cryo-Tomography of Vitreous Cryo-Sections: Towards Imaging Biological Nanomachines in their Cellular Environment

Proefschrift

ter verkrijging van de graad van doctor
aan de Technische Universiteit Delft,
op gezag van de Rector Magnificus prof.ir. K.C.A.M. Luyben,
voorzitter van het College voor Promoties,
in het openbaar te verdedigen op woensdag 20 april 2011 om 12:30 uur

door

Jason Michael PIERSON

Bachelor of Arts
Western State College, Gunnison, Colorado, U.S.A.
geboren te Grand Junction, Colorado, de Verenigde Staten

Dit proefschrift is goedgekeurd door de promotor:
Prof. dr. P.J. Peters

Samenstelling promotiecommissie:

Rector Magnificus	Voorzitter
Prof. dr. P.J. Peters,	Technische Universiteit Delft en NKI-AVL, promotor
Prof. dr. J.J. Neefjes,	Universiteit Leiden en NKI-AVL
Prof. dr. H.W. Zandbergen,	Technische Universiteit Delft
Prof. dr. A.J. Koster,	Universiteit Leiden
Prof. dr. E.J. Boekema,	Rijksuniversiteit Groningen
Prof. dr. C. Dekker,	Technische Universiteit Delft, reservelid

Table of Contents

Be truly glad. There is wonderful joy ahead!

- I Peter 1:6

Chapter 1

Introduction

1.1 Aim of the thesis

All life forms are governed by functional units, composed of proteins, nucleic acids, and various small molecules, which interact synergistically to regulate, at the cellular systems-level, the behavior of an organism[1]. Cells and all their functional units, therefore, can be compared to an industrial factory, in which numerous macromolecular 'machines' are organized to complete the biological workload of the cell[2]. Our knowledge, unfortunately, is rather limited at the 'systems' level of cellular organization. As one would expect, elucidating or deciphering the ultra structure of these complex macromolecular functional networks, in their cellular context, is a central goal in all disciplines of biology.

The various imaging modalities of modern day biological structural determination can be seen in Figure 1.1. X-ray crystallography (XRD) and nuclear magnetic resonance (NMR) are proven imaging methods for structural feature determination in the atomic resolution and the millimeter resolution range, i.e. computerized axial tomography (CAT / CT scan) and magnetic resonance imagine (MRI). Visible-light microscopy (VLM) and conventional electron microscopy (EM) methods have been instrumental for addressing biological structures of intermediate sizes. Despite the fact that these imaging modalities span the majority of biological structures a small but important imaging gap remains.

The structural imaging gap includes large and dynamic multi-protein complexes and the details of small cellular organelles and viruses. These complexes are respectively too large or heterogeneous for XRD or NMR methods, and the wavelength of visible light limits the resolution of VLM. Figure 1.1 illustrates that high-resolution EM bridges this important imaging gap in the size spectrum for subcellular imaging at resolutions between those allowed by XRD and VLM[3].
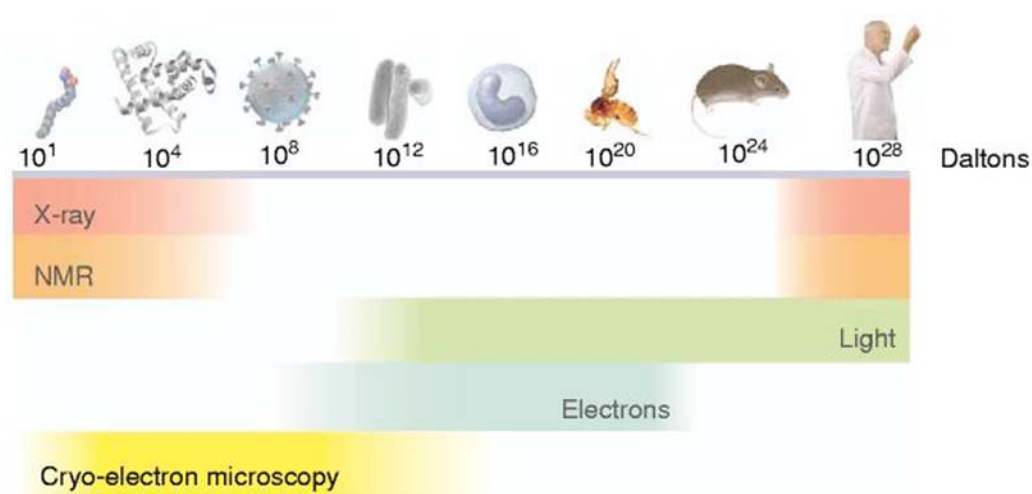
Figure 1.1: The range of imaging techniques used for visualizing objects that span from cellular molecules to humans. At one end of the spectrum are small biological entities such as lipids, proteins and whole viruses. At the other end are whole organisms like human beings. In the unified scale shown here, the sizes of all objects are described in units of 'molecular weight', Daltons. Using this scale, one can make a more standardized quantitative estimate of the relative sizes across the biological spectrum, showing, for example, that the 'molecular weight' of an adult human is about 25 orders of magnitude greater than the molecular weight of an amino acid. Reproduced from Subramaniam, 2005.

Cells are inherently three-dimensional; however, conventional EM only provides two-dimensional images. Therefore, cellular densities are superimposed along the projection direction and the resulting image lacks basic 3D information (Figure 1.2). Electron tomography[4] addresses this problem by tilting the stage of the microscope, which in turn tilts the sample, and records images from multiple angles (Figure 1.3a). These single projections at various tilts can be combined to generate a 3D volume (Figure 1.3b), albeit the reconstruction is imperfect, due to the limited range of angles that can usually be employed[5].

Figure 1.2: A drawing by John O'Brien, which appeared in The New Yorker Magazine in 1991, illustrating the projection problem. A three-dimensional object with a specific conformation, the bunny rabbit, appears as a hand in a two-dimensional projection image.
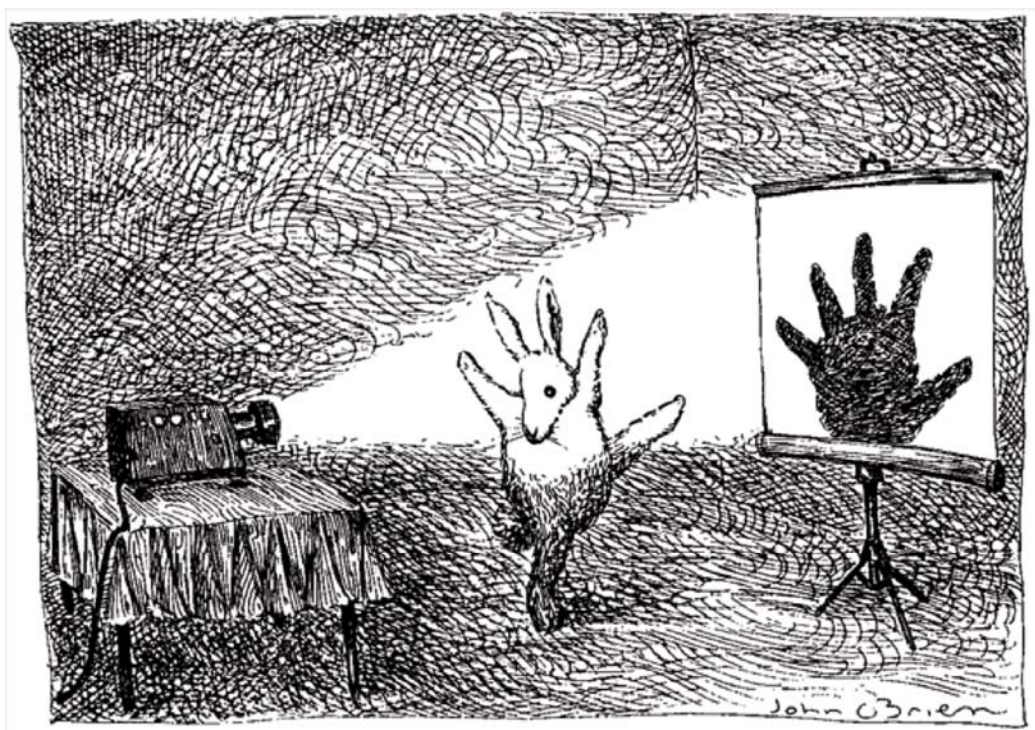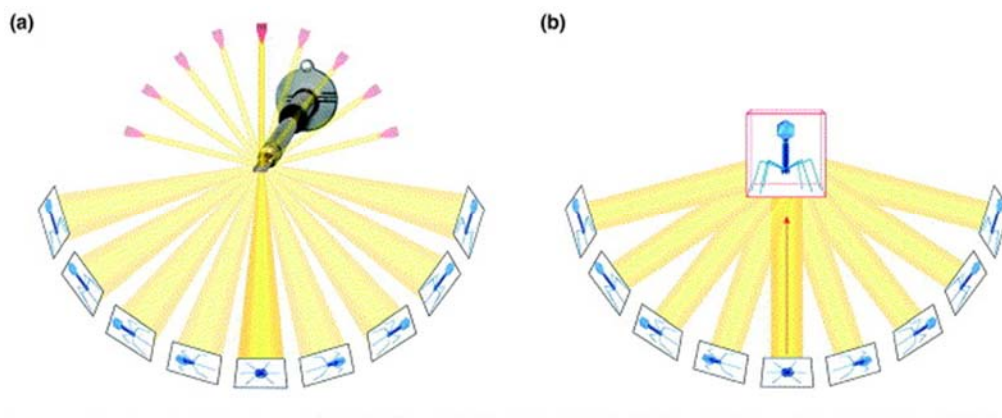
Figure 1.3: The principles of transmission electron tomography. A biological sample can be imaged in several different orientations by tilting the sample holder (a) inside the microscope and recording single projection images. Each tilted single projection image can be back projected in either real or reciprocal space to construct a three-dimensional reconstruction (b) of the original object. Reproduced from McIntosh, 2004.

The key to preserving the delicate cellular ultrastructure is to maintain a close-to-natural environment during sample preparation for EM. Conventional EM sample preparation involves cross-linking proteins and other cellular constituents with aldehydes. In addition, much of the cellular water is removed, which in turn causes a redistribution of soluble components of the cytoplasm. Finally, the sample is stained with contrast-enhancing salts like uranyl acetate to provide the necessary contrast in the EM. Because of the preparation artifacts mentioned above, cryogenic methods for sample preparation have been developed.

Cryogenic biological sample preparation for electron cryo-microscopy and tomography is at the forefront of modern biological structural analysis. Ultrarapid freezing immobilizes biological samples and ensures that they are in a close-to-native state during imaging[6]. Compared to conventional EM, which involves chemical fixation, dehydration, and staining, cryogenic sample preparation methods have

greatly improved our understanding of biological ultrastructure and macromolecular organization within a cellular context[7].

As Figure 1.1 shows, in order for the highest resolutions to be reached, cellular complexes must be isolated away from their natural environment. A staggering question remains, however, as to whether these complexes that are reconstructed, reconstituted, or isolated away from the cell reflect a natural, structural organization in living cells.

The thin film method of plunge-freezing for EM sample preparation must be limited to ~500 nm or less for proper imaging[8]. Larger cells and pieces of tissue, however, are too thick to be viewed by EM *in toto*, due to frequent plural electron scattering. The biological sample and its extracellular medium must be treated in such a way to prevent ice crystal formation. To successfully freeze large cells or pieces of tissue, the sample must be high-pressure frozen[9]. This ensures that no crystallization of intra-cellular water will occur. Preventing crystallization, which is often called "vitrification", is important because growing ice crystals may damage the ultra-structure of the cell. To achieve vitrification, the pressure is raised >1000X, which could potentially alter chemical equilibrium in cells. However, the speeds with which pressure is applied and freezing is accomplished are likely to provide reliable cryo-immmbolization.

Subsequently, the sample can be thinned for EM imaging. Figure 1.4 shows a comparison of a conventionally fixed sample (left image)[10] with a cryogenically prepared samples (right image)[11]. Notice in the chemically fixed sample that much of

the cellular ultra structure is lost due to the harsh preparation method, as we discussed

earlier, while in the frozen-hydrated preparation the ultra structure is retained.
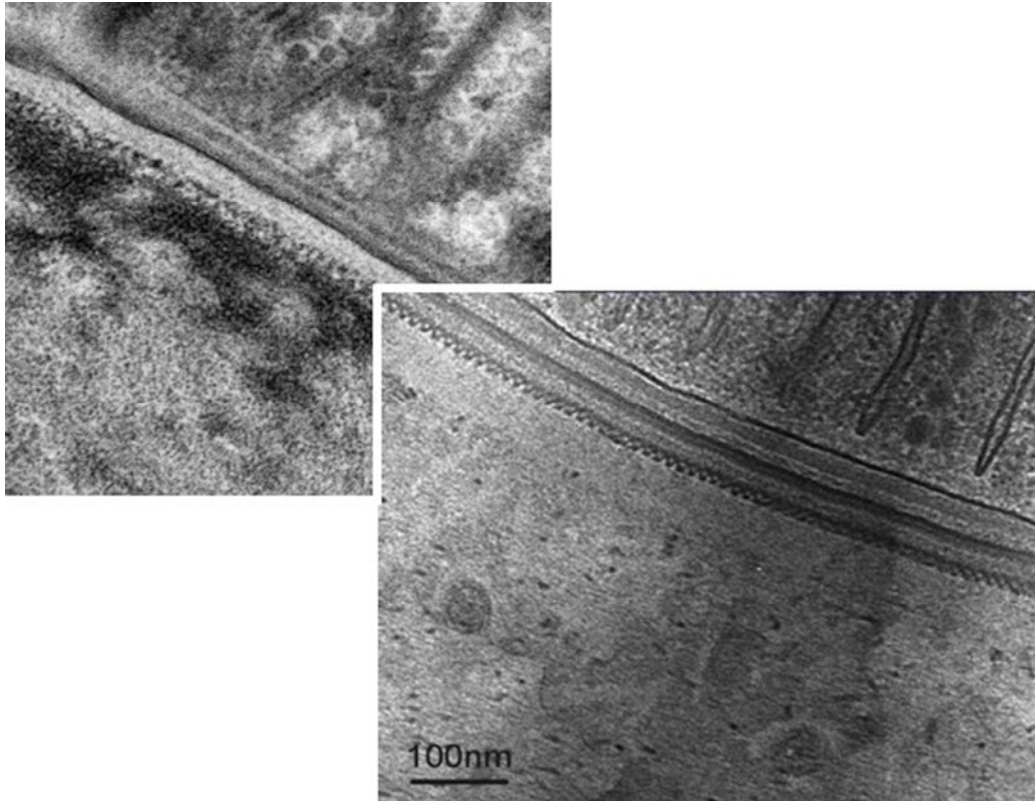
Figure 1.4: A comparison between observable cellular structural information within a conventionally prepared sample (left) and high-pressure frozen, vitreous-sectioned sample (right). Both images show a single projection image of a cyanobacteria envelope. The left image shows the limits of observable structural information using a preparation method that involves chemical fixation with aldehydes and heavy metal staining with uranyl acetate. The right image shows the structural preservation that is afforded by using vitrification to immobilize the sample.

In this thesis we have used electron cryo-tomography of vitreous cryo-sections, which is currently the most suitable technique for analyzing the spatial organization of macromolecular complexes within the cell in a close-to-native environment, to image sections of cells and their constituents.

1.2 Outline of the thesis

The first aim of this thesis is to define the most suitable EM imaging technique for looking at cells and their constituents in a *close-to-native,* cellular environment. **Chapter 2** introduces and analyzes each EM technique that can be used for cellular structural analysis. We conclude that the technique of electron cryo-tomography of vitreous cryo-sections is the most suitable technique for studying macromolecular complexes within large cells and tissue in a close-to-native, cellular environment.

In **Chapter 3** we introduce two novel technical advancements to vitreous cryo-sectioning, which in turn have made the technique more widespread and reproducible. In **Chapter 4** we address one of the main limitations of the technique – vitreous-section-induced compression. In **Chapter 5** we use these techniques to investigate the bacteriophage T7 infection process in a close-to-native state.

Finally, we provide a summary of the work done in this thesis and a future outlook for the technique of electron cryo-tomography of vitreous cryo-sectioning.

References

1. Alberts, B. 1998 The cell as a collection of protein machines: preparing the next generation of molecular biologists. *Cell* **92**, 291-294.

2. Robinson, C.V., Sali, A., Baumeister, W. 2007 The molecular sociology of the cell. *Nature* **450**, 973-982.

3. Subramaniam, S. 2005 Bridging the imaging gap: visualizing subcellular architecture with electron tomography. *Curr. Opin. Microbiol.* **8**, 316-22.

4. McIntosh J.R., Nicastro, D., Mastronarde, D. 2004 New views of cells in 3D: an introduction to electron tomography. *Trends Cell Biol.* **15**, 43-51.

5. Koster A.J., Grimm R., Typke D., Hegerl R., Stoschek A., Walz J., and Baumeister W. 1997 Perspectives of molecular and cellular electron tomography. *J. Struct. Biol.* **120**, 276-308.

6. Dubochet J., McDowall A.W., Menge B., Schmid E.N., and Lickfeld K.G. 1983 Electron microscopy of frozen-hydrated bacteria. *J. Bacteriology* **155**, 381-390.

7. Al-Amoudi A., Castaño-Díez D., Betts M.J., Frangakis A.J. (2007) The molecular architecture of cadherins in native epidermal desmosomes. *Nature* **450**,832-837.

8. Dubochet J., Adrian M., Chang J.J., Homo J.C., Lepault J., McDowall A.W., and Schultz P. 1988 Cryo-electron microscopy of vitrified specimens. *Q. Rev. Biophys.* **21**, 129-228.

9. Studer D., Graber W., Al-Amoudi A., and Eggli P. 2001 A new approach for cryofixation by high-pressure freezing. *J. Microsc.* **203**, 285-294.

10. Sleytr, U.B. and Beveridge, T.J. 1999 Bacterial S-layers. *Trends Microbiol.* **7**, 253-60.

11. Al-Amodui, A., Chang, J.J., Leforestier, A., McDowal, A., Salamin, L.M., Norlen, L.P., Richter, K., Blanc, N.S., Studer, D.S., Dubochet, J. 2004 Cryo-electron microscopy of vitreous sections. *EMBO J.* **23**, 3583-8.

Chapter 2

Towards Visualization of Biological Nanomachines in their Native

Cellular Environment

Jason Pierson[a], Musa Sani[a], Cveta Tomova[a], Susan Godsave[a], Peter J. Peters[a]

[a]Division of Cell Biology II, The Netherlands Cancer Institute – Antoni van Leeuwenhoek Hospital,

Plesmanlaan 121, 1066 CX Amsterdam, The Netherlands

Abstract

The cellular *nanocosm* is made up of numerous types of macromolecular complexes, or biological nanomachines. These form functional modules that are organized into complex subcellular networks. The majority of structural information of cellular nano-machinery has mainly been obtained by analyzing isolated structures using imaging techniques such as X-Ray crystallography, nuclear magnetic resonance imaging (NMR), or single particle electron microscopy (SPA). However, there is a strong argument towards imaging these biological complexes in a more native state and within a cellular environment and once this is achieved a more clear understanding of their function will be realized. Emerging methods in electron microscopy, specifically cryogenic sample preparation combined with electron tomography, are now making this goal attainable.

Electron cryo-tomography bypasses the need for conventional fixatives, dehydration and stains, so that a quasi-native environment in retained. As this technique is approaching macromolecular resolution, it is possible to create maps of individual macromolecular complexes. X-ray crystal structures and NMR data can be 'docked' or fitted into the lower resolution particle density maps to create a macromolecular atlas of the cell under normal and pathological conditions. The majority of cells, however, are too thick to be imaged in an intact state and therefore methods such as high-pressure freezing with freeze substitution and cryo-sectioning have been introduced for electron tomography. Here, we review technical considerations and methodology for visualizing nanomachines in a close-to-physiological and cellular context.

16

2.1 Introduction

Proteins perform key roles in the majority of cellular functions. They also serve as building blocks for larger heterogeneous macromolecular assemblies, or biological nanomachines, which are organized into cellular 'modules'[1]. As the name implies, a biological machine is analogous to the man-made version. Both are made of individual components that function in a coordinated fashion to perform specific functions. In nature, if any single structural component of a nanomachine malfunctions the result is often a disease. Discerning the ultrastructure of a biological machine and its components within the cell can contribute to an understanding of how it functions both normally, and in disease. Little is known, however, about the details of how these macromolecular machines are spatially organized within their cellular environment.

X-ray crystallography and NMR approaches have been used to complement genetics, biochemistry, and proteomics to characterize the overall structural organization of individual protein complexes. Most macromolecules, however, cannot be crystallized, or when crystallized they diffract poorly because only large well-ordered crystals diffract. In the case of NMR, the size of the protein complex is limited to approximately < 100 kDa[2]. In order to study biological machines where they normally reside, and not as isolated entities, then more suitable imaging techniques, such as Transmission Electron Microscopy (TEM) and/or Electron Tomography (ET), need to be adapted.

TEM is one of the most powerful techniques for ultra-structural studies of the cell and its constituents[3]. When performed on sections of fixed cells and tissues, it has been invaluable in establishing a picture of the sub cellular arrangement of organelles and determining the localization of gene products with immunogold labeling techniques. Recently, the route of *tubercles bacillus* infection was demonstrated using immunogold labeling on aldehyde fixed cryosections in which the findings revealed a pathway that is against the current textbook dogma[4]. But, this technique makes use of fixed, dehydrated and heavy metal-stained material, which artifacts may be introduced at all stages[5]. Recently, there has been an important focus on optimal TEM sample preservation for high-resolution structural studies of macromolecules *in situ*. This quest to find the true relation between molecules, linked into supramolecular complexes and assembled into an intricate network of cellular compartments, is revolutionizing modern TEM. The catalyst for this revolution has been Cryo-EM and ET[6,7]. ET is used to generate three-dimensional maps from a series of two-dimensional images. The specimen is rotated with respect to the imaging source; in this case electrons and a series of projection images are recorded over a limited angular range (usually -70° to +70°).

Cryo-ET is based on a freezing technique that captures the cellular water in an amorphous (glass-like) layer in which all cellular components are embedded. This process is known as vitrification, which is achieved by the ultrarapid freezing of a thin biological sample, circumventing all harsh chemical fixatives and heavy metal stain.

Here we analyze different EM imaging procedures that have the ultimate goal to visualize macromolecular 'machines' in the most natural environment currently

possible. Using a variety of imaging techniques, structural information can be extracted at different resolution levels. This information can be combined to create a multiresolution density map of the individual macromolecular complexes; eventually leading to a catalogue of all biological nanomachines that can be used to search in 3D volumes[8] of cells, and to determine the spatial organization of individual complexes within their cellular environment[9]. In addition we provide insight on the techniques that will likely play an important role in achieving the goal to mapping macromolecular machines within their cellular context.

2.2 Single Particle Analysis

Electron microscopy (EM) has provided important structural information about protein complexes essential for describing their functional organization. Single particle analysis (SPA) has been used to determine the structure of a variety of macromolecules and biological nanomachines. This involves the analysis of images from large numbers of purified macromolecular particles that have been placed on an EM grid. These images are used to build up a three-dimensional model of the protein complex.

2.2.1 Sample Preparation

For SPA, a convenient isolation approach is to 'fish' the nanomachines out from their cellular environment using a tag that targets a single component of the complex, most importantly in a single step[10]. Negative staining is often the first step to check for quality and suitability. The sample is embedded in heavy metal salts, such as uranyl

acetate or phosphotungstic acid, providing a contrasting agent for the weakly electron scattering biological molecules. This staining has been part of the most commonly used EM preparation methods since its introduction 50 years ago[11]. An example can be seen in (Fig. 2.1) that shows a negatively stained *Shigella flexneri* needle appendage. The averaged projection view shows the basal part of the needle complex, composed of several rings that traverse the cell envelope. The heavy metal stain, however, creates a cast around the surface of the specimen. Moreover, dehydration of the specimen can potentially alter fine structural details. It also imposes a resolution limit of 10–20 Å[12,13]. These limitations have been overcome by cryo-fixation, or embedding of the specimen in vitreous water[6].

2.2.2 Image Analysis

Irrespective of the sample preparation method, individual particles must be aligned and averaged to improve the signal. For cryo-preparation methods the averaged particle contains information to atomic resolutions,[14,15] but suffers from limited contrast. The imaging electron dose is limited (low-dose imaging) to 10-20 electrons/Å[16,6] to reduce the number of inelastically scattered electrons[17] that often lead to radiation damage. To overcome this problem, single particle image enhancement programs have been developed[18,19] to average large numbers of copies of single particles and improve the signal-to-noise ratio.
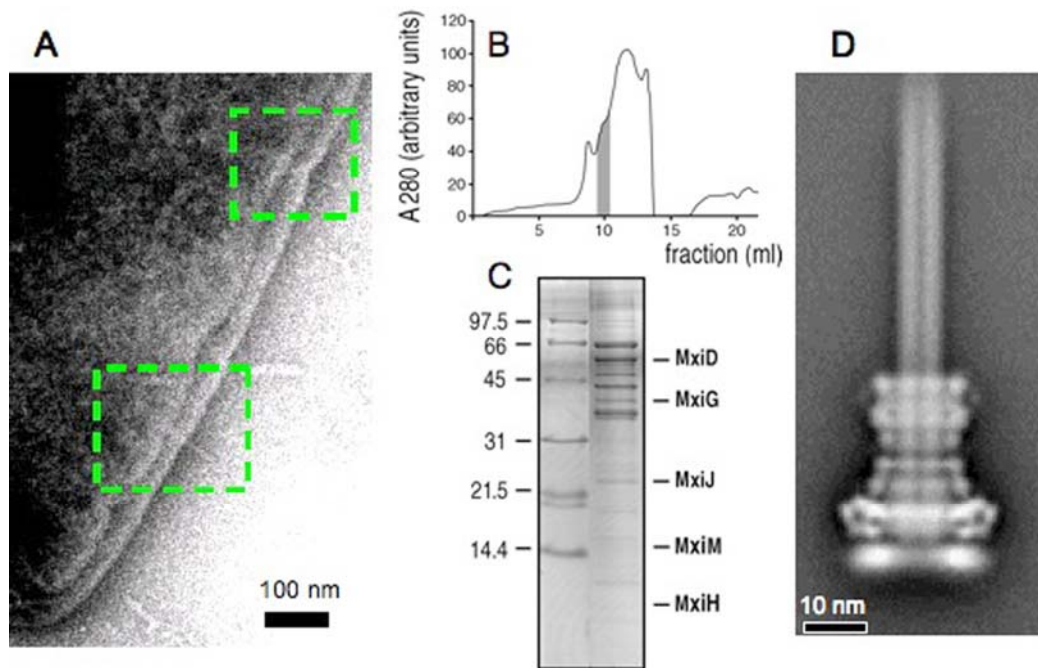
Figure 2.1: From a whole cell to isolated complexes. (A) Electron micrographs of osmotically shocked *S. flexneri* exhibiting the type III secretion system protruding through the bacterial envelope (see boxed area). (B) Gel chromatography of solubilized secretion complexes from the bacterial envelope. (C) The fraction containing enriched complex is checked by SDS and individual bands identified by mass spectrometry. (D) 2D projection average of 1500 isolated needle complexes composed of a hollow needle appendage (indicated by a stain-penetrated line along its axis) and a basal part of several rings that traverse the cell envelope. The channel that runs through the needle appendage is 2-3 nm in diameter indicating that substrates that exit the conduit do so in an unfolded state.

The first step in the averaging procedure is to identify individual particles within the micrograph manually or by using semi-automated computer programs. Particle alignment then modifies the rotational and translational position of each particle, such that all particles have a comparable orientation and key features will become visible. Since the resolution depends on the accuracy of the particle alignment, there must be sufficient particle feature recognition in a noisy image. Larger complexes are easier to align and subsequently process. A minimum particle size of 1000 kDa is therefore desired for proper alignment[14]. The more particles used in the reconstruction, the

higher the resolution of the final model. The technique is most powerful when the particles display intrinsic icosahedral[20], helical[21], or crystalline symmetry[22], that in certain instances such as polyhedrosis virus[23], aquaporin-1[24,25] and of the bacterial flagellum[26] have reached atomic resolution.

Asymmetric complexes still remain challenging to image using single particle analysis. The ribosome, which is one of the most analyzed low symmetry single particles, is an exception. It has served for many years as test specimen in the development of many single particle techniques[27]. Although the resolution is lower for such asymmetric particles, a quantitative description, on the quaternary level, is nevertheless possible.

2.3 Visualizing Nanomachines in their Cellular Context

A drawback with the single particle technique is that the nanomachines may undergo changes during isolation, such as loss of labile components, or certain conformational states may be favored. Furthermore, there are many macromolecular assemblies associated with membranes, which should be studied without extraction and in a cellular context.

Specimen preservation is one of the most critical steps in the entire process of native cellular imaging. Cellular water in liquid form is incompatible with the vacuum of the EM. Water is the most abundant cellular constituent and therefore important for preserving cellular ultra-structure. Currently the only way to fix cellular constituents without introducing significant structural alterations is by cryofixation. To be

successful, the freezing process has to be ultra-rapid in order to avoid ice crystal formation, which damages cellular material and can hinder imaging. There are currently two common methods employed; plunge freezing into liquid ethane[6] and high pressure freezing (HPF)[28].

2.3.1 Cryofixation

The plunge freezing technique is suitable for samples with limited thickness [i.e. bacteria, isolated cellular organelles[29] or viruses] or relatively thin regions of larger cells[30]. The physical properties of water, namely its poor heat conductivity, are the reason that freezing is limited for large cells and tissues. Currently, the only method to vitrify thicker samples (up to 200µm) is by HPF.

High pressure, introduced at the moment of freezing, lowers the freezing point of water. Synchronized pressurization and cooling of the sample takes place within 20 ms[31]. The development of these machines has allowed samples of various thicknesses to be vitrified. In general, cryo-fixation has two distinct advantages over chemical fixation. It is achieved within milliseconds and it ensures simultaneous immobilization of all macromolecular components. Many protein networks are very labile and fall apart with the slightest osmotic or temperature change and these unwanted effects are minimized during cryo-fixation. These techniques allow the study of biological samples with improved ultrastructural preservation, and can facilitate the study of dynamic processes.

2.4 Freeze Substitution

Achieving optimal preservation of the biological sample is undoubtedly critical, but still only the first step in visualizing it. Until it was demonstrated that vitreous water could be sectioned and cellular structure visualized directly in the cryo-TEM, the only way to examine the cryo-fixed sample was by embedding it in resin for sectioning. For this the vitrified water in the HPF frozen specimen must be replaced by an organic solvent in a process known as freeze-substitution (FS).

Freeze substitution is a process of dehydration, performed at temperatures low enough to avoid the formation of ice crystals and to circumvent the damaging effects observed after ambient temperature dehydration. Aggregation of macromolecules in organic solvents and changes of the hydration shell surrounding the biological molecules can occur even at very low temperatures, but it is reasonable to assume that cryo-substitution at temperatures below a specific threshold preserves the hydration shell[32,33]. Further, the total or partial loss of the hydration shell can be reduced during the cryo-embedding procedure, so minimizing aggregation and the redistribution of diffusible elements[34,35].

Freeze substitution combines instant physical immobilization of the cell constituents and resin embedding. Once substitution is complete, samples are gradually warmed-up and processed further as for conventionally prepared samples. Successful cryo-fixation followed by freeze-substitution shows superior preservation of fine structure compared to chemical fixation techniques[36,37]. This technique also gives the possibility of examining thick (200-300 nm sections) samples by ET, so that relatively

large cellular volumes can be studied in three dimensions. This approach is very beneficial for an understanding of the complex relation between different cellular organelles and randomly occurring events. Membrane contact sites between the ER and the outer-most membrane of the apicoplast (a plastid found in most parasites from *Apiconplexa Toxoplasma gondii* and *Plasmoduim* species) can be seen in Fig. 2.2 as an example of a sample that has been freeze substituted in 0.1% uranyl and embedded in Lowicryl HM20[38].
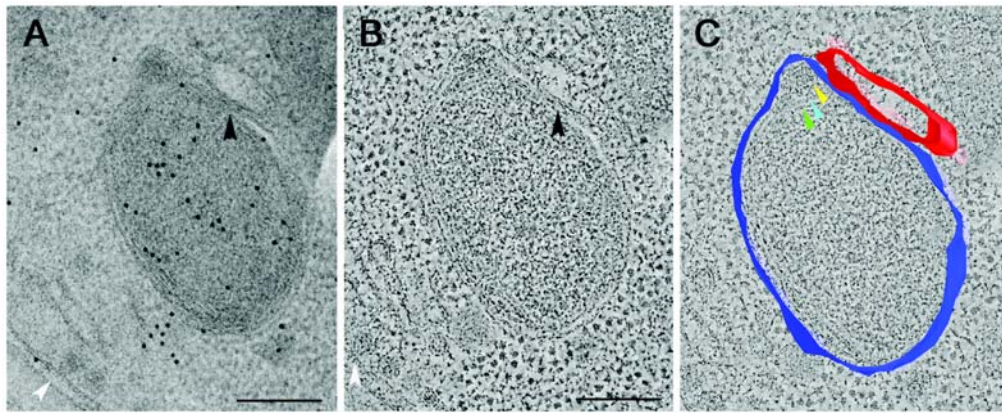
Figure 2.2: Images illustrating the relation between the ER and the apicoplast outermost membrane from high-pressure frozen and freeze substituted samples. (A) Single projection image from an aligned stack acquired from a thick section (200 nm), at -35 degree tilt. The gold particles, also used for alignment of the tilt series, are specific labeling for the apicoplast *acyl* carrier protein. The relation between the membranes of the ER and the apicoplast is shown (black arrowhead). *Scale bars* 100 nm. (B) Optical slice from a tomographic reconstruction. The lamellar structure of the membranes is visible (highlighted in (C). This image has also captured a budding vesicle from the nuclear envelope (white arrowhead). (C) An IMOD[39] model generated from the tomographic reconstructions shown in b that displays the ER (red) and the outermost membrane of the apicoplast (blue). The other three membranes are indicated by coloured arrowheads: green and light blue respectively for the innermost two membranes; yellow for the periplastid.

In addition, Fig. 2.2 shows the potential of high pressure freezing – freeze substitution (HPF/FS) in combining optimal structural preservation with protein detection. There are numerous examples where HPF/FS combined with ET have changed our understanding of cellular structure and dynamics[40,41,42,43,44,45]. Recently, it was shown that cellular fibrils connect protofilaments directly to the inner kinetochore[46], which nicely illustrates a mechanism for directly harnessing microtubule dynamics for chromosome movement.

Even though numerous different substitution protocols exist, there are only a few methodological investigations concerning the process of freeze-substitution, such as the replacement of ice by an organic solvent at temperatures of -90°C to 0°C[47], the substitution capacities of different organic solvents in the presence of water[48], and the influence of the different solvents on the ultra-structural preservation of high-pressure frozen, freeze-substituted samples[49]. It is still arguable what alterations of the cellular structure are induced and to what extent the information obtained can be considered as an accurate representation of the living cell, especially in the case of the 3D structure of macromolecules.

2.5 Vitreous Cryo-Sectioning

The expansion and development of electron cryo-tomography and cryo-sectioning of native vitreous samples, such as yeast and bacteria, has made visualizing cells directly in the absence of chemicals, heavy metals and hypertonic cryo-protectants possible. Vitreous cryo-sections of *Saccharomyces cerevisiae* (Fig. 2.3) showed that the nuclear envelope forms a unique membrane contact site with the vacuole, called the

nucleus-vacuole (NV) junction[50]. 'Velcro' like protein-protein interactions holds the junction in place. The proteins involved are Vac8 in the vacuole membrane, which is associated with Nvj1 in the outer nuclear membrane. NV junctions are the sites of piecemeal microautophagy of the nucleus (PMN), which is a type of autophagy that targets portions of the nucleus. One of the problems associated with the vitreous cryo-sectioning technique is the presence of knife-induced surface artifacts, called crevasses. An example of this is shown in Fig. 2.3b, where crevasses are partially visible in the vacuole (V) as white stripes perpendicular to the cutting direction (parallel to the NV junction). In certain cases crevasses can penetrate into the depths of the vitreous cryo-section and affect the underlying biological ultrastructure, however, in ultra-thin sections (< 50 nm) these artifacts appear to be non-intrusive to the biological ultra-structure.

Artifacts induced by the process of sectioning (knife marks, crevasses, and compression) have been described in detail and must be taken into consideration[51]. It is possible to minimize knife marks and crevasses, making compression the most problematic artifact. Compression is a deformation that makes the vitreous section shorter along the cutting direction without changing the overall volume. The result is an increase in overall section thickness. Thirty percent compression within vitreous cryo-sections is not unusual. If compression is evenly distributed, then a reverse transform[51] can be applied to the entire volume post-reconstruction. We have seen indications, however, that compression is non-homogeneous in filament bundles[52], microtubules[53], desmosomes[54], and bacterial chemotaxis receptors[55]. On the biological nanomachine level, the affect of these artifacts is uncertain, but could be minimal for rigid, macromolecular machinery (see Chapter 4).
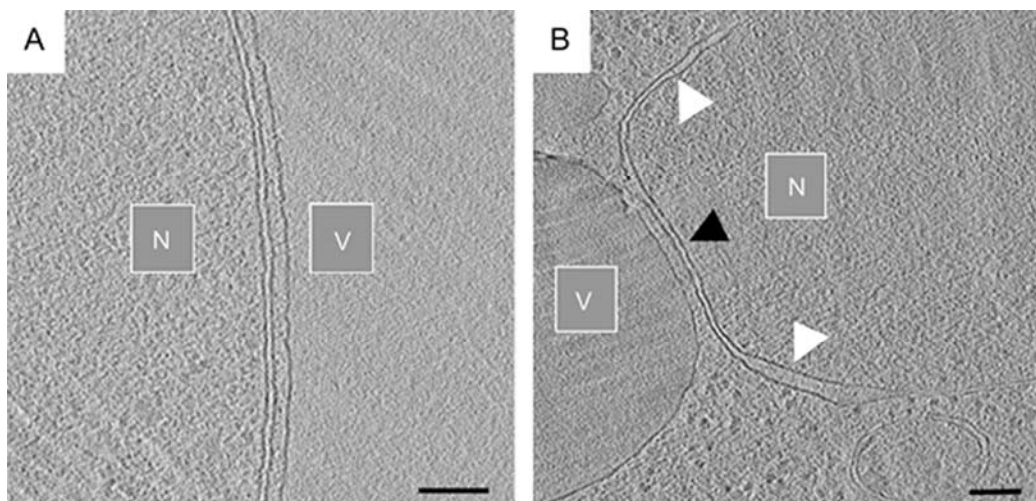
27

Figure 2.3: Tomography of thin vitreous cryo-sections of the *Saccharomyces cerevisiae* nucleus-vacuole junction. (A) A 10 nm slice from a reconstruction that shows the consistent width of the nuclear membranes in relation to the vacuole. 'N' denotes the nucleus and 'V' the vacuole. *Scale bars* 50 nm. (B) A second reconstruction that shows more of an overview of the region of the NV junction. The inner and outer membranes of the bulk nuclear envelope (white arrows) are further apart compared to those of the nuclear envelope at the NV junction. Around and within the nucleus, macromolecular complexes can be observed, along with a mitochondrion at the bottom of the image.

In addition, extreme caution must be taken during image acquisition. Beam induced alterations in the sample are well-known to be a problem and are often believed to be the rate limiting step for achieving optimal electron cryo-microscopy. It is no secret that vitreous sections 'flow' during image acquisition[56,57], which is considered by some researchers to be due to local charge accumulation and/or radiochemical processes. Therefore it is important to 'learn' how to read vitreous sections with respect to structural integrity and preservation[58]. A common practice is to acquire a single projection image, using a very low electron dose, before a tilt series is collected, and then compare it to an image taken after the series is complete. If there is no noticeable change, then the structural integrity of the vitreous section has been

maintained. If the final image appears 'smooth' (with no knife marks and/or crevasses visible) then the ultrastructure of the cell must be analyzed with caution. Map montaging helps to reduce the 'overhead' electrons used to pinpoint an area of interest before acquiring a tilt series. In order to preserve the vitreous section integrity, the electron beam dose is restricted, which in turn limits the contrast levels and the signal-to-noise ratio. This makes subsequent analysis of such images rather difficult.

The application of tomography of vitreous sections is the future of cellular imaging, combining close-to-native preparation techniques with a three-dimensional view of the vitreous section. The ultimate goal is to map complex macromolecular machines within 3D slices of large cells and tissue. An example is shown of a sample of *S. cerevisiae* that was immobilized in a copper tube using HPF. The sample was vitreous cryo-sectioned into thin (50 nm) slices and observed using electron cryo-tomography (Fig. 2.4).

Within the volume of the reconstruction, individual macromolecular complexes can be observed (Fig. 2.5). Based on their size and distribution we assume that these are native 80S ribosomes in various conformational states, which can also be associated with a variety of protein complexes that aid in protein translation. The true identity, however, remains subjective until a suitable labeling or correlative approach is developed for the vitreous cryo-sectioning.
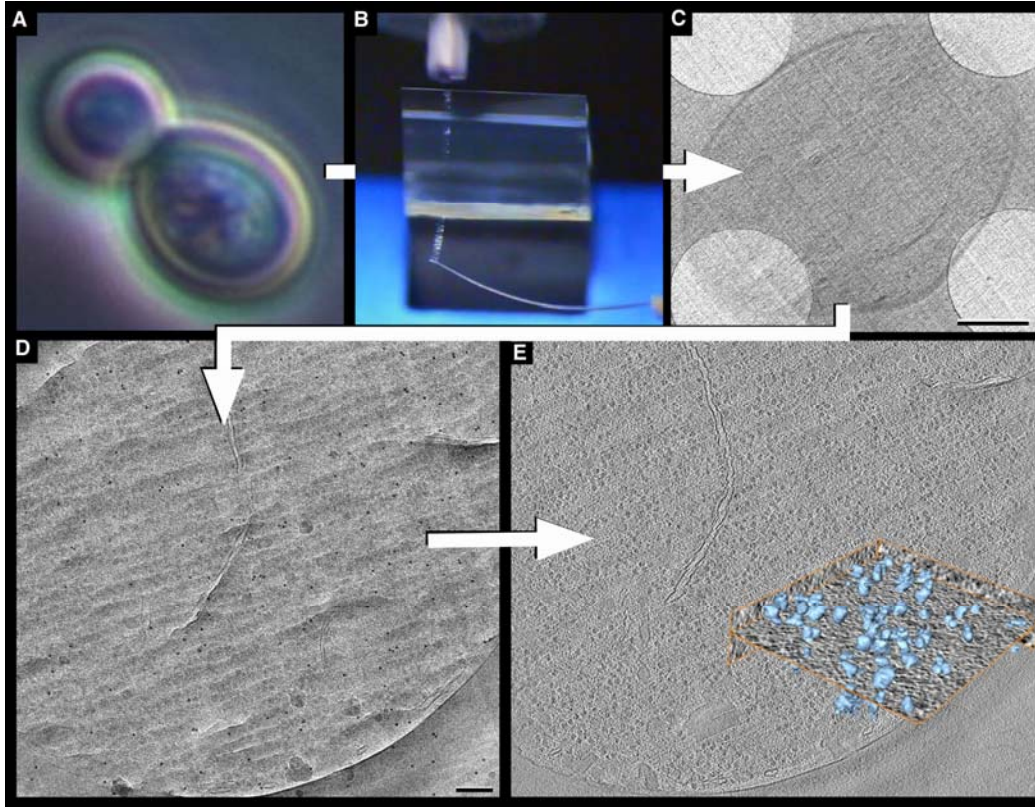
Figure 2.4: A diagram illustrating the Vitreous Cryo-Sectioning technique. (A) A confocal laser image of *S. cerevisiae* (Dr. Maxim Zakhartsev and Doris Petroi, International University Bremen, Germany). The cells are rapidly frozen by high pressure freezing (HPF) in copper tubes and then sliced (B) into very thin (50 nm) vitreous cryo-sections. (B) A relatively long ribbon of vitreous cryo-sections is held by the operator and pulled away from the diamond knife. The ribbon is placed on an EM grid and imaged by Cryo EM and ET. (C) A medium magnification single image showing a 50 nm vitreous slice of a single *S.cerevisiae* cell. *Scale bar* 2 μm. Asterisks denote holes within the carbon support film of an EM grid. Subsequent cryo-ET is shown in (D-E). (D) A single 2D projection image from a tilt series. It is difficult to interpret such images due to the projection problem of overlapping structures, along with a low signal-to-noise ratio and contrast levels. *Scale bar* 100 nm. (E) Multiple single projection images can be aligned and reconstructed into a 3D volume. A 5 nm slice from a reconstructed volume. In this image the cellular environment can be visualized well, better than within the single projection image (D). The inset displays a selected area (orange-bounded box) from the tomographic reconstruction (E).
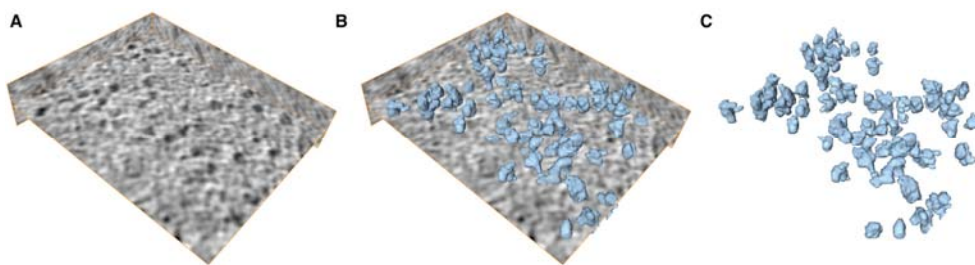
Figure 2.5: Charting Macromolecular Machines within a Vitreous Cryo-Section. (A) A selected area (orange-bounded box in Fig. 2.4D) from a tomographic reconstruction. (B-C) The volume has been surface rendered in order to visualize the cellular organization of macromolecular complexes within a thin vitreous cryo-section from a whole *S.cerevisiae*

2.6 The Future of Charting Nanomachinary in a Native Cellular Context

We have witnessed light microscopy breaking the diffraction barrier, and in the future the spatial resolution will only improve with the development of super resolution light microscopes. Recently it became clear that the green fluorescent protein (GFP) tag has a 10-50 times better signal to noise ratio at cryogenic conditions because of reduced photo-bleaching. In combination with EM, correlative cryo LM-EM offers a promising opportunity to investigate cellular organization[59,60,61]. Rather than using a single GFP tagged construct, a circular string of 5 GFP's in tandem could be constructed that would be visible in the rather noisy and low contrast cryo-ET images. In addition, the GFP could be coupled to ferritin or another analogue electron dense molecule to provide a label for cryo approaches.

High-resolution structures produced by X-ray crystallography or NMR can be fitted or docked into lower resolution EM images to create a multiresolution map of the protein structure. Such bridging techniques will be instrumental in providing a more

complete understanding of the structure and function of molecular complexes than is possible with a stand-alone technique.

Recently, volumetric averaging, which is based on the single particle averaging techniques presented, was applied to isolated organelles[29] and to cellular protein complexes involving cadherins in epidermal desmosomes of native skin[54]. In the latter case, a high-resolution X-ray crystal structure was placed into the lower resolution cadherin EM map, which resulted in a multi-resolution map of the cadherin in native epidermal desmosomes.

2.6.1 'Cutting Edge' Technology

The only way to look inside large cells and tissue, at a close-to-native preservation, is by high pressure freezing and vitreous sectioning for cryo EM. The diamond knife and accessory tools used for cryo-sectioning are improving, which will tremendously improve both the quality of the vitreous sections and subsequently the quality of the imaging. We foresee that in the near future we will use robotics for section manipulation to make handling even more convenient. An alternative approach to mechanical sectioning is based on focused ion beam milling[62]. A futuristic 'nano-knife' has also been proposed[63] constructed from multi-walled carbon nanotubes. In the future these techniques may be able to reduce the distortions currently caused by mechanical vitreous sectioning with a diamond knife, but at the current state are rather technically demanding and in development.

2.6.2 The Future of Electron Cryo-Tomography

The current, rather conservative, approximation of the resolution limit of 4-5 nm is expected to improve as the need for high-resolution structural information steadily increases. The electron source is a suitable starting point for improvement. We have witnessed a dramatic increase in spatial coherence of electrons using a field emission electron gun (FEG) rather than a LaB6 or tungsten filament. As the field emission gun improves, the induced specimen damage will be further minimized and the resolution may improve.

Contrast is generated differently with unfixed, unstained material. The objective lens is defocused creating phase contrast. By defocusing the objective lens, the contrast transfer function is altered and for high resolution studies it will need to be accurately assessed through the volume of single projection images, which is not trivial compared to single projection images. A comparison between CTF corrected and uncorrected can be seen in chromosome arrangement within mitotic HeLa cell sections[64].

Electron detectors for image collection are also becoming more sophisticated. The problem of electrons backscattering from the fiber optic plate into the scintillating layer of a charge couple device (CCD) in current detectors can be partially solved by direct detection of electrons rather than relying on a scintillating layer[65]. Remote microscopy control will soon allow users from around the world to operate and control microscopes in a completely different part of world. We have seen that the loading of cryo samples has now become completely automatic thanks to the

autoloader (FEI, Eindhoven). Millions of particles taken from several EM grids under cryogenic conditions can be imaged and processed automatically in a short period of time. This trend should not be limited to imaging but also to the sample preparation.

In the past two decades, scientific challenges in physics, chemistry, and molecular cell biology have moved towards the molecular, nanometer-scale domain. Nanoscience, once only a discipline of theoretical subjects, has now been established as a vibrant multidisciplinary area of research and development.

2.7 Summary

The cell is composed of a highly organized network of macromolecular machines addressing the demanding requirements of a living cell. Imaging these 'nanomachines' in a cellular, close-to-native state is not a trivial task. Isolation techniques will continue to be essential in solving the structures of these types of protein complexes by the "divide and conquer" method[66]. For analysis of these nanomachines in a normal environment, rapidly freezing the cell, and cellular elements, in a vitreous layer of water is currently the only technique that retains a physiological state of the organism or cells before EM imaging. As we have seen[29], unmatched structural information can be obtained. Using vitreous cryo-sections, cryo-ET can be extended to any cell and almost all tissue. Yet, one major limitation is the proper vitrification under physiological conditions and the localization of each macromolecular complex, along with their binding partners, throughout the thickness of the vitreous cryo-section. As the field of cellular imaging of nanomachines continues to evolve, we are certain to gain invaluable cell biological insights and we

are also likely to see many nanotechnology applications that utilize these elegant cellular machines.

Acknowledgements

References

1. Alberts B. 1998 The cell as a collection of protein machines: preparing the next generation of molecular biologists. *Cell* **92**, 291-294.

2. Wider G., Wuthrich K. 1999 NMR spectroscopy of large molecules and multimolecular assemblies in solution. *Curr. Opin. Struct. Biol.* **9**, 594-601.

3. McIntosh J.R. 2001 Electron microscopy of cells: a new beginning for a new century. *J. Cell Biol.* **153**, 25-32.

4. van der Wel N., Hava D., Houben D., Fluitsma D., van Zon M., Pierson J., Brenner M., Peters P.J. 2007 *M. tuberculosis* and *M. leprae* translocate from the phagolysosome to the cytosol in myeloid cells. *Cell* **129**,1287-98.

5. Peters P.J. and Pierson J. 2008 Immunogold labeling of thawed cryosections. *Methods Cell Biol.* **88**, 131-49.

6. Dubochet J., Adrian M., Chang J.J., Homo J.C., Lepault J., McDowall A.W., Schultz P. 1988 Cryo-electron microscopy of vitrified specimens. *Q. Rev. Biophys.* **21**, 129-228.

7. Lucic V., Leis A., Baumeister, W. 2008 Cryo-electron tomography of cells: connecting structure and function. *Histochem. Cell Biol.* **130**, 185-96.

8. Bohm J., Frangakis A.S., Hegerl R., Nickell S., Typke D., Baumeister W. 2000 Toward detecting and identifying macromolecules in a cellular context: template matching applied to electron tomograms. *Proc. Natl. Acad. Sci. USA* **97**, 14245-14250.

9. Nickell S., Kofler C., Leis A.P., Baumeister W. 2006 A visual approach to proteomics. *Nat. Rev. Mol. Cell Biol.* **7**, 225-230.

10. Kelly D.F., Dukovshi D., Walz T. 2008 Monolayer purification: a rapid method for isolating protein complexes for single-particle electron microscopy. *Proc. Natl. Acad. Sci. USA* **105**, 4703-8.

11. Brenner S., Horne R.W. 1959 A negative staining method for high-resolution electron microscopy of viruses. *Biochim. Biophys. Acta.* **34**, 103-110.

12. Amos L.A., Henderson R., Unwin P.N. 1982 Three-dimensional structure determination by electron microscopy of two-dimensional crystals. *Prog. Biophys. Mol. Biol.* **39**, 183-231.

13. Sani M., Allaoui A., Fusetti F., Oostergetel G.T., Keegstra W., Boekema E.J. 2007 Structural organization of the needle complex of the type III secretion apparatus of Shigella flexneri. *Micron* **38**, 291-301.

14. Henderson R. 1995 The potential and limitations of neutrons, electrons and X-rays for atomic resolution microscopy of unstained biological molecules. *Q. Rev. Biophys.* **28**, 171-193.

15. van Heel M., Gowen B., Matadeen R., Orlova E.V., Finn R., Pape T., Cohen D., Stark H., Schmidt R., Schatz M., Patwardhan A. 2000 Single-particle electron cryo-microscopy: towards atomic resolution. *Q. Rev. Biophys.* **33**, 307-369.

16. Glaeser R.M., Taylor K.A. 1978 Radiation damage relative to transmission electron microscopy of biological specimens at low temperature. *J. Microsc.* **112**, 127–138.

17. Stark H., Zemlin F., Boettcher C. 1996 Electron radiation damage to protein crystals of bacteriorhodopsin at different temperatures. *Ultramicroscopy* **63**, 75–79.

18. van Heel M., Harauz G., Orlova E.V., Schmidt R., Schatz M. 1996 A new generation of the IMAGIC image processing system. *J. Struct. Biol.* **116**, 17-24.

19. Frank J., Radermacher M., Penczek P., Zhu J., Li Y., Ladjadj M., Leith A. 1996 SPIDER and WEB: processing and visualization of images in 3D electron microscopy and related fields. *J. Struct. Biol.* **116**, 190-199.

20. Bottcher B., Wynne S.A., Crowther R.A. 1997 Determination of the fold of the core protein of hepatitis B virus by electron cryomicroscopy. *Nature* **386**, 88-91.

21. Miyazawa A., Fujiyoshi Y., Unwin N. 2003 Structure and gating mechanism of the acetylcholine receptor pore. *Nature* **423**, 949-955.

22. Henderson R., Baldwin J.M., Ceska T.A., Zemlin F., Beckmann E., Downing K.H. 1990 Model for the structure of bacteriorhodopsin based on high-resolution electron cryo-microscopy. *J. Mol. Biol.* **213**, 899-929.

23. Yu X., Jin L., Zhou Z.H. 2008 3.88Å structure of cytoplasmic polyhedrosis virus by cryo-electron microscopy. *Nature* **453**, 415-419.

24. Murata K., Mitsuoka K., Hirai T., Walz T., Agre P., Heymann J.B., Engel A., Fujiyoshi Y. 2000 Structural determinants of water permeation through aquaporin-1. *Nature* **407**, 599-605.

25. Engel A. 2003 Robert Feulgen Lecture. Microscopic assessment of membrane protein structure and function. *Histochem. Cell Biol.* **120**, 93-102.

26. Yonekura K., Maki-Yonekura S., Namba K. 2003 Complete atomic model of the bacterial flagellar filament by electron cryomicroscopy. *Nature* **424**, 643-650.

27. Stark H. 2002 Three-dimensional electron cryomicroscopy of ribosomes. *Curr. Protein Pept. Sci.* **3**, 79-91.

28. Studer D., Graber W., Al-Amoudi A., Eggli P. 2001 A new approach for cryofixation by high-pressure freezing. *J. Microsc.* **203**, 285-294.

29. Nicastro D., Schwartz C., Pierson J., Gaudette R., Porter M.E., McIntosh J.R. 2006 The molecular architecture of axonemes revealed by cryoelectron tomography. *Science* **313**, 944-8.

30. Medalia O., Weber I., Frangakis A.S., Nicastro D., Gerisch G., Baumeister W. 2002 Macromolecular architecture in eukaryotic cells visualized by cryoelectron tomography. *Science* **298**, 1155-7.

31. Studer D., Humberl B.M., Chiquet M. 2008 Electron microscopy of high pressure frozen samples: bridging the gap between cellular ultrastrucutre and atomic resolution. *Histochem. Cell Biol.* **130**, 877-89.

32. Hobot J.A., Villiger W., Escaig J., Maeder M., Ryter A., Kellenberger E. 1985 The shape and fine structure of the nucleoid observed on sections of ultrarapid frozen and cryosubstituted bacteria. *J. Bacteriol.* **162**, 960-971.

33. Kellenberger E. 1991 The potential of cryofixation and freeze substitution: Observations and theoretical considerations. *J. Microsc.* **163**, 183-203.

34. Edelman L. 1991 Freeze-substitution and the preservation of diffusible ions. *J. Microsc.* **161**, 217-228.

35. Quintana C., Lopez-Iglesias C., Laine-Delaunay M.C. 1991 (3-Cryo) methods (cryofixation, cryosubstitution and cryoembeddingding) for processing of tissues for ultrastructural and immunocytochemical studies. Application to oviduct cells of laying quail. *Biol. Cell* **72**, 167- 180.

36. Müller M. 1992 The integrating power of cryofixation-based electron microscopy in biology. *Acta. Microscopica* **1**, 37-44.

37. Steinbrecht R.A., Müller M. 1987 Freeze-substitution and freeze-drying. Cryotechniques in Biological Electron Micoscopy. Springer-Verlag, Berlin, Heidelberg, pp 149-172.

38. Tomova C., Humbel B.M., Geerts W.J.C., Entzeroth R., Holthuis J.C.M., Verkleij A.J. 2009 Membrane Contact Sites between Apicoplast and ER in Toxoplasma gondii Revealed by Electron Tomography. *Traffic* **10**, 1471-80.

39. Kremer J.R., Mastronarde D.N., McIntosh J.R. 1996 Computer visualization of three-dimensional image data using IMOD. *J. Struct. Biol.* **116**, 71-76.

40. Marsh B.J., Mastronarde D.N., Buttle K.F., Howell K.E., McIntosh J.R. 2001 Organellar relationships in the Golgi region of the pancreatic beta cell line, HIT-T15, visualized by high resolution electron tomography. *Proc. Natl. Acad. Sci. USA* **98**, 2399-2406.

41. Murk J.L., Posthuma G., Koster A.J., Geuze H.J., Verkleij A.J., Kleijmeer M.J., Humbel B.M. 2003 Influence of aldehyde fixation on the morphology of endosomes and lysosomes: Quatitative analysis and electron tomography. *J. Microsc.* **212**, 81-90.

42. Perkins G.A., Renken C.W., Frey T.G., Ellisman M.H. 2001 Membrane architecture of mitochondria in neurons of the central nervous system. *J. Neurosci. Res.* **66**, 857-865.

43. Perktold A., Zechmann B., Daum G., Zellnig G. 2007 Organelle association visualized by three-dimensional ultrastructural imaging of the yeast cell. *Federation of European Microbiological Societies Yeast Research* **7**, 629-638.

44. Tomova C., Geerts W.J., Müller-Reichert T., Entzeroth R., Humbel B.M. 2006 New comprehension of the apicoplast of Sarcocystis by transmission electron tomography. *Biol. Cell* **98**, 535-45.

45. Zeuschner D., Geerts W.J., van Donselaar E., Slot J.W., Koster A.J., Klumperman J. 2005 Immuno-electron tomography of ER exit sites reveals the existence of free COPII-coated transport carriers. *Nat. Cell Biol.* **8**, 377-83.

46. McIntosh J.R., Grishchuk E.L., Morphew M.K., Efremov A.K., Zhudenkov K., Volkov V.A., Cheeseman I.M., Desai A., Mastronarde D.N., Ataullakhanov F.I. 2008 Fibrils Connect Microtubule Tips with Kinetochores: A Mechanism to Couple Tubulin Dynamics to Chromosome Motion. *Cell* **135**, 322–333.

47. Müller M., Marti T., Kriz S. 1980 Improved structural preservation by freeze substitution. In: Brederoo P, de Priester W (ed) Proceedings of the 7th European Congress on Electron Microscopy. pp 720-721.

48. Humbel B., Müller M. 1986 Freeze substitution and low temperature embedding. In: Müller M, Becker RP, Boyde A, Wolosewick JJ (eds) The Science of Biological Specimen Preparation 1985. SEM Inc., AMF O'Hare, pp 175-183.

49. Studer D., Michel M., Wohlwend M., Hunziker E.B., Buschmann M.D. 1995 Vitrification of articular cartilage by high-pressure freezing. *J. Microsc.* **179**, 321-332.

50. Millen J.I., Pierson J., Kvam E., Olsen L.J., Goldfarb D.S. 2008 The luminal N-terminus of yeast Nvj1 is an inner nuclear membrane anchor. *Traffic* **9**, 1653-64.

51. Al-Amoudi A., Studer D., Dubochet J. 2005 Cutting artifacts and cutting process in vitreous sections for cryo-electron microscopy. *J. Struct. Biol.* **150**, 109-121.

52. Salje J., Zuber B., Löwe J. 2009 Electron cryomicroscopy of *E. coli* reveals filament bundles involved in plasmid DNA segregation. *Science* **323**, 509-12.

53. Bouchet-Marquis C., Zuber B., Glynn A.M., Eltsov M., Gradenbauer M., Goldie K.N., Thomas D., Frangakis A.S., Dubochet J., Chretien D. 2007 Visualization of cell microtubules in their native state. *Biol. Cell* **99**, 45-53.

54. Al-Amoudi A., Castano-Diez D., Betts M.J., Frangakis A.S. 2007 The molecular architecture of cadherins in native epidermal desmosomes. *Nature* **450**, 832-837.

55. Zhang P., Bos E., Heymann J., Gnaegi H., Kessel M., Peters P.J., Subramaniam S. 2004 Direct visualization of receptor arrays in frozen-hydrated sections and plunge-frozen specimens of E.coli engineered to overproduce the chemotaxis receptor Tsr. *J. Microsc.* **216**, 76-83.

56. Sartori Blanc N., Studer D., Ruhl K., Dubochet J. 1998 Electron beam-induced changes in vitreous sections of biological samples. *J. Microsc.* **192**, 194-201.

57. Sartori N., Bednar J., Dubochet J. 1996 Electron-beam-induced amorphization of ice III or IX obtained by high-pressure freezing. *J. Microc.* **182**, 163-168.

58. Dubochet J., Zuber B., Eltsov M., Bouchet-Marquis C., Al-Amoudi A., Livolant F. 2007 How to "Read" a Vitreous Section. In: McIntosh JR (ed) Cellular electron microscopy, Academic Press, pp 385-406.

59. Sartori A., Gatz R., Beck F., Rigort A., Baumeister W., Plitzko J.M. 2007 Correlative microscopy: bridging the gap between fluorescence light microscopy and cryo-electron tomography. *J. Struct. Biol.* **160**, 135-145.

60. Schwartz C.L., Sarbash V.I., Ataullakhanov F.I., McIntosh J.R., Nicastro D. 2007 Cryo-fluorescence microscopy facilitates correlations between light and cryo-electron microscopy and reduces the rate of photobleaching. *J. Microsc.* **227**, 98-109.

61. Plitzko J.M., Rigort A., Leis A. 2009 Correlative cryo-light microscopy and cryo-electron tomography: from cellular territories to molecular landscapes. *Curr. Opin. Biotechnol.* **20**, 83-89.

62. Marko M., Hsieh C., Schalek R., Frank J., Mannella C. 2007 Focused-ion-beam thinning of frozen-hydrated biological specimens for cryo-electron microscopy. *Nat. Methods* **4**, 215-217.

63. Singh G., Rice P., Mahajan R.L., McIntosh J.R. 2009 Fabrication and characterization of a carbon nanotube-based nanoknife. *Nanotechnology* **20**, 095701.

64. Eltsov M., Maclellan K.M., Maeshima K., Frangakis A.S., Dubochet J. 2008 Analysis of cryo-electron microscopy images does not support the existence of 30-nm chromatin fibers in mitotic chromosomes in situ. *Proc. Natl. Acad. Sci. USA* **105**, 19732-19737.

65. Jin L., Milazzo A.C., Kleinfelder S., Li S., Leblanc P., Duttweiler F., Bouwer J.C., Peltier S.T., Ellisman M.H., Xuong N.H. 2007 Applications of direct detection device in transmission electron microscopy. *J. Struct. Biol.* **161**, 352-8.

66. McIntosh J.R. 2007 Cellular electron microscopy. Academic Press.

Chapter 3

Improving the Technique of Vitreous Cryo-Sectioning for Cryo-Electron Tomography: Electrostatic Charging for Section Attachment and an Anti-Contamination Glove Box

Jason Pierson[a], Jose, Jesus Fernandez[b,c], Erik Bos[a], Shoaib Amini[a], Helmut Gnaegi[d], Matthijn Vos[a], Bennie Bel[e], Freek Adolfsen[e], Jose L. Carrascosa[b], Peter J. Peters[a,f]

[a] Divison of Cell Biology II, The Netherlands Cancer Institute – Antoni van Leeuwenhoek Hospital, Plesmanlaan 121, 1066 CX Amsterdam, The Netherlands

[b] Centro Nacional de Biotechnologia – CSIC, Campus Universidad Autonoma, Cantoblanco, 28049 Madrid, Spain

[c] Department of Computer Architecture, University of Almeria, Almeria 04120, Spain

[d] Diatome Ltd, PO Box 1164, CH-2501 Biel, Switzerland

[e] Simco (Nederland) B.V., PO Box 71, 7240 AB Lochem, The Netherlands

[f] Kavli Institute of Nanoscience, Delft University of Technology, Delft, The Netherlands

Abstract

Cryo-electron tomography of vitreous cryo-sections is the most suitable method for exploring the 3D organization of biological samples that are too large to be imaged in an intact state. Producing good quality vitreous cryo-sections, however, is challenging. Here, we focused on the major obstacles to success: contamination inside and around the microtome, and attachment of the ribbon of sections to an electron microscopic grid support film. The conventional method for attaching sections to the grid has involved mechanical force generated by a crude stamping or pressing device, but this disrupts the integrity of vitreous cryo-sections. Furthermore, attachment is poor, and parts of the ribbon of sections are often far from the support film. This results in specimen instability during image acquisition and subsequent difficulty with aligning projection images.

Here, we have implemented a protective glove box surrounding the cryo-ultramicrotome that reduces the humidity around and within the microtome during sectioning. We also introduce a novel way to attach vitreous cryo-sections to an EM grid support film using electrostatic charging. The ribbon of vitreous cryo-sections remains in place during transfer and storage and is devoid of stamping related artifacts. We illustrate these improvements by exploring the structure of putative cellular 80S ribosomes within 50nm, vitreous cryo-sections of *Saccharomyces cerevisiae*.

3.1 Introduction

An important goal of structural biology is to visualize protein complexes within the cell using methods that involve a minimum of preparation associated artifacts. In recent years, cryo transmission electron tomography (cryo-ET) has taken the forefront for imaging large and stochastically variable structures with close-to-native preservation; it is currently the best technique available for imaging cellular machinery *in situ* at molecular resolution[1]. The technique has been limited, however, to specimens that are less than ~500 nm thick. When cells of a greater thickness are imaged, the low contrast and signal-to-noise ratio (SNR) create problems with image interpretation and identification of macromolecules within the context of a cell. As a result, most of the literature on cryo-ET is related to isolated macromolecular complexes or organelles[2], relatively small cells[3], or on the thin margins of extended cells[4]. If cryo-ET is to become the general tool of choice for biological imaging, then a suitable method to slice large cells and tissue must be established.

Vitreous cryo-sectioning with a diamond knife has shown considerable promise for slicing large cells and tissue[5]. Its application to tomography, however, has been limited[6,7,8,9,10] due to a number of technical obstacles[7,11]. One such limitation is contamination, in the form of large crystals, which accumulate inside the microtome, on the support film of an electron microscopic (EM) grid, and the vitreous cryo-sections.

Attachment of the vitreous cryo-sections to an EM grid support film is another technical bottleneck that limits the areas of the section that are suitable for cryo-ET.

Currently, the methods used for creating attachment involve mechanical forces, generated by either a stamping tool or a pressing device[12,13]. Using these methods for attachment, damage in the form of large fissures or cracks can be observed[7], which alters the integrity of both the ribbon of vitreous cryo-sections and the individual sections.

In addition, mechanical pressing creates only a limited number of contacts between the support film and the vitreous cryo-sections, resulting in poor adhesion between the section and the support film. This hinders tomographic data collection, due to erratic movements of the sample during imaging[14], especially at high tilt angles, which subsequently compromises the use of fiducials for tilt-series alignment. Finally, there is a high chance that the vitreous cryo-sections become completely detached from the grid during the transfer to the EM.

In the present study we have implemented an anti-contamination glove box to create a reduced humidity environment surrounding the cryo-ultramicrotome. We also introduce a novel attachment method using electrostatic charging in a dry cryo-ultramicrotomy chamber. Similar ideas have been introduced in the past[15,16] to circumvent section disruption, however, the application of such procedures has been minimal. Using our novel electrostatic charging technique we have: 1) increased the reliability and relative throughput of suitable vitreous sections for electron tomography and 2) retained proper cryo-section ribbon integrity. We illustrate our novel techniques by analyzing putative cellular 80S ribosome's from *S. cerevisiae*.

3.2 Materials and methods

3.2.1 Specimen Preparation

S. cerevisiae were harvested at mid to late log phase (OD600 of ~1.5) in YEP medium (30 g/L Dextrose) and 5 g/L yeast extract supplemented with 20% Dextran (w/v) (from *Leuconostoc mesenteroides*, 35-45 kDa; Sigma Chemical, St. Louis), a medium in which we have established an unperturbed cellular growth rate. In addition, *S.cerevisiae* in its original culturing media as mentioned above (without the addition of Dextran prior to freezing) was taken as a control. Yeast suspensions were taken up into copper tubes (inner Ø 350 µm) as described[17], and vitrified using an EM-PACT2 high-pressure freezing machine (Leica Microsystems, Vienna). The pressure reached 2000 bar within 15 ms and had a nominal cooling rate of ~20,000°C s^{-1}. After freezing, the copper tubes were stored in liquid nitrogen.

3.2.2 Cryo-Ultramicrotomy

A single copper tube was transferred to a pre-cooled (-150ºC) EM FC6 cryo-ultramicrotome (Leica Microsystems, Vienna) that was covered with an anti-contamination glove box or 'Cryosphere' (Leica Microsystems, Vienna) (Supplementary Fig. SF3.1). In addition, dry sodium hydroxide pellets and an influx of dry nitrogen gas were used to reduce the humidity further and create over-pressure within the chamber; the humidity within the chamber could be reduced to below 1% RH.

The copper tube containing the vitrified sample was trimmed to a square block-face with dimensions approximately 100 µm x 100 µm using a cryotrim-45 diamond blade (Diatome, Biel, Switzerland). Fiducial gold markers were attached to C-Flat™ EM grids CF-2/2-2C[18] (Aurion, Wageningen, The Netherlands) by successively floating them on 10 µL drops of 10 nm gold (diluted 1:60 in distilled water) (Aurion), PBS, and distilled water. The excess liquid was removed from the grid using filter paper and the grids were stored. We found that C-Flat support films were preferable as the support film remained flatter then the support film of carbon coated molybdenum or copper grids when submerged in liquid nitrogen (Supplementary Fig. SF3.2).

Ribbons of vitreous cryo-sections were produced at a nominal cutting feed of 30 to 50 nm at cutting speeds ranging from 1 to 100 mm/sec; the first sections of the block-face were cut at a speed of 0.6 to 1 mm/sec. If the surface gliding properties were suitable (i.e. vitreous cryo- sections were not sticking to the knife, appeared 'shiny', and flat), then the speed was increased incrementally to 20 mm/sec, 50 mm/sec and ultimately 100 mm/sec), using a 35º cryo diamond knife (Diatome, Biel, Switzerland) with a clearance angle of 6˚. The cutting speed was varied only to ease the collection of long vitreous section ribbons (~3 mm or longer). Ribbons of vitreous cryo-sections were attached to the pre-treated EM grids using two independent methods for comparison. In both methods the electrode was positioned ~10-20 mm from the knife.

3.2.2.1 Conventional attachment using stamping

A ribbon of vitreous cryo-sections (microtome feed setting 50 nm) was pulled from the knife edge using an eyelash attached to a wooden dowel, placed on top of the EM grid,

re-positioned on a smooth platform behind the knife and stamped using a polished metal stamping tool (Leica, Vienna, Austria). The grid was transferred to a grid box (Gatan) and stored in liquid nitrogen.

3.2.2.2 Electrostatic charging for attachment

 A ribbon of vitreous cryo-sections was pulled from the knife-edge (as above) over the EM grid and attached using electrostatic charging. Charging was accomplished via a generator connected to an electrode positioned above the knife (approximately 10-20 mm from the diamond knife). During normal ionization the electrode emitted a high voltage negative direct current (DC), which created a strong negative field towards the ribbon of vitreous sections. Switching between ionization and electrostatic charging was controlled using foot pedals or a control box. During electrostatic charging, the electrical field (emitted from the electrode) was switched to a negative polarized, low voltage (kV range) field. The ribbons of vitreous cryo-sections acted as an isolator (non-conductive) and the negatively charged ions remained on the ribbon, therefore electrostatically attaching the ribbon to the support film of a grounded, conductive EM grid positioned beneath, and perpendicular, to the field of charging (Fig. 3.1). The entire electrostatic charging apparatus (named 'CRION') has been incorporated into the new generation Leica FC7 EM cryo-ultramicrotome (Leica Microsystems, Vienna), with equipment developed by Simco, Lochem, The Netherlands. After charging, the grid was transferred to a grid box (Gatan Inc., Pleasanton, CA) for storage in liquid nitrogen.
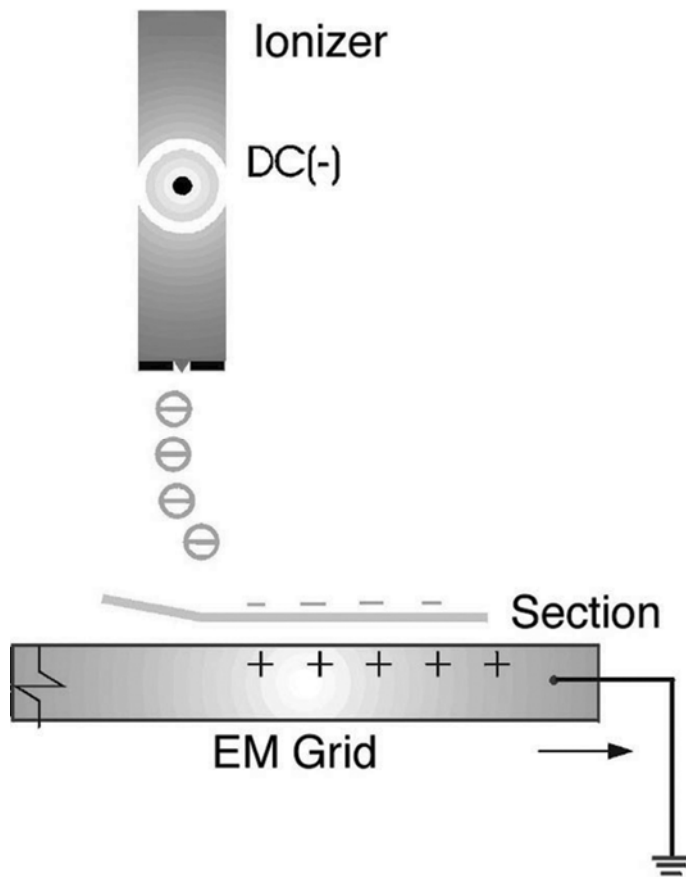
Figure 3.1: A schematic drawing that shows the principle of electrostatic charging. At the top of the scheme is the electrode (Ionizer). The electrode is connected to negative DC high voltage, which will create a strong negative (Ө) field. The rectangle at the bottom of the figure represents an EM grid, which is connected to ground through tweezers. Due to the fact that the ribbon, shown between the EM grid and the electrode, acts like an isolator (non conductive) the negatively charged ions (-) remain on the ribbon of sections. The grounded EM grid is conductive and therefore an electrostatic force (attraction) between the negatively charged ribbon and the EM grid exists.

3.2.3 Electron Cryo-Microscopy / Tomography

3.2.3.1 Single projection Images

Vitreous cryo-sections were imaged using a Tecnai 12 TEM (FEI, Eindhoven, The Netherlands). Images were recorded at 120 kV at liquid nitrogen temperatures on a 4k x 4k FEI Eagle CCD camera (FEI, Eindhoven, The Netherlands).

A nominal magnification of 1900x, with a 5.3 nm pixel size, was used for low magnification comparison between different attachment methods (electrostatic charging and stamping).

3.2.3.2 High-Resolution Tomography

Ribbons of vitreous cryo-sections supported by EM grids were mounted in autoloader clips and inserted into the Titan autoloader (FEI, Eindhoven, The Netherlands). Images were recorded at 300 kV, using a Titan cryo-TEM (Technical University of Eindhoven – TU/e, Eindhoven, The Netherlands) operated at liquid nitrogen temperatures equipped with a Gatan post column energy filter and a 2k x 2k Gatan CCD camera (Gatan Inc., Pleasanton, CA.). Single axis tilt series were collected using FEI Xplore3D (FEI, Eindhoven, The Netherlands) acquisition program under low dose conditions. The angular tilt range was typically set from -65º to +65º with a 1.5 – 2º tilt increment, and an objective lens defocus of -4.5 to -5.5 μm. Total dose was kept at or below ~100e/Å^2 with a pixel size of 0.6 nm. Projection images were aligned using 10 nm gold fiducial markers on the EM support film and reconstructed (R-weighted back

projection) using the IMOD package[19]. General visualization and surface rendering was performed using Amira (http://amira.zib.de).

3.2.4 Subtomogram averaging

 The structure of the 80S Ribosome from *S. cerevisiae*[20] was taken from the EM Data Bank at the EBI (http://www.ebi.ac.uk/pdbe/emdb/) (entry emd-1076) and used as a template. A template-matching procedure was then applied to detect putative ribosomes within a binned version of the tomogram using Spider commands[21]. False positives were discarded by visual inspection. Ribosome locations of 354 positive peaks were then extracted from the tomogram at full resolution. Angular determination and refinement were carried out as described[22,23], using Bsoft tools[24]. The resolution of the average ribosome was assessed based on the Fourier shell correlation (FSC) of two independent averages, each from half of the collected ribosomes[22].

3.3 Results

3.3.1 Reduced Contamination Vitreous Cryo-Sectioning

Contamination hampers all low temperature cryo-EM/ET techniques. In the case of low-temperature vitreous cryo-sectioning, the source is the air-nitrogen interface at the top of the microtome chamber (Supplementary Fig. SF3.3). In normal room humidity this interface can be compared to a 'cloud' that results in a blanket of contamination that covers the cryo-'tools' used inside the microtome, including the diamond knife (Fig. 3.2A).

To reduce contamination, a glove box was placed around the microtome (Supplementary Fig. SF3.1). In addition, we placed sodium hydroxide pellets inside the chamber and used a steady flow of dry nitrogen to further reduce the humidity. The dry nitrogen flow creates an overpressure within the chamber that maintains the low humidity when the glove box is opened to the outside environment. In this situation, the humidity can be reduced to below 1%. In this atmosphere, the air-nitrogen interface is not visible and the cryo-'tools', including the diamond knife, remain clean during vitreous cryo-sectioning (Fig. 3.2B).
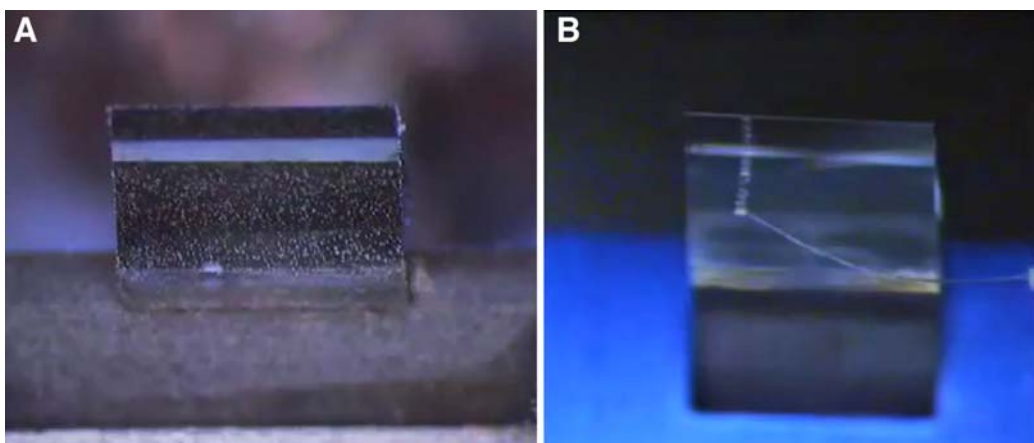
Figure 3.2: Reducing contamination within the ultramicrotome at cryo-temperatures. (A) A diamond knife within an ultramicrotome at ambient humidity, which is heavily contaminated. (B) A diamond knife that is within an ultramicrotome that is surrounded by an anti-contamination glove box. The knife remains clean during vitreous cryo-sectioning.

3.3.2 Electrostatic charging

To facilitate cryo-ET of vitreous cryo-sections, the ribbon of sections must be well attached to the support film of an EM grid. Conventional stamping/pressing techniques compromise the integrity of the ribbon of vitreous cryo-sections. The force generated for attachment is not sufficient to retain the ribbon during storage in liquid nitrogen, and the vitreous cryo-sections are usually at a distance, from a few nanometers to micrometers, from the support film of the EM grid[7].

To circumvent these technical obstacles, a novel electrostatic charging procedure was developed to attach the sections to an EM grid support film. The complete apparatus consists of a generator, which applies a high voltage to an electrode, foot pedals to control the output of the generator, and a control box. The discharge mode produces an ionization current, which enhances the surface gliding properties of the diamond knife

during vitreous cryo-sectioning. The amplitude of ionization can be regulated either with a potentiometer or through external control. A charging mode is used for attaching the vitreous cryo-sections to an EM grid support film. When the generator is switched from discharge to charge, a burst of negative charge, approximately 1 sec in duration, is produced in the vicinity of the electrode (Fig. 3.1). This process firmly attaches the vitreous cryo-sections to the support film. The detailed procedure is as follows: an EM grid is placed in the vicinity of the diamond knife (Fig. 3.3A). A relatively long ribbon of sections (denoted in Fig. 3.3B and C with white arrowheads) is pulled using an eyelash from the knife-edge over the EM grid (Fig. 3.3B). It is then attached using electrostatic charge (Fig. 3.3C). For proper attachment, the ribbon of sections must be above the EM grid, and the electrode tip must be normal to the plane of both the ribbon of vitreous sections and the EM grid, and about a distance of 10-20 mm from the grid.

3.3.3 Attachment using electrostatic charging compared to conventional stamping

In our experience, stamping vitreous cryo-sections to an EM support film resulted in a number of mechanically induced artifacts in both the ribbon of sections and in the support film of the EM grid, reducing the number of suitable areas for tomography. The types of damage that were characteristically introduced by mechanical stamping/pressing based attachment methods were prevented by using the electrostatic charging method (Fig. 3.3D and E). In addition, the charging procedure did not alter the vitreous state of the ice, as assessed by electron diffraction (Fig. 3.3F).
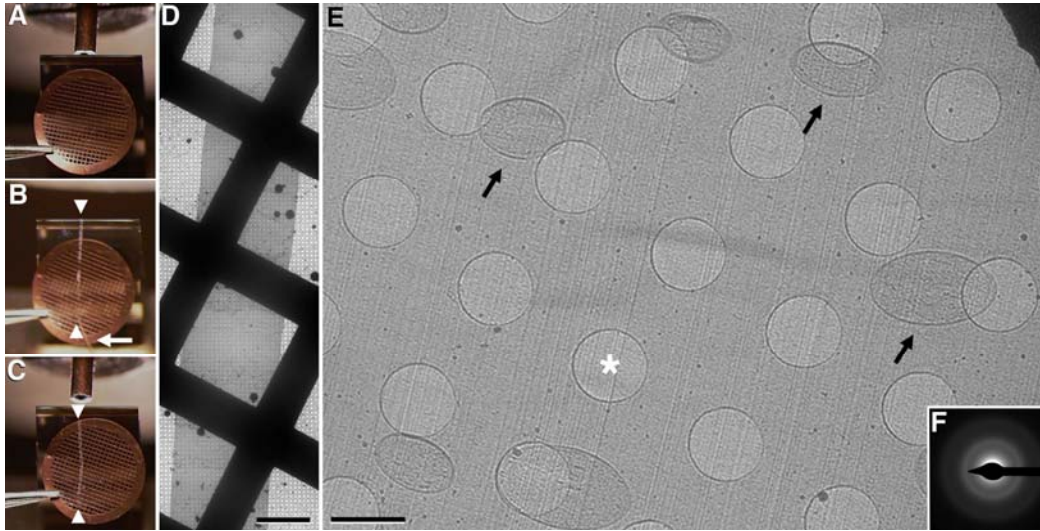
Figure 3.3: Electrostatic charging technique for attaching a ribbon of vitreous sections to an EM support film. (A) An EM grid is placed at the diamond knife-edge using tweezers with a bent tip. (B) A ribbon of vitreous sections (white arrowheads) is guided over the EM grid using an eyelash (white arrow) attached to a wooden dowel. (C) Once the ribbon of vitreous sections is of suitable length (white arrowheads), approximately the diameter of the EM grid; the generator is switched from the discharge mode to the charge mode, causing the ribbon to attach to the EM grid. (D) A low magnification image showing the ribbon of vitreous sections after electrostatic charging. Scale bar = 50 μm. (E) A medium magnification micrograph showing a vitreous section from within the ribbon. Note that the section is smooth and relatively flat with no apparent mechanically induced damage as is often seen with stamping/pressing techniques. *S. cerevisiae* cells can be seen scattered throughout the vitreous section (black arrows). Holes within the C-Flat EM grid can be seen and one such is denoted with a white asterisk. Scale bar = 2 μm. (F) A selected area diffraction pattern confirming vitreous ice.

We have repeatedly seen that stamping was not sufficient to achieve good attachment of the ribbon of vitreous cryo-sections to the support film of an EM grid. After stamping, an eyelash was used to probe the interaction between the ribbon and the substrate. The ribbon was easily removed, suggesting that the method was not

56

adequate for proper attachment. With electrostatic charging, the ribbon remained attached to the support film.

In order to quantify the success rate between the two attachment methods, comparison grids were produced under similar conditions (diamond knife, sample, ribbon length) using the stamping method and the electrostatic charging method. In every case where electrostatic charging was used for attachment, the ribbon was retained when observed in the EM. This was not the case, however, for the conventional stamping method. In a study of 5 grids that were prepared using the conventional stamping method, 2 out of the 5 were completely empty, even though the ribbon was observed in the microtome prior to transfer to the EM. This suggests that electrostatic charging increases the likelihood and reliability that a ribbon of vitreous cryo-sections will be present through transfer (in liquid nitrogen) and after insertion into the EM. 'Coarse' attachment and overall ribbon integrity was assessed using relatively low-magnification, tilted images, which can be seen in Supplemental Figure SF3.4.

3.3.4 Tomography of *S.cerevisiae* vitreous sections

Tomography was performed on *S.cerevisiae* that were vitreous cryo-sectioned and collected using the novel electrostatic attachment method described above. Numerous tilt series were recorded and a representative tomogram can be seen in Fig. 3.4. The 'fine' attachment was verified by flipping the volume around the X-axis (Fig. 3.4B), which directly shows that the vitreous section (black arrowheads) is well attached to the support film (white arrowheads). Alignment of individual projection images was accomplished using 10 nm gold fiducial markers applied to the surface of the carbon

support film, our method of choice for tracking individual projection images within a tilt series for volumetric reconstruction. In the displayed tomogram, the residual mean error and standard deviation was below 1 pixel.

Specific cellular structures could be identified in a representative 5 nm slice from a tomographic reconstructed volume (Fig. 3.4A); a mitochondrion (M), profiles of the endoplasmic reticulum (ER), and a vacuole (V) are all evident. Large macromolecular complexes, such as putative 80S ribosomes, could also be recognized within the cell due to their inherent high contrast (black arrows).
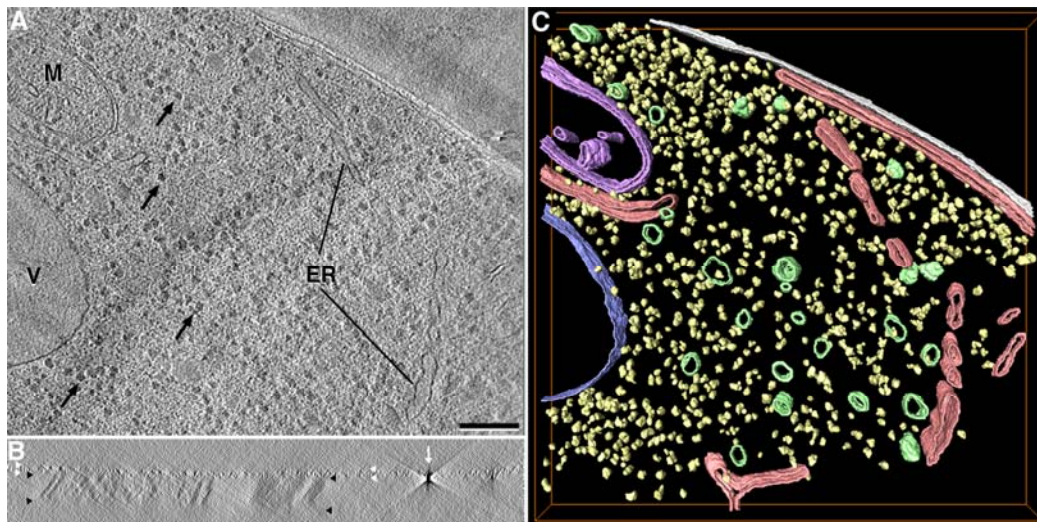

Figure 3.4: Tomography of Vitreous Sections of *S.cerevisiae*. (A) 5-nm-thick tomographic slice from a vitreous section, (V) Vacuole, (M) Mitochondrion, (ER) Endoplasmic Reticulum, and black arrows indicate putative 80S ribosomes. Scale bar = 100 nm. (B) A flipped view (about the x-axis) from the tomographic reconstruction in (A). The vitreous section (black arrowheads) is well attached to the support film (white arrowheads). A fiducial gold marker is seen on the surface of the carbon support film (white arrow). Scale bar = 100 nm. (C) A surface rendered visualization of the tomographic volume in (A). Mitochondrion, purple; Vacuole, blue; Endoplasmic Reticulum, red; cell membrane, white; unidentified vesicle structures, green; unidentified macromolecular complexes including putative ribosomes, yellow.

We then focused on these *in situ* ribosome-like particles to illustrate the potential of the novel techniques proposed, deriving an average eukaryotic 80S ribosome map. The average ribosome map (Fig. 3.5) was computed by the standard combination of template matching and angular refinement[22], and had a resolution of 5.6nm (FSC 0.5 criterion, see supplemental Fig. SF3.5). The denoted (Fig. 3.5A and B) structural features that are recognizable from the 40S small subunit (40S) include the beak (bk) and the body (b). From the 60S large subunit (60S), the stalk base (SB) and the L1 protuberance (L1) are denoted[20].
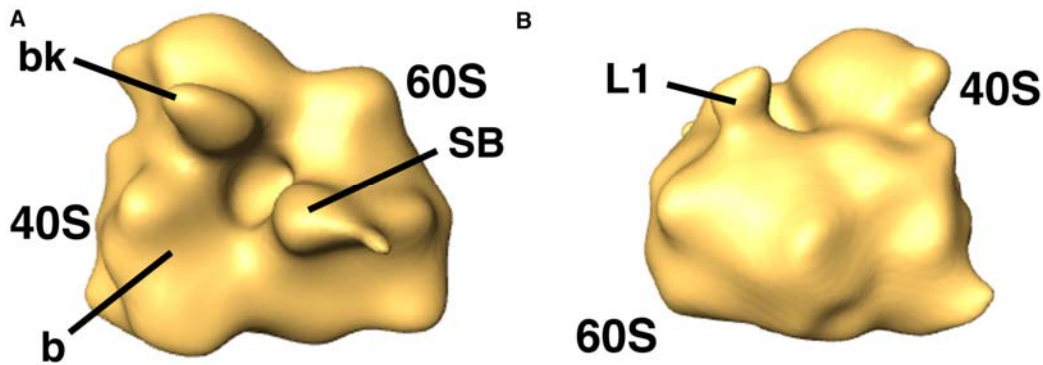

Figure 3.5: 80S *S.cerevisiae* ribosome density map. (A) Specific 80S Ribosomal features can be recognized; the large 60S subunit (60S) and the associated stalk base complex L7/L12 region (SB), the small sub-unit (40S), beak region (bk) and base (b) region of the 40S. (B) A 90° rotated view from (A) that shows the L1 region of the 60S large sub-unit.

3.4 Discussion

Cryo- ET of large cells and tissue can only be carried out after slicing these cells into thin sections. Tomography of vitreous sections, however, has been limited due to a number of technical bottlenecks[7]. Here we have addressed the major difficulties; contamination in and around the microtome and attachment of the vitreous sections to an EM support film.

Frost contamination has been significantly reduced, by using a glove box surrounding the microtome to produce a controlled, low humidity, environment. An unanticipated benefit of the environmental chamber was that ionizing properties of the electrode were observed to be more effective in a low humidity environment. In a normal room environment, the ionization electrode can become covered with ice contamination, which may reduce the electrical field strength from the electrode. When ionization is compromised, the surface-gliding properties of the diamond knife can be affected, which can make producing high quality vitreous cryo sections difficult.

Attachment of vitreous cryo-sections to the support film of an EM grid has been problematic using conventional, force generating attachment methods, such as stamping or pressing. Although different techniques for mechanical attachment have been explored, none has yet been able to solve the attachment problem. Using electrostatic charging, the ribbon of vitreous sections is well attached to the EM grid support film, which increases the likelihood for successful tomography. Using conventional attachment methods, sections often moved or drifted during imaging due to the gap between the vitreous cryo-sections and the support film. With electrostatic

charging, the sections are flush against the support film and therefore stable during imaging.

In addition, because the attachment has been improved using electrostatic charging, colloidal gold particles on the support film can be used as fiducial markers for tilt series alignment. This is generally not the case with stamping. The poor attachment causes problems with aligning individual projection images from a tilt series to a common register because the section being imaged changes its position relative to the fiducial markers on the support film during tilting.

An alternative to using colloidal gold as fiducial markers is alignment through cross correlation-based algorithms[25,26] that rely on tracking distinguishable features throughout the individual projection images. Cross correlation methods work relatively well when there is a high contrast and signal-to-noise within the images to facilitate feature tracking. Unfortunately, the inherent low contrast and signal-to-noise in cryo imaging techniques makes the tracking of distinguishable features rather difficult. In addition to cross correlation methods, there are procedures for applying fiducial markers directly onto the surface of the vitreous sections. Such methods include the use of Quantum Dots[27] and also colloidal gold particles as fiducial markers[28]. Unfortunately, vitreous sections are capricious during tilt series acquisition[14], which can compromise the alignment as mentioned above. The most optimal situation may be to have tracking markers (quantum dots or colloidal gold) applied both to the surface of the vitreous sections, and to the support film.

In this study, the operator manually controlled the positioning of both the ribbon of vitreous cryo- sections and the EM grid prior to attachment. A more suitable method may employ a micromanipulator[29], which would reduce the error of positioning. Using micromanipulation, a gentle tension can be maintained as the ribbon of vitreous cryo-sections is pulled from the knife-edge. Combining micromanipulation with electrostatic charging may be the most optimal technique.

Electron tomography allows the identification of macromolecular complexes, together with analysis of their spatial distribution and interactions in the native cellular context[23]. The electrostatic charging technique for attaching for vitreous sections to the EM grid for cryo-ET facilitates studies on thin slices of biological specimens. As an illustrative example of the potential of this technique, the average eukaryotic ribosome *in situ* has been computed from a section of *S. cerevisiae*. This is the first step towards the construction of an 80S ribosomal map from a thin slice of a large eukaryotic cell, and towards identification of specific macromolecular spatial arrangements within the cellular context, as already revealed for prokaryotic cells[22,23]. However, compression at the macromolecular level remains ambiguous and must be addressed in future studies. For future studies we must be fully confident that we only detect and select true cellular 80S ribosomes.

Although the resolution of the final ribosomal density map obtained here was sufficient to detect large structural landmarks on the 80S ribosome, increasing the particle pool may improve the resolution limits, as is commonly seen in single particle cryo-EM. We expect that these densities will be better defined in the near future, as the resolution within our density maps improve, and in combination with the rapidly

expanding structural database for the 80S eukaryotic ribosome and its protein complexes.

3.5 Conclusions

The technique of vitreous cryo-sectioning still remains a challenge; however the novel techniques presented here facilitate the procedure. We have shown that frost contamination is reduced inside the cryo ultramicrotome, when a protective anti-contamination glove box is used. We have also shown that electrostatic charging enhances attachment to an EM support film without compromising the integrity of ribbons of vitreous cryo-sections, so that the throughput of suitable areas for tomography can be increased compared to conventional methods. We obtained an initial glimpse of the putative 80S ribosomal cellular structure, within a thin vitreous cryo-section, when these novel improvements were applied to yeast cells.

References

1. Lucic V., Förster F., and Baumeister W. 2005 Structural studies by electron tomography: from cells to molecules. *Annu. Rev. Biochem.* **74**, 833-865.

2. Nicastro D., Schwartz C., Pierson J., Gaudette R., Porter M.E., and McIntosh, J.R. 2006 The molecular architecture of axonemes revealed by cryoelectron tomography. *Science* **313**, 944-948.

3. Henderson G.R., Gan L., and Jensen, G.J. 2007 3-D Ultrastructure of *O. tauri*: Electron Cryotomography of an Entire Eukaryotic Cell. *PLoS ONE* **8**, e749 (13pp).

4. Medalia O., Weber I., Frangakis A.S., Nicastro D., Gerisch G., and Baumeister, W. 2002 Macromolecular architecture in eukaryotic cells visualized by cryoelectron tomography. *Science* **289**, 1209-1213.

5. Dubochet J., Adrian M., Chang J.J., Homo J.C., Lepault J., McDowall A.W., and Schultz, P. 1988 Cryo-electron microscopy of vitrified specimens. *Q. Rev. Biophys.* **21**, 129-228.

6. Hsieh C.E., Marko M., Frank J., and Mannella C.A. 2002 Electron tomographic analysis of frozen-hydrated tissue sections. *J. Struct. Biol.* **138**, 63-73.

7. Hsieh C.E., Leith A., Mannella C.A., Frank J., and Marko M. 2006 Towards high-resolution three-dimensional imaging of native mammalian tissue: Electron tomography of frozen-hydrated rat liver sections. *J. Struct. Biol.* **153**, 1-13.

8. Al-Amoudi A., Díez D.C., Betts M.J., and Frangakis A.S. 2007 The molecular architecture of cadherins in native epidermal desmosomes. *Nature* **450**, 832-837.

9. Millen J.I., Pierson J., Kvam E., Olsen L.J., and Goldfarb D.S. 2008 The luminal N-terminus of yeast Nvj1 is an inner nuclear membrane anchor. *Traffic* **9**, 1653-1664.

10. Salje J., Zuber B., and Löwe J. 2009 Electron cryomicroscopy of *E. coli* reveals filament bundles involved in plasmid DNA segregation. *Science* **323**, 509-512.

11. Marko M., Hsieh C.H., and Mannella, C.E. 2006 Electron tomography of frozen hydrated sections of cells and tissues, in: Frank J. (Ed.) Electron tomography, methods for three-

dimensional visualization of structures in the cell. Springer New York, Second Edition, pp. 49-81.

12. Christensen A.K. 1971 Frozen thin sections of fresh tissue for electron microscopy with a description of pancreas and liver. *J. Cell Biol.* **51**, 772-804.

13. Frederik P.M., Busing W.M., and Persson, A. 1982 Concerning the nature of the cryosectioning process. *J. Microsc.* **125**, 167-175.

14. Sartori Blanc N., Studer D., Ruhl K., and Dubochet, J. 1998 Electron beam-induced changes in vitreous sections of biological samples. *J. Microsc.* **192**, 194-201.

15. Tsuji S., Anglade P., Daudet-Monsac M., and Motelica-Heino I. 1992 Cryoultramicrotomy: electrostatic transfer of dry ultrathin frozen sections on grids applied to the central nervous system. *Arch. Histol. Cytol.* **55**, 423-8.

16. Koller T. 1965 Mounting of ultrathin sections with the aid of an electrostatic field. *J. Cell Biol.* **27**, 441-445.

17. Studer D., Graber W., Al-Amoudi A., and Eggli P. 2001 A new approach for cryofixation by high-pressure freezing. *J. Microsc.* **203**, 285-294.

18. Quispe J., Damiano J., Mick S.E., Nackashi D.P., Fellmann D., Ajero T.G., Carragher B., and Potter C.S. 2007 An Improved Holey Carbon Film for Cryo-Electron Microscopy. *Microscopy and Analysis* **13**, 365-371.

19. Kremer J.R., Mastronarde D.N., and McIntosh, J.R. 1996 Computer visualization of three-dimensional image data using IMOD. *J. Struct. Biol.* **116**, 71-76.

20. Spahn C.M., Beckmann R., Eswar N., Penczek P.A., Sali A., Blobel G., and Frank, J. 2001 Structure of the 80S Ribosome from *Saccharomyces cerevisiae*-tRNA-Ribosome and Subunit-Subunit Interactions. *Cell* **107**, 373-386.

21. Frank J., Radermacher M., Penczek P., Zhu J., Li Y., Ladjadj M., and Leith, A. 1996 SPIDER and WEB: Processing and Visualization of Images in 3D Electron Microscopy and Related Fields. *J. Struct. Biol.* **116**, 190-199.

22. Ortiz J.O., Förster F., Kürner J., Linaroudis A.A., and Baumeister W. 2006 Mapping 70S ribosomes in intact cells by cryoelectron tomography and pattern recognition. *J. Struct. Biol.* **156**, 334-341.

23. Brandt F., Etchells S.A., Ortiz J.O., Elcock A.H., Hartl F.U., and Baumeister W. 2009 The native 3D organization of bacterial polysomes. *Cell* **136**, 261-271.

24. Heymann J.B., and Belnap D.M. 2007 Bsoft: Image processing and molecular modeling for electron microscopy. *J. Struct. Biol.* **157**, 3-18.

25. Castaño-Díez D., Al-Amoudi A., Glynn A.M., Seybert A., and Frangakis A.S. 2007 Fiducial-less alignment of cryo-sections. *J. Struct. Biol.* **159**, 413-423.

26. Winkler H., and Taylor K.A. 2006 Accurate marker-free alignment with simultaneous geometry determination and reconstruction of tilt series in electron tomography. *Ultramicroscopy* **106**, 240-254.

27. Masich S., Östberg T., Norlén L., Shupliakov O., and Daneholt B. 2006 A procedure to deposit fiducial markers on vitreous cryo-sections for cellular tomography. *J. Struct. Biol.* **156,** 461-468.

28. Gruska M., Medalia O., Baumeister W., and Leis A. 2008 Electron tomography of vitreous sections from cultured mammalian cells. *J. Struct. Biol.* **161**, 384-392.

29. Ladinsky M.S., Pierson J., and McIntosh J.R. 2006 Vitreous cryosectioning of cells, facilitated by a micromanipulator. *J. Microsc.* **224**, 129-134.

3.6 Supplementary Data

3.6.1 Specimen Preparation

Saccharomyces cerevisiae were harvested at mid-log phase (OD600 of ~1.5) in YE medium (30 g/L Dextrose) and 5 g/L yeast extract, filtered (using a filter-syringe) to create a highly concentrated soft pellet, and re-suspended in 20% Dextran (w/v) (from Leuconostoc mesenteroides, 35-45 kDa, Sigma Chemical). Note: Two controls were also taken: 1) 20% Dextran was omitted from the protocol, providing an important comparison between cryo-fixation in the presence and absence of 20% Dextran and 2) *S.cerevisiae* culture grown to log-phase in the presence of 20% Dextran that was supplemented in the original media. There was no observable difference between the two preparation methods, addition of Dextran or the omission in the media prior to freezing, and therefore we concluded that the addition of dextran does not alter the sub-cellular structure of the *S.cerevisiae* in a noticeable way.

3.6.2 C-Flat™ EM Grids

The C-Flat (Quispe et al., 2007) support film was observed to remain 'flat', or without wrinkles, when submerged in LN2. Whereas, carbon coated copper and molybdenum grids wrinkled after submerged in LN2 (see Supplementary Figure SF3.1). Another possible advantage of the C-Flat grids are the continuous holes throughout the carbon, which may improve attachment by allowing air between the sections and the carbon film a place to escape during the attachment procedure, a contrast to a continuous film where the air may get trapped between the carbon film and the vitreous sections.

Vitreous sections were cut at a nominal thickness of 30 to 50 nm at varying speed. The first sections of the block face usually were cut at a speed of 0.6 to 1 mm/sec, if the

surface gliding properties were suitable (i.e. sections were not sticking to the knife and appeared 'shiny' and flat), then the speed was increased, usually to 20 mm/sec, then 50 mm/sec and ultimately 100 mm/sec (depending on cutting conditions or sample requirements), using a 35º cryo diamond knife (Diatome) with a clearance angle of 6˚. The cutting speed was varied only to ease the collection of long vitreous section ribbons (~3 mm or longer), mechanical cutting artifacts were not assessed for the various speeds used in this study.

3.6.3 Electrostatic Charging

The electrode was mounted approximately 10 mm from the knife. The sections were attached to a pre-treated C-Flat grid (EMS) with 10 nm gold (Aurion) using the newly developed electrostatic charging machine or 'Crion' (Leica Microsystems, Vienna). A ribbon of vitreous sections (nominal thickness 50 nm) was pulled from the knife-edge over the C-flat grid (Main Text Figure 3.3b). The success of the electrostatic charging method depends primarily on the quality of the vitrified sample. Once a suitable specimen has been obtained there are some minor technical considerations that may improve attachment. The orientation of the charging field in relation to the ribbons of sections is important for proper attachment. If the ribbon of sections and the EM grid are not directly perpendicular to the field of charge then attachment may be compromised. In addition, there must be a gap between the ribbon of sections and the EM grid.

We have tested a number of nominal thickness settings between 30 nm to 200 nm and each setting shows similar results to those presented with 50 nm. The true section thickness was directly measured from the resulting tomogram after Z-flipping, and

was found to be 60 nm. The ribbon is then attached to the grid using electrostatic charge (Main Text Figure 3.3). Charging is accomplished via a control unit connected to the electrode positioned above the knife, with ionizing/charging perpendicular to the EM grid. Tweezers, mainly used for positioning the EM grid perpendicular to the field of charging, were earthed during charging and attachment. After charging, the grid was transferred to a grid box (Gatan) for storage.

### 3.6.4 Resolution assessment of the average ribosome

The resolution of the average ribosome, which was determined as described in Main Text Materials and Methods, was assessed based on the Fourier shell correlation (FSC) of two independent averages, each from half of the collected putative 80S ribosomes. The resolution was approximated at 5.6nm according to the 0.5 criterion (Supplementary Figure SF3.4).

Supplementary Figures

SF 3.1: An anti-contamination glove box surrounds the cryo-ultramicrotome. The chamber is used to reduce contamination in and around the microtome while vitreous cryo-sectioning. With a steady influx of dry nitrogen gas and dry sodium hydroxide pellets the humidity within the chamber can be reduced to below 1% RH.
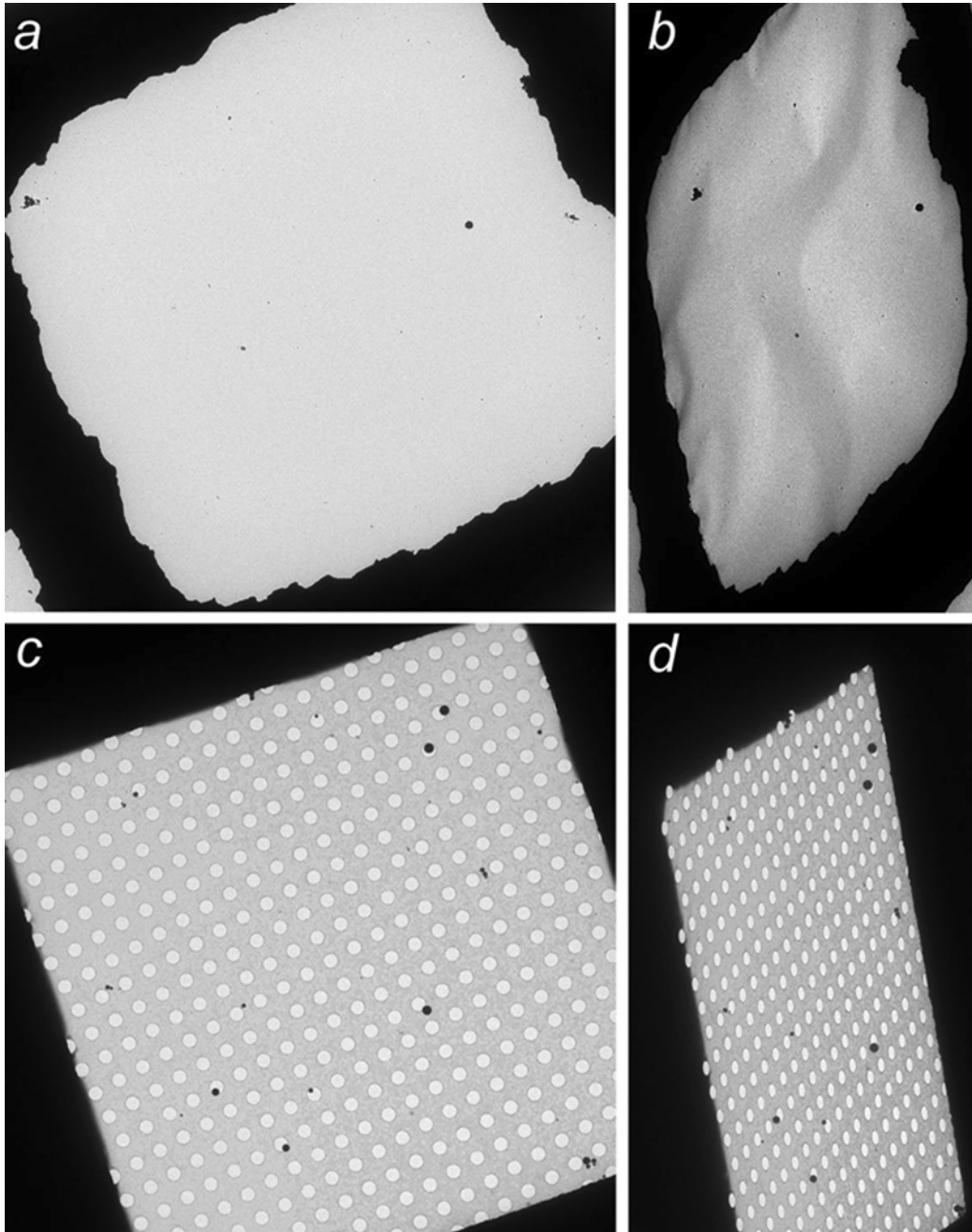
SF 3.2: C-flat EM grids compared with Molybdenum grids. A bare carbon coated molybdenum grid is shown in (A) imaged at cryogenic temperatures. (B) The same area in (A) tilted at -60º. Notice that the carbon film wrinkles as a result of cryogenic temperatures. (C) A C-flat EM grid and (D) the tilted version. The C-flat grid remains perfectly flat at cryogenic temperatures and therefore was used for our studies on vitreous sections.
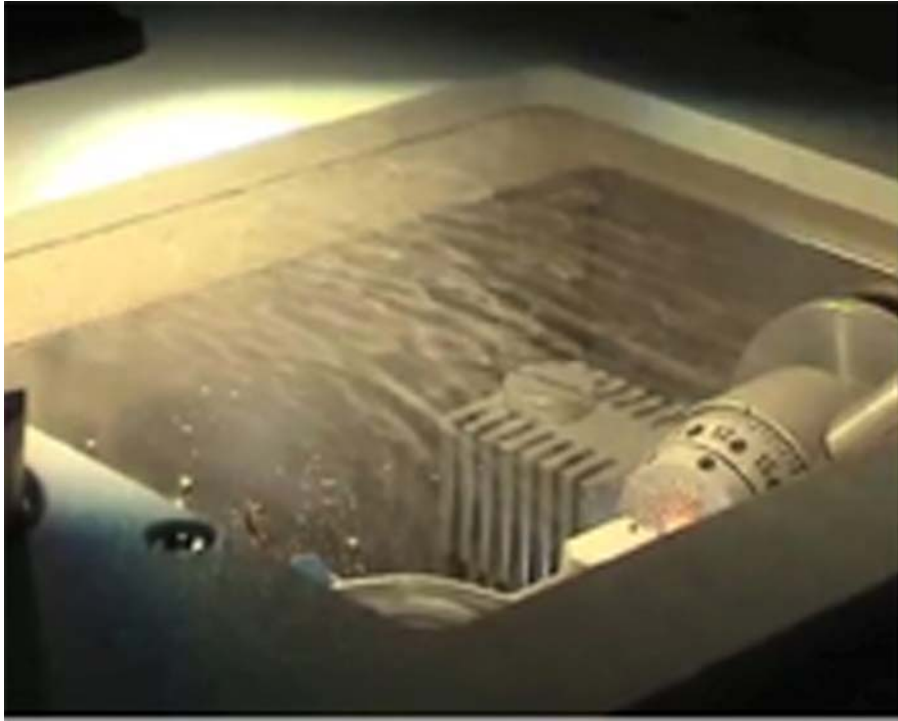
SF 3.3 The surface of a microtome chamber at ambient humidity (without an anti-contamination glove box). Notice the cloud that hovers over the chamber, which is the interface between cryo chamber nitrogen temperatures and environment. This 'cloud' produces contamination that falls on the vitreous sections and EM grids during sectioning.
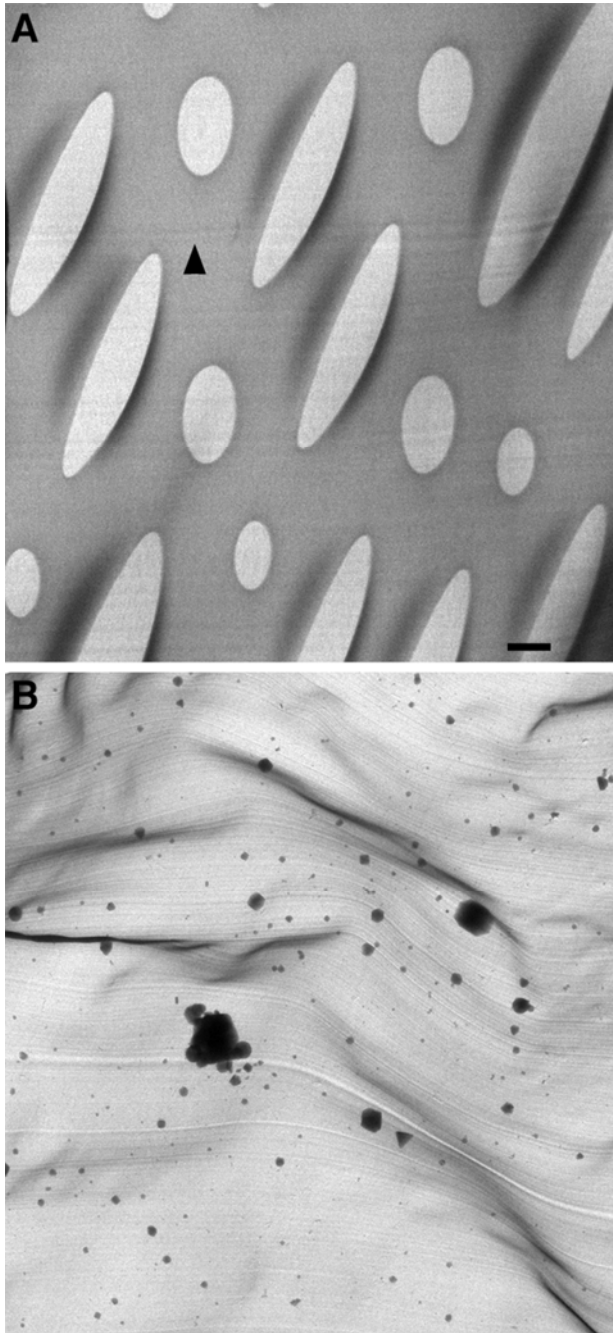
SF 3.4: Low magnification, high tilt comparison between stamping and electrostatic charging for section attachment. (A) A ribbon of vitreous cryo-sections electrostatically attached to a multi-hole C-Flat EM grid support film. Notice that the knife marks (black arrowhead) are continuous across the section, which is a direct result of a flat section. (B) A vitreous cryo-section that was stamping against a carbon coated molybdenum grid. This image shows that the sections are wavy and therefore not well attached to the support film. Scale bar = 2 um.
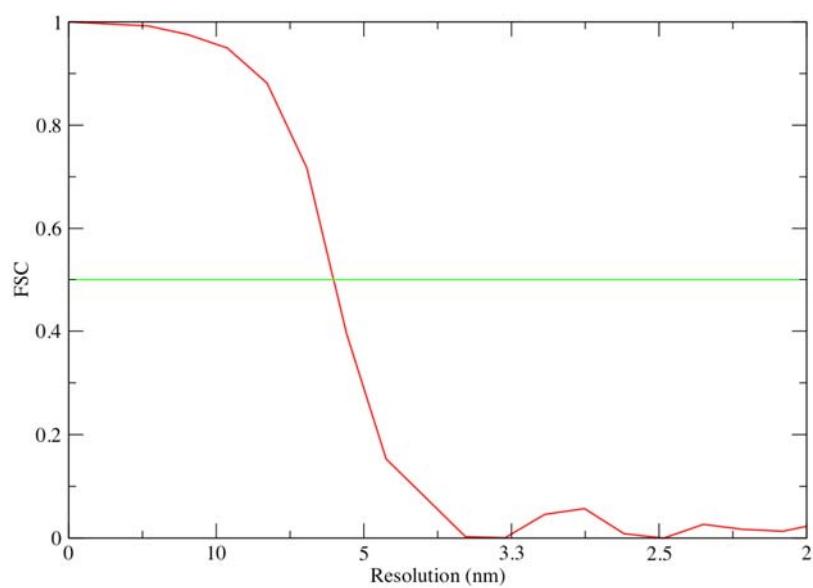
SF 3.5: Fourier Shell Correlation of the putative 80S ribosome particle average. The resolution was estimated to be 5.6nm, according to the 0.5 criterion.

Chapter 4

Exploring Vitreous Cryo-Section-Induced Compression at the

Macromolecular Level Using Electron Cryo-Tomography; 80S Yeast

Ribosomes Appear Unaffected

Jason Pierson, Ulrike Ziese, Musa Sani and Peter J. Peters[a, b*]

[a] Division of Cell Biology II, The Netherlands Cancer Institute – Antoni van Leeuwenhoek Hospital, Plesmanlaan 121, 1066 CX Amsterdam, The Netherlands

[b] Kavli Institute of Nanoscience, Delft University of Technology, Delft, The Netherlands

Abstract

Vitreous cryo-section-induced compression influences the interpretation and the reliability of electron microscopy images and tomographic reconstructions. Previous studies of this deformation have been focused at the cellular level where considerable compression occurs, yet the degree of possible intracellular macromolecular deformation has remained unclear. Here, electron cryo-tomographic reconstructions of vitreous cryo-sections show that 80S ribosomes, both intracellular and in an isolated state, appear able to resist section-induced compression. Our observations indicate that vitreous section-induced compression is non-uniform between whole cells that have been sectioned and their intracellular macromolecular complexes. We conclude that electron cryo-tomography of vitreous cryo-sections, in spite of section-induced compression, is a suitable technique for charting the structural organization of cellular nanomachines, such as ribosomes, in a cellular environment.

4.1 Introduction

Electron cryo-tomography of vitreous cryo-sections is currently the only technique that allows a three-dimensional visualization of large cells and tissue in a close-to-native state[1,2,3,4]. Both single projection images[5,6,7,8,9] and tomography[10,11,12,13,14,15] have been used to reveal structural insights into the architecture of various cells and pieces of tissue and their cellular components. Although the technique is quickly gaining importance, it is prone to several cutting-induced deformations[16,17], which include chatter, knife marks, crevassing, and compression[18,19].

Of the four cutting-induced artifacts, compression is arguably the most worrisome[20]. This is mainly because the other artifacts can be controlled, if not eliminated, by proper specimen preparation and sectioning procedures: increasing the cutting speed can reduce chatter[17]; knife marks are localized to the surface and don't seem to penetrate into the depth of the vitreous cryo-sections; the effects of crevassing are undetectable for thin sections, at or below ~50 nm nominal microtome feed[7]. Finally, each section-induced artifact is minimized with well vitrified samples.

There have been several attempts to reduce, or compensate for the fourth cutting-induced artifact: compression. Reducing the knife angles, for example from 45º to 35º [17] and in some case to 25º [7, 21] has been shown to slightly reduce the amount of measured compression but unfortunately does not eliminate it. Oscillating the diamond knife has been successful in alleviating compression for microtomy of plastic embedded specimens at room temperature[22], however, similar results have not yet been achieved for vitreous cryo-sectioning[23]. Focused ion-beam milling[24] and micromachining[20] of frozen-hydrated material is a technique that has the potential to completely overcome diamond knife-induced artifacts, however it is still in development. Finally, there has been a suggestion to alter or artificially transform the post-reconstructed volume in order to restore the original, pre-microtomed, specimen volume. If compression is approximately homogeneous[17, 8], then it can, in principle, be compensated for by a rescaling linear transformation[17].

There have been hints that vitreous cryo-sectioning-induced compression is inhomogeneous between vitreous cryo-sections of whole cells and cellular constituents. For instance in filament bundles[14], microtubules[13], desmosomes[25, 12],

77

nucleosome core particles[5], bacterial chemotaxis receptors[7], and chromatin fibers[26, 27, 28]. An in-depth study, however, to understand compression levels at the macromolecular level has been lacking.

In the present study, we have specifically explored cutting-induced compression in vitreous cryo-sections at the macromolecular level. We have analyzed cellular constituents, represented by 80S ribosomes, and no compression-induced distortion could be detected. Furthermore, we compared the morphology of isolated 80S ribosomes after plunge freezing to those that have been high-pressure frozen and vitreous cryo-sectioned. Again we found no evidence for ribosomal compression. Therefore we conclude that vitreous cryo section-induced compression does not uniformly affect sections of whole cells compared to their constituents. As a result, this technique will be invaluable for charting biological nanomachines in a native cellular environment within vitreous cryo-sections.

4.2 Methods

4.2.1 Sample Preparation

4.2.1.1 *Saccharomyces cerevisiae*

S.cerevisiae were harvested at mid to late log phase (OD600 of ~1.5) in YEP medium (30 g/L Dextrose and 5 g/L yeast extract) supplemented with 20% (w/v) Dextran (from *Leuconostoc mesenteroides*, 35-45 kDa; Sigma Chemical, St. Louis). Yeast suspensions were taken up into copper tubes (inner Ø 350 µm) as described[29], and

vitrified using an EM-PACT2 high-pressure freezing (HPF) machine (Leica Microsystems, Vienna). The pressure reached 2000 bar within 15 ms and had a nominal cooling rate of ~20,000°C s^{-1}. After freezing, the copper tubes were stored in liquid nitrogen.

4.2.1.2 Isolated 80S Ribosomes

We received purified 80S yeast ribosomes from the lab of Professor Mans Ehrenberg (Uppsala University, Sweden). The purification details can be found in Hauryliuk et al., 2006. Fiducial gold markers were applied to C-Flat™ EM grids CF-2/2-2C[31] (Aurion, Wageningen, The Netherlands) by successively floating them on 10 µL drops of 10 nm gold (diluted 1:60 in distilled water) (Aurion, Wageningen, The Netherlands), PBS and distilled water, and drying on filter paper. For plunge freezing, 3 µL of the isolated 80S ribosome preparation and 1 µL of 10 nm colloidal gold (O.D. 0.1) suspension were briefly mixed and applied to glow-discharged C-Flat EM grids, mounted in an environmentally controlled chamber at 100% humidity, blotted and vitrified by plunging into liquid ethane using the Vitrobot IV (FEI, Eindhoven, The Netherlands). Grids were stored for later analysis in liquid nitrogen. For high-pressure freezing, aliquots of isolated 80S ribosomes supplemented with 20% (w/v) Dextran were taken up into copper tubes and high-pressure frozen as in section 4.2.1.1. After freezing, the copper tubes were stored in liquid nitrogen.

4.2.2 Cryo-Ultramicrotomy

A copper tube containing the high-pressure frozen sample was transferred to a pre-cooled (-150ºC) EM FC6 cryo-ultramicrotome (Leica Microsystems, Vienna) covered with a Cryosphere™ box[15] (Leica Microsystems, Vienna), which controls the environment around the microtome. The copper tube containing the HPF sample was trimmed to a square block-face with dimensions approximately 100 μm x 100 x 50 using a cryotrim-45° diamond blade (Diatome, Biel, Switzerland). Ribbons of vitreous cryo-sections were produced at a nominal cutting feed of 50 nm at cutting speeds of 100 mm/sec; ribbons did not stick to the surface of the diamond knife and appeared shiny and flat. A single 35º cryo-immuno diamond knife (MT11699) with a clearance angle of 6˚ was used throughout the entire study in order to eliminate a potential bias of the diamond knife. Ribbons of vitreous cryo-sections were attached to C-Flat EM grids (pre-treated with fiducial markers as described in section 4.2.1.2) using electrostatic charging with the Crion™ [15] (Leica Microsystems, Vienna).

4.2.3 Electron Cryo-Tomography of Vitreous cryo-Sections

A single tilt liquid nitrogen cryo transfer holder model 626 (Gatan Inc., Pleasanton, CA, USA) was used for transferring the grid from the liquid nitrogen storage into the transmission electron microscope for imaging. Images were recorded at 120 kV, using a Tecnai 12-TEM (FEI Co., Eindhoven, The Netherlands) operated at liquid nitrogen temperatures and equipped with a 4k x 4k pixel charge-coupled device (CCD) Eagle™ camera (FEI, Eindhoven, The Netherlands). Single axis tilt series were collected semi-automatically using Xplore3D (FEI, Eindhoven, The Netherlands) acquisition program

under low dose conditions. The tilt range was typically set from -65° to +65° with a 1.5 – 2° tilt increment. Total dose was kept at or below ~70 e/Å^2. Most of the images and tilt series were recorded at an objective lens defocus of ca. -5.5 µm. Individual projection images were aligned using fiducial markers attached to the EM grid support film and subsequently reconstructed (R-weighted back projection) using the IMOD package[32].

4.2.4 Image Processing

4.2.4.1 Volumetric Transformations

Compression was measured according to the following equation: $C = (d_o - d_c) / d_o$ x 100%, where C = compression, d_o = measurements of the cellular dimensions perpendicular to the cutting direction, d_c = measurements of the cellular dimensions parallel to the cutting direction. We also measured compression levels directly from the reconstructed tomographic volumes: $C = (T_o - T_c) / T_o$ x 100%, where C = compression, T_o = section thickness measured directly from the reconstructed volume, T_c = nominal thickness set on the microtome during vitreous cryo-sectioning.

The reconstructed volumes (N=6) were rotated in IMOD to orientate the knife marks parallel to the Y-axis. A simplified volume-conserving transformation[17] (stretch in the Y direction along the cutting direction and a reduction in Z) was applied to the original reconstructions by the measured compression factor.

4.2.4.2 Volumetric Summing

The 3D coordinates of particles with the characteristics of 80S ribosomes were manually selected in the tomograms using IMOD. Manual particle selection was biased towards the middle portion of the reconstructed volume to eliminate the possibility for selecting partial 80S ribosomes. Although we cannot formally prove that these particles were all true 80S ribosomes, we refer to them as such throughout the manuscript. Volumes of single ribosomes (32 x 32 x 32 voxels) were extracted from the reconstructions using bsoft[33].

4.3 Results

4.3.1 Exploring Vitreous Section-Induced Compression at the Macromolecular Level

The effect of vitreous cryo-section-induced compression, at both the cellular and macromolecular level, can be seen in electron cryo-tomographic reconstructed volumes of *S.cerevisiae* cells (Fig. 4.1). The cell in Figure 1a appears to be compressed along the cutting direction (black arrow in Fig. 4.1a'). The cutting axis can be directly inferred from the diamond knife marks (Fig. 4.1a') observed as stripes corresponding to scratches at the top surface of the reconstructed volume. For our analysis on the effect of vitreous section-induced compression at the macromolecular level, we measured the dimensions of individual 80S ribosomes (Fig. 4.1c-e). The dimensions of approximately four hundred 80S ribosomes were measured both parallel and perpendicular (Fig. 4.1d) to the cutting direction (Fig. 4.1a'). The average

height of the ribosomes was measured to be 21 nm ± 2.4 and the width was 22 nm ±

2.5 (Fig. 4.1i). The corresponding 80S ribosome sub-volumes were then summed

(Fig. 4.1e).

4.3.2 Post-Reconstruction Volumetric Transformation

It has been reported that if the three-dimensional volume could be corrected with a

post-reconstruction transformation, the effect of vitreous cryo-section-induced

compression could be compensated[17]. For the reconstructed volume shown in Figure

1a, the vitreous cryo-section thickness was measured directly from the reconstructed

volume to be ~65 nm (original nominal microtome feed was set to 50 nm), which

corresponds to a compression value of ~23%. A similar value was obtained using the

second, independent method for compression measurements described in section

4.2.4.1. Subsequently, a simplified volume-conserving transformation of 23% was

applied to the original reconstructed volume (Fig. 4.1a) along the cutting direction.

The 80S ribosomes that were selected and used for measurements in section 4.3.1

(Fig. 4.1a, c-e, and i) were subsequently measured again in the transformed volume

(Fig. 4.1b, f-h, and j). The particles were measured to be 27 nm ± 3.5 parallel to the

cutting direction (along the transformation plane) and 21 nm ± 2.5 perpendicular to
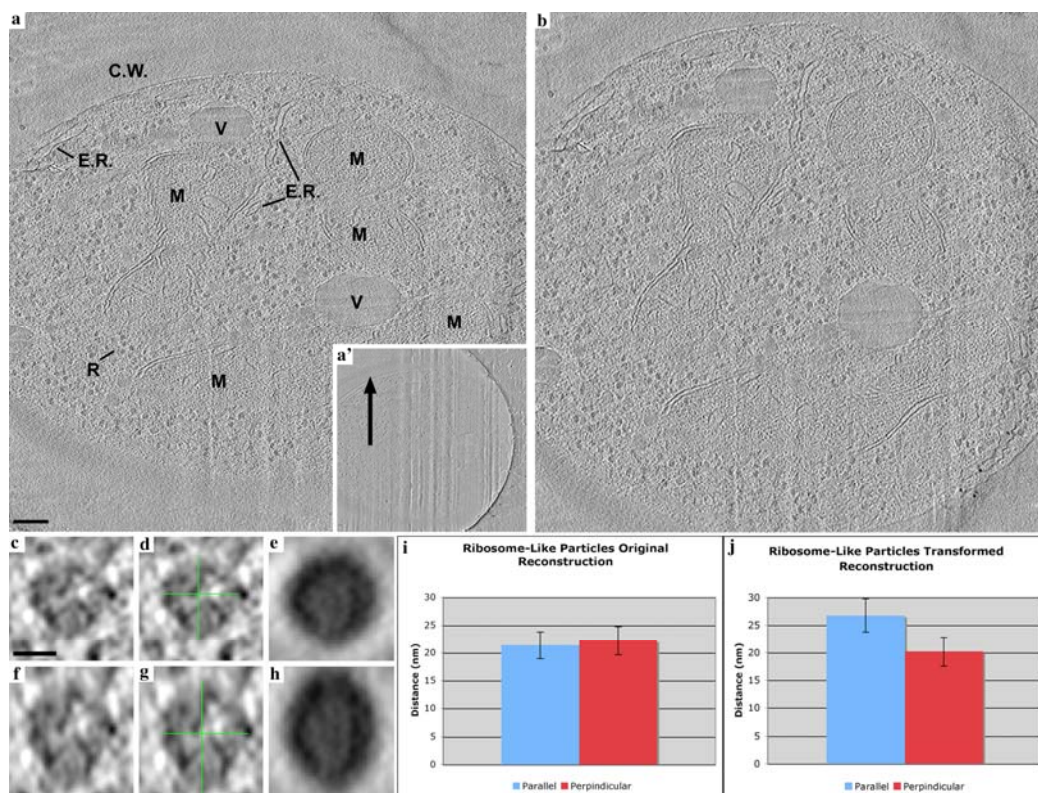
the cutting direction (Fig. 4.1j).

Figure 4.1: Vitreous cryo-section-induced compression explored at the macromolecular level using 80S ribosomes. (a) A 5 nm thick slice through a reconstructed tilt series from a ~ 65 nm thick vitreous cryo-section of an *S.cerevisiae* cell: C.W. – Cell Wall, V – Vacuole, M – Mitochondrion, E.R. – lamellae of Endoplasmic Reticulum, R – cytoplasmic 80S ribosomes. Bar 100 nm. (a') The surface of the reconstructed volume (a) that shows the diamond knife marks used to approximate the cutting direction (black arrow). (b) A simple volume conserving transformation (section 4.2.4.1) was applied to the original reconstructed volume (a) to compensate for vitreous cryo-section-induced compression. (c) A single cross-section of an 80S ribosome sub-volume that was used to measure (d) the dimensions in relation to the cutting direction (denoted in a'). Bar 10 nm. (e) A sum of 400 isolated 80S ribosome volumes from the reconstructed volume (a). The measurements are presented in the graph (i), which displays the relationship between dimensions measured parallel (blue) and perpendicular (red) to the cutting direction. The graph shows that the average height of the 80S cellular ribosomes was measured to be 21 nm ± 2.4, the width 22 nm ± 2.5. The same measurements were done for the transformed volume (b) in (f – h) and presented in the corresponding graph (j). For the 80S ribosomes in the transformed volume, the average height was measured to be 27 nm ± 3.5 and the width to be 21 nm ± 2.5.

4.3.3 Isolated 80S S.cerevisiae Ribosomes

We extended our study from vitreous cryo-sections of whole *S.cerevisiae* to isolated 80S yeast ribosomes. Figure 4.2 shows a comparison of isolated 80S ribosomes that were plunge frozen (Fig. 4.2a and a') and HPF, vitreous cryo-sectioned (Fig. 4.2b and b'). The same volumetric summing method, described in sections 4.3.1 and 4.3.2, was used to analyze electron cryo-tomographic reconstructions of isolated 80S ribosomes. The final 80S ribosome density sum, taken from approximately 300 sub-volumes, from the plunge frozen isolated preparation can be seen in Figure 4.2a'. The density appears spherical (Fig. 4.2a') and the dimensions (~22 nm in diameter), measured in the same way as for the cellular studies (Fig. 4.1), correlate with the cellular 80S ribosome measurements. For vitreous cryo-sectioning experiments, three hundred 80S ribosomes were picked from the reconstructed electron cryo-tomographic volume (Fig. 4.2b) and then summed (Fig. 4.2b'). The dimensions (~22 nm in diameter) again correlate with both cellular studies and also the plunge frozen 80S ribosomal preparation.
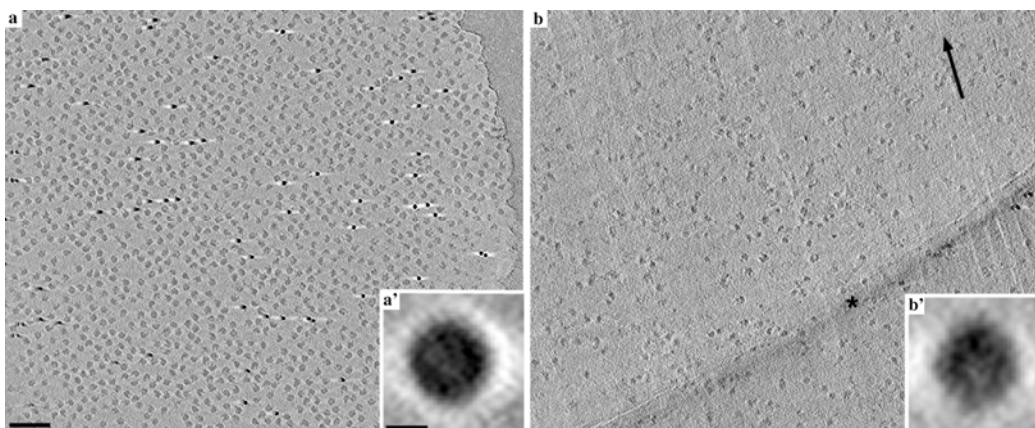
Figure 4.2: Comparison of plunge frozen and HPF, vitreous cryo-sectioned isolated 80S ribosomes. (a) A 5 nm thick slice from a reconstructed volume of isolated, plunge frozen 80S yeast ribosomes. Bar = 100 nm. (a') A summed volume of 300 particles from the reconstruction can be seen in (a). Bar = 10 nm. (b) A 5 nm cross-section from a reconstructed volume of isolated 80S yeast ribosomes that were HPF, vitreous cryo-sectioned. The black arrow denotes the cutting direction on the surface of the section. The asterisk represents a carbon edge of the C-Flat EM grid used to support the vitreous cryo-section during imaging. (b') A summed volume of 300 particles from the reconstruction can be seen in (b).

As a control, we took the single particle average of the 80S ribosome from *S.cerevisiae*[34] (http://www.ebi.ac.uk/pdbe/emdb/ entry emd-1076), resized it to match our experimental imaging conditions, created 400 arbitrarily rotated versions of this template (with and without inclusion of a compression factor), applied the missing wedge, and summed the individual particles. In addition, we applied a translational error of 3 and 5 pixels to mimic the manual particle selection procedure used in our experimental data. The results displayed similar dimensional sums of the 80S ribosomes compared to our experimental data, which confirmed the validity of our experimental approach.

4.4 Discussion

As cellular electron cryo-tomography progresses towards charting macromolecular landscapes[35, 36, 37, 38], tomography of vitreous cryo-sections must play a critical role for investigations of large cells and tissues that are too thick to be imaged *in toto*. The major limitation, however, has been vitreous cryo-section-induced artifacts, which hinder image interpretation. In this report, however, we directly show that 80S ribosomes, both cellular and in an isolated state, can withstand the effect of vitreous cryo-section-induced compression and remain unperturbed at the given resolution limit in their native cellular environment.

In this study we focused our attention on 80S ribosomes, mainly because they have a relatively high inherent contrast level and are therefore easier to detect than other intracellular complexes at the given resolution and signal to noise limits of our experimental data. We propose that large, tightly ordered macromolecular complexes, like the 80S ribosome, can withstand this specific type of mechanically induced deformation, because of its relatively small size (compared to the whole cell) and its structural order. In a similar study, it has been shown that electron diffraction patterns of high pressure frozen vitreous cryo-sectioned lysozyme crystals can extend to 7.9Å[39]. Both studies indicate that after vitreous cryo-sectioning (and all associated section-induced artifacts) structural information can be retained up to the given resolution limit.

We have extended our compression study to other large macromolecular complexes, such as Hemocyanin from *Limulus polyphemus*, which is a respiratory protein complex that binds single oxygen molecules. As with the 80S ribosome, isolated Hemocyanin particles initially appear to withstand the effect of vitreous cryo-section-induced compression. As the technique of electron cryo tomography evolves, these smaller and less abundant macromolecular complexes may be more straightforward to localize in a natural, cellular environment. We suggest doing similar experiments to those we have presented in this report if an in-depth study is desired for an individual protein complex within vitreous cryo-sections.

The optimal vitreous cryo-sectioning conditions are a trade-off between minimizing section-induced artifacts and maximizing biological sampling. For example, thin sections (<50 nm nominal thickness) limit the biological sampling of the specimen, but it also minimizes crevassing[7, 17, 21]. In addition, imaging thin vitreous cryo-sections reduces the amount of electron scattering that contributes to noise, which leads to more accurate image interpretation. Finally, 'crevasse-less', thin vitreous cryo-sections not only appear better but are also less subject to beam-induced movement[40], or 'ironing', of the crevasses during imaging. Reducing beam-induced movement allows for a more accurate and reliable alignment of individual projection images before reconstruction.

An ultimate goal of structural biology is to map the spatial organization of macromolecular complexes within large cells and tissues that cannot be imaged in an intact state. In this report we directly show that large macromolecular complexes, like the 80S ribosome, can withstand the possible artifact-inducing effects of vitreous

cryo-sectioning, therefore the technique will remain valuable for exploring macromolecular landscapes for large cells and tissues that cannot be imaged *in toto*. Finally, for studying the entire spectrum of nanomachines in cells, most of which have dimensions smaller than the 80S ribosome, a number of methodological impediments must be addressed: accurate contrast transfer function corrections, more stringent alignment and classifications techniques during volumetric averaging, improving the sensitivity of electron detectors, and correcting for chromatic lens aberrations to improve image quality.

Acknowledgments

References

1.Dubochet J., Adrian M., Chang J.J., Homo J.C., Lepault J., McDowall A.W., and Schultz P., 1988 Cryo-electron microscopy of vitrified specimens. *Q. Rev. Biophys.* **21**, 129-228.

2. Al-Amoudi A., Chang J.J., Leforestier A., McDowall A., Salamin L.M., Norlen L.P.O., Richter K., Sartori Blanc N., Studer D., and Dubochet J. 2004 Cryo-electron microscopy of vitreous sections. *EMBO J.* **23**, 3583-8.

3. Lucic V., Förster F., and Baumeister W. 2005 Structural studies by electron tomography: from cells to molecules. *Annu. Rev. Biochem.* **74**, 833-865.

4. Pierson J., Sani M., Tomova C., Godsave S., and Peters, P.J. 2009 Toward visualization of nanomachines in their native cellular environment. *Histochem. Cell Biol.* **132**, 253-62.

5. Leforestier A., Dubochet J., and Livolant F. 2001 Bilayers of nucleosomes core particles. *Biophys. J.* **81**, 2414-2421.

6. Matias V.R.F., Al-Amoudi A., Dubochet J., and Beveridge T.J. 2003 Cryo-transmission electron microscopy of frozen-hydrated sections of *Escherichia coli* and *Pseudomonas aeruginosa*. *J. Bacteriol.* **185**, 6112-6118.

7. Zhang P., Bos E., Heyman J., Gnagi H., Kessel M., Peters P.J., and Subramaniam S. 2004 Direct visualization of receptor arrays in frozen-hydrated sections and plunge-frozen specimens of *E. coli* engineered to overproduce the chemotaxis receptor Tsr. *J. Microsc.* **216**, 76-83.

8. Zuber B., Haenni M., Ribeiro T., Minning K., Lopes F., Moreillon P., and Dubochet J. 2006 Granular layer in the periplasmic space of gram-positive bacteria and fine structures of *Enterococcus gallinarum* and *Streptococcus gordonii* septa revealed by cryo-electron microscopy of vitreous sections. *J. Bacteriol.* **188**, 6652-6660.

9. Bouchet-Marquis C., Dubochet J., and Fakan S. 2006 Cryoelectron microscopy of vitrified sections: a new challenge for the analysis of functional nuclear architecture. *Histochem. Cell. Biol.* **125**, 43-51.

10. Schwartz C., Nicastro D., Ladinsky M.S., Mastronarde D., O'Toole E., and McIntosh J.R. 2003 Cryo-electron tomography of frozen-hydrated sections of eukaryotic cells. *Microsc. Microanal.* **9**, 1166-1167.

11. Hsieh C.E., Leith A., Mannella C.A., Frank J., and Marko M. 2006 Towards high-resolution three-dimensional imaging of native mammalian tissue: Electron tomography of frozen-hydrated rat liver sections. *J. Struct. Biol.* **153**, 1-13.

12. Al-Amoudi A., Díez D.C., Betts M.J., and Frangakis A.S. 2007 The molecular architecture of cadherins in native epidermal desmosomes. *Nature* **450**, 832-837.

13. Bouchet-Marquis C., Zuber B., Glynn A.M., Eltsov M., Grabenbauer M., Goldie K.N., Thomas D., Frangakis A.S., Dubochet J., and Chretien D. 2007 Visualization of cell microtubules in their native state. *Biol. Cell* **99**, 45-53.

14. Salje J., Zuber B., and Löwe J. 2009 Electron cryomicroscopy of *E. coli* reveals filament bundles involved in plasmid DNA segregation. *Science* **23**, 509-512.

15. Pierson J., Fernandez J.J., Bos E., Amini S., Gnaegi H., Vos M., Bel B., Adolfsen F., Carrascosa J.L., and Peters P.J. 2010 Improving the technique of vitreous cryo-sectioning for cryo-electron tomography: electrostatic charging for section attachment and implmentation of an anti-contamination glove box. *J. Struct. Biol.* **169**, 219-25.

16. Richter K. 1994 Cutting artifacts on ultrathin cryosections of biological bulk specimens. *Micron* **25**, 297-308.

17. Al-Amoudi A., Studer D., and Dubochet J. 2005 Cutting artifacts and cutting process in vitreous sections for cryo-electron microscopy. *J. Struct. Biol.* **150**, 109-121.

18. Chang J.J., McDowall A.W., Lepault J., Freeman R., Walter C.A., and Dubochet J. 1983 Freezing, sectioning and observation artifacts of frozen hydrated sections for electron microscopy. *J. Microsc.* **132**, 109-23.

19. McDowall A.W., Chang J.J., Freeman R., Lepault J., Walter C.A., and Dubochet J. 1983 Electron microscopy of frozen hydrated sections of vitreous ice and vitrified biological samples. *J. Microsc.* **131**, 1-9.

20. Rigort A., Bäuerlein F.J., Leis A., Gruska M., Hoffmann C., Laugks T., Böhm U., Elbauer M., Gnaegi H., Baumeister W., and Plitzko J.M. 2010 Micromachining tools and correlative approaches for cellular cryo-electron tomography. *J. Struct. Biol.* **172**, 169-79.

21. Han H.M., Zuber B., and Dubochet J. 2008 Compression and crevassing in vitreous sections under different cutting conditions. *J. Microsc.* **230**, 167-171.

22. Studer D., and Gnagi H. 2000 Minimal compression of ultrathin sections with use of an oscillating diamond knife. *J. Microsc.* **197**, 94-100.

23. Al-Amoudi A., Dubochet J., Gnagi H., Luthi W., and Studer D. 2003 An oscillating cryo-knife reduces cutting-induced deformation of vitreous ultrathin sections. *J. Microsc.* **212,** 26-33.

24. Marko M., Hsieh C.H., Schalek R., Frank J., and Mannella C. 2007 Focused-ion-beam thinning of frozen-hydrated biological specimens for cryoelectron microscopy. *Nature Meth.* **4**, 215-217.

25. Hsieh C., He W., Marko M., and Stokes D.L. 2004 3D Tomographic map of desmosome from frozen hydrated skin sections. *Microsc. Microanal.* **10**, 1188CD.

26. Woodcock C.L. 1994 Chromatin fibers observed in situ in frozen hydrated sections. Native fiber diameter is not correlated with nucleosome repeat length. *J. Cell Biol.* **125**, 11-9.

27. Sartori-Blanc N., Senn A., Leforestier A., Livolant F., and Dubochet J. 2001 DNA in human and stallion spermatozoa forms local hexagonal packing with twist and many defects. *J. Struct. Biol.* **134**, 76-81.

28. Elstov M., Maclellan K.M., Maeshima K., Frangakis A.S., and Dubochet J. 2008 Analysis of cryo-electron microscopy images does not support the existence of 30-nm chromatin fibers in mitotic chromosomes in situ. *Proc. Natl. Acad. Sci. USA* **105**, 19732-7.

29. Studer D., Graber W., Al-Amoudi A., and Eggli P. 2001 A new approach for cryofixation by high-pressure freezing. *J. Microsc.* **203**, 285-294.

30. Hauryliuk V., Zavialov A., Kisselev L., and Ehrenberg M. 2006 Class-1 release factor eRF1 promotes GTP binding by class-2 release factor eRF3. *Biochimie* **88**: 747-757.

31. Quispe J., Damiano J., Mick S.E., Nackashi D.P., Fellmann D., Ajero T.G., Carragher B., and Potter C.S. 2007 An Improved Holey Carbon Film for Cryo-Electron Microscopy. *Microscopy and Analysis* **13**, 365-371.

32. Kremer J.R., Mastronarde D.N., and McIntosh J.R. 1996 Computer visualization of three-dimensional image data using IMOD. *J. Struct. Biol.* **116**, 71-76.

33. Heymann J.B., and Belnap D.M. 2007 Bsoft: Image processing and molecular modeling for electron microscopy. *J. Struct. Biol.* **157**, 3-18.

34. Spahn C.M., Beckmann R., Eswar N., Penczek P.A., Sali A., Blobel G., and Frank J. 2001 Structure of the 80S ribosome from *Saccharomyces cerevisiae*—tRNA-ribosome and subunit-subunit interaction. *Cell* **107**, 373-386.

35. Grunewald K., Medalia O., Gross A., Steven A.C., and Baumeister W. 2003 Prospects of electron cryotomography to visualize macromolecular complexes inside cellular compartments: implications of crowding. *Biophy. J.* **100**, 577-591.

36. Ortiz J.O., Förster F., Kürner J., Linaroudis A.A., and Baumeister W. 2006 Mapping 70S ribosomes in intact cells by cryoelectron tomography and pattern recognition. *J. Struct. Biol.* **156**, 334-341.

37. Beck M., Malmstrom J.A., Lange V., Schmidt A., Deutsch E.W., and Aebersold R. 2009 Visual proteomics of the human pathogen *Leptospira interrogans*. *Nat. Methods* **6**, 817-23.

38. Kühner S., van Noort V., Betts M.J., Leo-Macias A., Batisse C., Rode M., Yamada T., Maier T., Bader S., Beltran-Alvarez P., Castaño-Diez D., Chen W.H., Devos D., Güell M., Norambuena T., Racke I., Rybin V., Schmidt A., Yus E., Aebersold R., Herrmann R., Böttcher B., Frangakis A.S., Russell R.B., Serrano L., Bork P., and Gavin A.C. 2009 Proteome organization in a genome-reduced bacterium. *Science* **326**, 1235-40.

39. Sader K., Studer D., Zuber B., Gnaegi H., and Trinick J. 2009 Preservation of high resolution protein structure by cryo-electron microscopy of vitreous sections. *Ultramicroscopy* **110**, 43-47.

40. Sartori Blanc N., Studer D., Ruhl K., and Dubochet J. 1998 Electron beam-induced changes in vitreous sections of biological samples. *J. Microsc.* **192**, 194-201.BB

Chapter 5

Exploring the Bacteriophage T7 infection process using Electron Cryo-Tomography of Vitreous Cryo-Sections

In preparation

Jason Pierson[a], Maria José Rodríguez[b], José Jesús Fernández[b,c], José L. Carrascosa[b], Peter J. Peters[a,d]

[a] Division of Cell Biology II, The Netherlands Cancer Institute – Antoni van Leeuwenhoek Hospital, Plesmanlaan 121, 1066 CX Amsterdam, The Netherlands

[b] Centro Nacional de Biotecnologia – CSIC, Campus Universidad Autonoma, Cantoblanco, 28049 Madrid, Spain

[c] Department of Computer Architecture, University of Almeria, Almeria 04120, Spain

[d] Kavli Institute of Nanoscience, Delft University of Technology, Delft, The Netherlands

Abstract

The fundamental process of genomic transfer from bacteriophage to host cell is a well-established event in the viral infection cycle, but at the structural level it is a dimly understood process. This process for T7 is more interesting because its tail is far too short to span the bacterial cell envelope and also doesn't contract like other phages. Therefore the question remains; how does bacteriophage T7 genome transfer across the host cell's envelope?

Here we use electron cryo-tomography of vitreous cryo-sections to analyze, at a macromolecular level, the bacteriophage T7 host cell interaction. We report that introducing 20% Dextran to the bacteria's normal growth medium doesn't affect its ability to reach exponential growth. In addition, the T7 phage can reach similar infection proficiency in the presence of the Dextran medium. Both full and empty viral capsids could be seen within our cryo-tomographic reconstructed volumes, which we used to guide our analyses towards post-genome transfer viral capsids. Observation of empty viral capsid indicates that T7 uses a protein complex to aid in genome transfer across the bacterial cell envelope. The possible mechanism and procedure for genome transfer is discussed.

5.1 Introduction

Bacteriophage T7 is an elegant viral 'nanomachine' that is a member of the *Podoviridae* family, which infects enteric and other gram-negative bacteria with remarkable efficiency. It has served as an accessible model system for understanding many aspects of molecular biology and macromolecular assembly. Its promoter sequence is used extensively in molecular biology because of its extremely high affinity for RNA polymerase, which leads to high levels of expression. As with other phages, its genome is transferred to the host cell and takes over its machinery to create its progeny. Bacteriophage genome transfer is a highly regulated process and extremely efficient for transferring DNA across bacterial membranes[1].

The virion capsid of bacteriophage T7 is 55 to 60 nm and icosahedral[2]. It contains a genome of linear double-stranded DNA. At one vertex of the icosahedral capsid is the head-tail connector complex (gp8), which has been resolved by cryo-electron microscopy and single-particle analysis to 8 Å[3]. A complex of head proteins, gp16, gp15, and gp14 form an internal, cylindrical structure approximately 26 nm long by 21 nm wide that is attached to the connecter region[4]. A short 23 nm long 'stubby' tail extends from the connector region and is tapered from 21 nm wide at the connector to 9 nm at the distal end[2]. Six tail fibers, each consisting of three parallel gp17 molecules, are attached near the top of the tail[5, 6].

The classic mode of infection has been based on experiments using phages T2, T4 and T5 as a model system. From these experiments it remains widely accepted that the process of phage infection involves absorption, phage tail contraction, and DNA

transfer into the host cell. However, recently it has been recognized that this classical process of infection cannot hold true certain members of the *Podoviridae* family, specifically bacteriophage T7[7]. Translocation of DNA across bacterial envelope is a key aspect of the survival of bacteriophages, but also for several other biological processes including conjugative DNA transfer, genetic transformation, and t-DNA transfer from bacteria to plant cells[8]. For bacteriophage T7, the structural components that aid in genome transfer is dimly understood.

Initial attachment, or T7 absorption to the host cell, is guided by six tail fibers, each consisting of three parallel gp17 molecules, which are connected to the phage near the top of the tail unit[9]. The phage probes the surface of the host cell, reversibly binding to lipopolysaccharides (LPS) on the outer membrane, searching for an outer membrane cellular component, however the specific cellular receptor responsible for T7 binding has not been established. The tail component likely irreversibly binds to the cellular components establishing a proper orientation to the host cell. At this time gp7.3 and gp6.7 are ejected and are degraded by the host cell.

A large majority of bacteriophages have relatively long and contractile tails, which can be used to 'inject' the genome directly into the host cell. The tail acts as a conduit preventing harmful periplamic endonucleases to access the genome. However, for a select few bacteriophages, such as T7, the tail is short and stubby[10]. In addition, the tail is non-contractile, a feature that is unique for the *Podoviridae* family. Therefore the important question remains, how does T7 transfer its genome with a non-contractile, short and stubby tail? The mode of infection has been predicted to involve a trans-membrane protein channel constructed by the internal core proteins of T7,

gp14, 15, and 16[11, 12] or an extensible tail[4, 13], but structural evidence for such a channel has not been established.

Electron cryo-microscopy, and its extension to three-dimensional imaging using tomography, is a technique that overcomes the limitations and preparation artifacts that are associated with conventional electron microscopy[14]. Vitreous cryo-sectioning combined with electron cryo-tomography[15, 16] has evolved into a suitable technique for imaging cells and pieces of tissue in a close-to-native state, and at molecular resolutions, that are often too large to be viewed *in toto*.

In this study, we employed electron cryo-tomography of vitreous cryo-sections to observe the T7 infection process. We observe three distinct infection 'states' for the bacteriophage capsid: a full capsid, an empty capsid, and a residual body. In addition we observe that the outer membrane is pinched towards the inner membrane of the host cell. Finally, we show direct evidence of protein complexes within the host membrane, which could be part of a possible genome transfer complex. This study has not only shed light on the mechanism of genome transfer for T7, but also provides insights to understand how nucleic acids pass through a bacterial lipids membrane system with the aid of transmembrane protein complexes.

5.2 Methods

5.2.1 Sample Preparation

Escherichia coli strain BL21 was grown in LB media supplemented with 20% Dextran (w/v) (from *Leuconostoc mesenteroides*, 35-45 kDa; Sigma Chemical, St. Louis) at 37°C in an incubator shaker to an O.D. of 0.400. Bacteriophage T7 at a titer of 1 x 10^{12} pfu/mL was added to the bacteria for a final M.O.I. of 100. The infection time was taken directly after addition to the *E.coli*. Samples were taken after addition of T7 to the *E.coli* culture and subsequent 5 min. centrifuge to obtain a highly concentrated pellet. The pellet was resuspended and taken up into a copper tube (inner ø 350 μm) as described[17], and vitrified using an EM-PACT2 high-pressure freezing machine (Leica Microsystems, Vienna). The pressure reached 2000 bar within 15 ms and had a nominal cooling rate of ~20,000 °C s^{-1}. After freezing, the copper tubes were stored in liquid nitrogen.

5.2.2 Vitreous Cryo-Sectioning

Vitreous cryo-sections were obtained as described in Pierson et al., 2010. Briefly, a single copper tube was transferred to a pre-cooled (-150 ºC) EM FC6 cryo-ultramicrotome (Leica Microsystems, Vienna). An anti-contamination glove box, the 'Cryosphere' (Leica Microsystems, Vienna) was placed around the microtome in order to reduce the humidity levels within and around the microtome. Ribbons of vitreous cryo-sections were made using a 35º cryo-diamond knife (Diatome, Biel, Switzerland) with a clearance angle of 6º. Ribbons were attached using electrostatic

charging[18] to a pre-treated C-Flat™ EM grids CF-2/2-2C[19] (Aurion, Wageningen, The Netherlands). Ribbons were produced at a nominal cutting feed of 30-50 nm at cutting speeds ranging from 1 to 100 mm/s.

5.2.3 Electron Cryo-Tomography

The vitreous cryo-sections were imaged using a Tecnai 12 TEM (FEI, Eindhoven, The Netherlands). Images were recorded at 120 kV at a liquid nitrogen temperature on a 4x4 kV FEI Eagle CCD camera (FEI, Eindhoven, The Netherlands). Single axis tilt series were collected using FEI Xplore3D (FEI, Eindhoven, The Netherlands) acquisition program under low dose conditions. The angular tilt range was typically set from -60º to +60º with a 1.5º - 2º tilt increment. The objective lens was defocused to -4.5 to -6.5 μm. Total dose for the entire tilt series was kept below ~100e/$Å^2$. The nominal magnification was 23000x, which resulted in a 0.45 nm pixel size. Single projection images were placed into register using 10 nm gold fiducial markers applied to the carbon support film on the C-Flat EM grid, the aligned stack was reconstructed (R-weighted back projection) using the IMOD package[20]. General visualization and surface rendering was preformed using Amira (http://www.amiravis.com/).

5.3 Results

5.3.1 Achieving Proper Freezing and Vitreous Sectioning Conditions

5.3.1.1 Bacterial Growth in the presence of 20% Dextran

A cryo-protective agent is often supplemented to a cellular suspension in order to enhance the freezing of the extracellular media and facilitate vitreous cryo-sectioning[21]. The cryo-protective agent should have little effect on cellular growth when introduced into the media. In this study we used 20% Dextran (wt/vol; average 35-45 kDa) as our primary cryo-protecting agent. We measured the optical density, used to estimate the cellular mass within a volume, for *E.coli* strain BL21 in the presence of 20% Dextran that was supplemented into the normal LB media.

Figure 5.1 shows growth curves over time for *E.coli* strain Bl21 (Fig. 5.1a) and strain *Su-* (Fig. 5.1b) cells growing in normal LB media (Control (LB) dark blue line), that was supplemented with 20% Dextran during the re-suspension from an overnight culture growing in normal LB media (Dextran (O/N in LB purple line), and media that was supplemented with 20% during the overnight culture (Dextran (O/N in Dextran) yellow line). In both strains of *E.coli*, the bacteria reached mid-log phase (OD600 ~0.7) within 90 minutes when cultured in normal LB media (Fig. 5.1a and b – blue lines). For both conditions where Dextran was used (supplemented in the overnight culture media and in the resuspension media), the cells reached mid-log phase (OD600 ~0.7) slower than in the control (Fig. 5.1a and b – purple and yellow

lines). Although cellular growth showed a slower rate of doubling, the cells nevertheless successfully reached log phase.
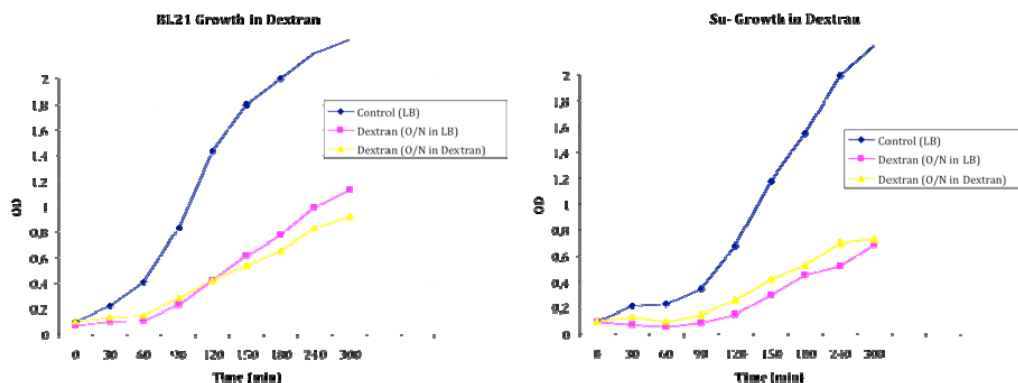

Figure 5.1: Cellular growth in the presence of the cryo-protectant Dextran. Growth curves for *E.coli* strain BL21. The blue lines in both graphs represent a control growth curves for BL21 grown in the presence of normal media. The pink curves represent Bl21 that have been grown in normal media overnight and then resuspended in LB+20% Dextran and grown to log phase. The yellow curves are BL21 that have been grown overnight in LB + 20% dextran. The right graph displays a different strain of *E.coli, Su-*. As indicated in the graphs, the growth to log phase is slower in the presence of dextran but both type of cells are still able to reach the log phase of the cell cycle, indicating that the cells are steadily dividing.

5.3.1.2 Bacteriophage T7 production in the presence of 20% Dextran

In addition to measuring the affects of Dextran on normal bacterial cellular growth, we also examined its effect on phage infection and production shown in Figure 5.2. The two graphs each display the production of phage forming units (pfu) over time (min.). Both total culture (Blue line) and supernatant (purple line) measurements were done to follow phage production in the presence of Dextran. Total culture (Blue line) is a measurement of the total virus titer and measures the total virus present in the

culture at the indicated time, both viruses present in the inside and outside of the cells.

The supernatant (Purple line) relates to the viruses titrated in the outside of the cells.
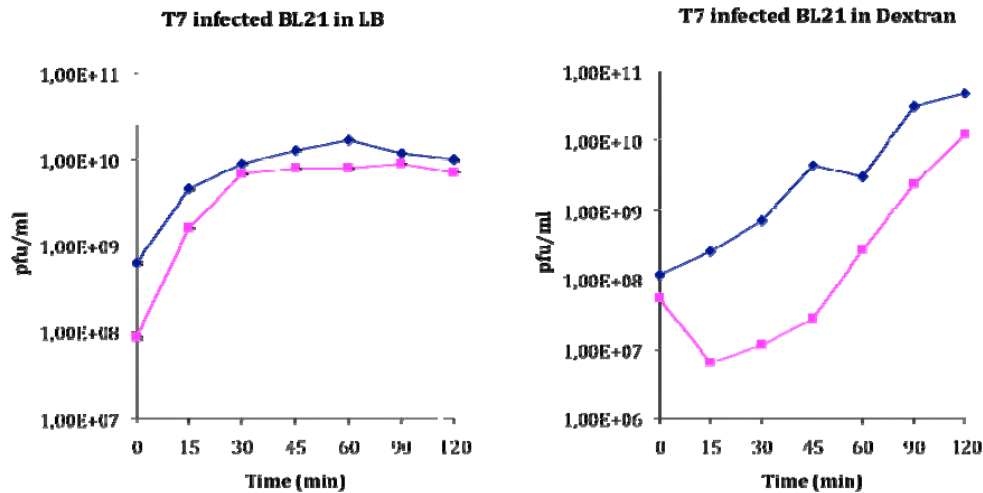

Figure 5.2: Phage infectivity in the presence of Dextran. The left graph displays the virus production curves in normal LB media. The blue line represents the total virus titer, which measures the total amount of virus present in the culture at the indicated times i.e. those present inside and outside the cells. The pink curve relates to the viruses titrated in the outside of the cells, i.e. viruses already freed from infected and lysed cells. This measures viable viruses that are released in the medium by the infected bacteria. Most of the viruses produced are released in the media without problems. The right graph shows the same experiments with the addition of 20% dextran in the media. The virus production is delayed with respect to the control in LB, but the virus is produced at a similar titer, although again like in the bacterial growth curves, slower than the control situation.

The left graph displays phage production in the presence of normal growth media for *E.coli* infected with T7. The right graph displays a similar experiment, however in these experiments the normal medium was supplemented with 20% Dextran. As depicted in the graphs, the virus production is delayed with respect to the control;

104

nevertheless the virus is still produced at a similar titer. In addition, the release of the virus from the infected bacteria is also delayed with respect to the control (compare the purple and dark blue curves). Other than the delayed virus production, the graphs display normal infection cycle and virus production kinetics with Dextran supplemented in the normal growth media.

5.3.2 Three-dimensional visualization of bacteriophage T7 infecting *E.coli* by electron cryo-tomography of vitreous cryo-sections

To examine the structural components of the T7 tail, *E.coli* strain BL21 was infected with T7 at a multiplicity of infection (M.O.I.) of 100. A high MOI was a critical step in the preparation of the sample to ensure that the T7 tail complex was present within our thin (~50 nm) vitreous cryo-sections.

At low magnifications, *E.coli* cells were visible and the quality of both the freezing and vitreous sectioning could be estimated. On closer examination of the cells we found that a majority of the cells contained electron dense spheres surrounding the periphery of the outer cell membrane as seen in Figure 5.3. The electron dense spheres are presumed to be the T7 capsids in the process of infection. The T7 phage capsids were evenly dispersed around the host cell. In some cases we observed multiple phage capsids surrounding the host cell as in Figure 5.3.
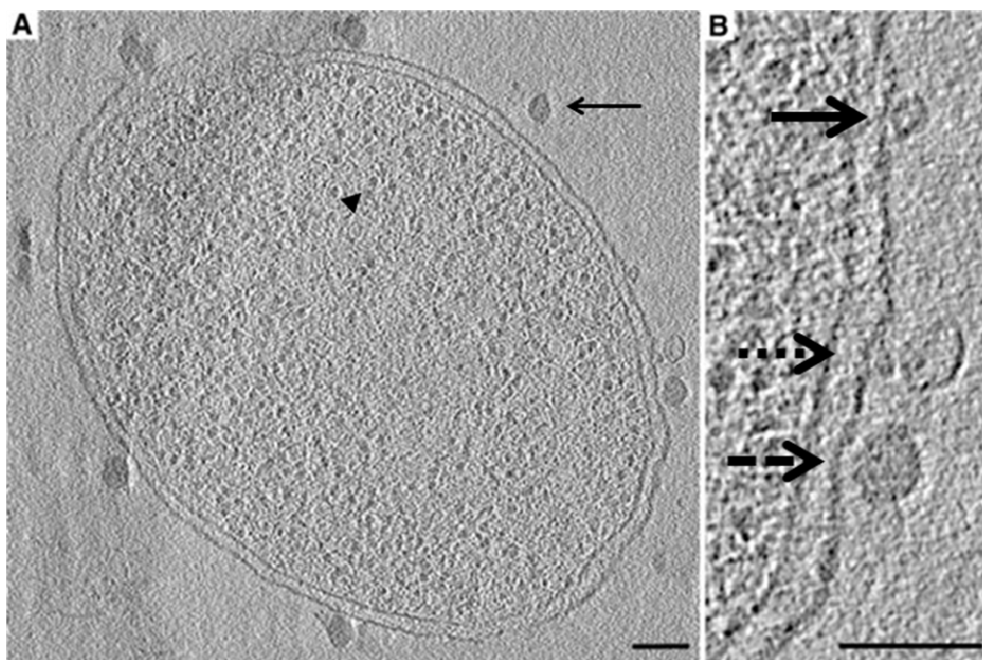
Figure 5.3: (A) A 5 nm slice from an electron cryo-tomographic reconstructed volume from a vitreous cryo-section of *E.coli* infected with bacteriophage T7. The quality of the reconstructed volume can be seen from the ability to resolve 70S ribosomes within the cell (black arrowhead). Bacteriophage T7 capsids can be seen surrounding the bacteria (black arrow) within the vitreous cryo-section. **(B)** Three distinctive viral capsid phenotypes were observed; full capsids (two dashed black arrow), empty capsids (four dashed black arrow), and partially empty capsids (black arrow).

Although single projection images were sufficient to recognize the bacteria and the T7 capsids, tomography was preformed to obtain a three-dimensional view of the T7 infected bacteria. Based on tilt series alignment and reconstruction quality, we selected and analyzed 18 tomograms of vitreous-sectioned *E.coli* that were infected with bacteriophage T7. Quality reconstructions were selected based on tilt series acquisition, alignment and reconstruction. In these reconstructions, multiple T7 phage particles could be observed associated with the bacterial cell wall. Figure 5.3a shows

a 5 nm slice through a reconstructed tomogram of a vitreous cryo-section of an *E.coli* bacterium that has been infected with the T7 phage.

Three distinctive viral capsid phenotypes were observed (Fig. 5.3b); (1) full capsid which presumably contains enough phage genome to appear more electron dense than other capsid, (2) empty capsids which appear devoid of its genome and (3) partially empty capsids which appear smaller than the normal empty or full capsids observed. Of the tomograms that were screened, we analyzed 52 full capsids, 18 empty capsids, and 18 partial ones.

5.3.3 The outer membrane of the host cell appears pinched toward the inner membrane at a number of T7 infection sites

From the reconstructed volumes we were able to measure the average dimensions for the bacteriophage T7 capsid, the distance from the base of the capsid to the outer membrane of the host cell, and also the outer membrane of the host cells to the inner membrane. Figure 5.4 shows a comparison of full capsids with empty ones associated with the outer membrane of the host cell. At a number of infections sites, the outer membrane is pinched towards the inner membrane by ~8 nm. Measurements were done at membranes parallel to the cutting direction to reduce the bias of vitreous cryo-section induced compression[22]. The bulk envelope, absent of any T7 phage interaction, was measured to be ~ 27.5 nm and the T7 associated envelope was measured to be 19.1 nm.
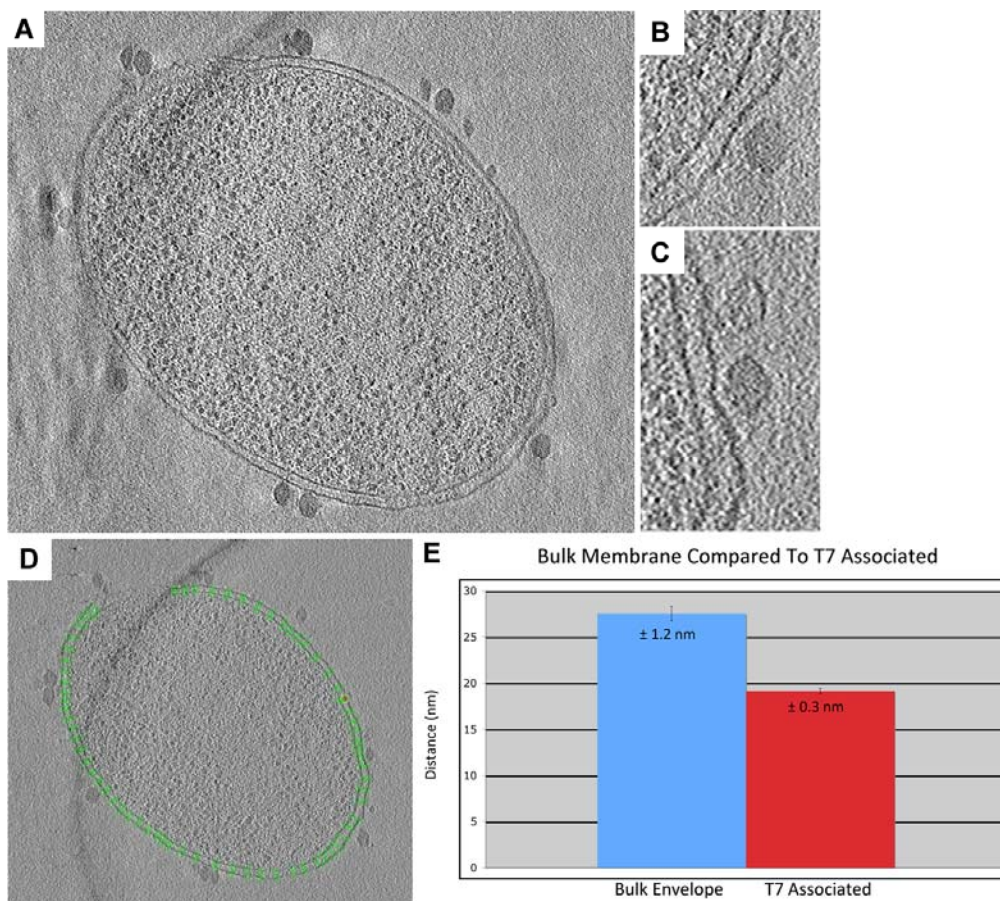
Figure 5.4: (A) 5 nm slice from an electron cryo-tomographic reconstructed volume from a vitreous cryo-section of *E.coli* infected with bacteriophage T7. At a number of infections sites, the outer membrane is pinched towards the inner membrane (A-C). We measured the bulk envelope in relation to the envelope at the infection site (D) and observed a difference in the distance from the outer membrane to the inner membrane, which results in a pinched envelope at the infection site by ~8 nm. We notice that the bulk envelope, absent of any T7 phage interaction, was measured to be ~ 27.5 nm and the T7 associated envelope was measured to be 19.1 nm.

In addition to measuring the altered membrane at infection site, we also measured the dimensions of full and empty capsids, along with distance to the host cell outer membrane in all the reconstructed volumes. Figure 5.5 shows a subsequent reconstructed volume including capsid dimensions. The average full capsid dimensions were measured to be 48.7 nm in width and 60.5 nm in length. The

distance from the base of the capsid to the outer membrane was measured to be 14.7 nm for both empty and full capsids that were perpendicular to the cutting directions.
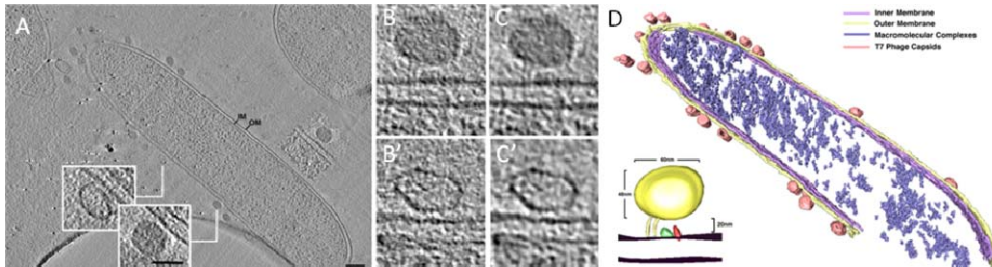

Figure 5.5: (A) A 5 nm slice from an electron cryo-tomographic reconstructed volume from a vitreous cryo-section of *E.coli* infected with bacteriophage T7. Insets are high magnification of phage interaction sites. (B, B', C, C') Similar enhanced magnification views of a select infection site with (B' and C') and without non-linear anisotropic denoising (B and C). (D) An isosurfaced view from (A). The dimensions of full and empty capsids, along with distance to the host cell outer membrane in all the reconstructed volumes were also measured. The average values of the full capsid dimensions were measured to be 48.7 nm in width and 60.5 nm in length. The distance from the base of the capsid to the outer membrane was measured to be 14.7 nm for both empty and full capsids.

5.3.4 A glimpse to the Bacteriophage T7 genome transfer complex

The most important step in the phage infection cycle is successful genome transfer to the host cell. Figure 5.5 shows a 5 nm slice from a reconstructed volume of an *E.coli* host cell infected with T7. Notice that we are able to visualize both full capsids and empty ones (see insets 5.5A). Although we didn't notice any striking features that could constitute a membrane-spanning channel, there are hints to protein densities that appear to be localized at the surface of the membrane in Fig. 5.5B – D. C and C' display higher magnification, denoised[23] (non-linear anisotropic diffusion), images from the tomographic reconstruction. At the surface of the outer membrane of the

host cells and below the capsid there are electron densities that could represent initial structural components involved in host cell interaction or the first stages of constructing a putative T7 tail complex.

A subsequent tomographic reconstruction shown in Figure 5.6 reveals 2 distinct protein complexes associated with the T7 phage infection site that lies within the outer and inner membrane of the host cell. Fig. 5.6 A is a 5 nm slice through a reconstructed volume that contains a T7 phage in the upper right corner, B shows a high magnification image of the representative area, C shows a denoised version of B, and D show the surface rendering of the select area from B and C. In the original high magnification image B we can already start to see electron densities associated with the phage that pass into the outer and inner membrane. In the denoised version, the complexes are retained and visualized more clear than in C. The purple rendered densities in D represent putative membrane complexes that have been introduced by the T7 bacteriophage and could be involved in the process of genome transfer.

5.4 Discussion

Electron cryo tomography of vitreous cryo sections remains the most suitable technique for three-dimensional visualization of cells and tissue in a close-to-native, fully hydrated state that are too large for normal plunge freezing, this technique was utilized to observe the bacteriophage T7 infection process in a cellular, and close-to-native environment.
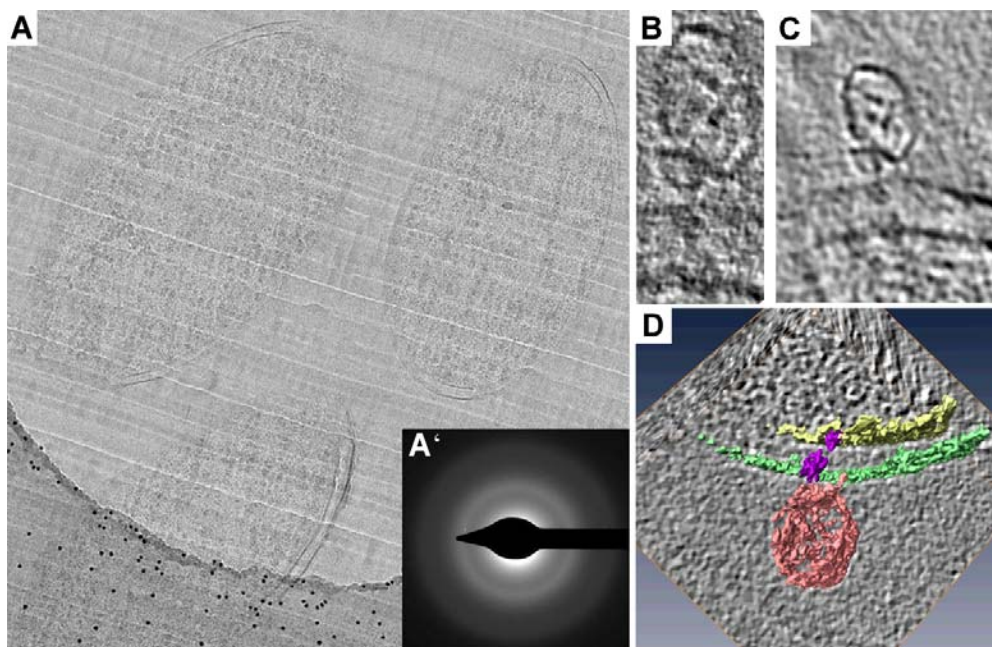
110

Figure 5.6: (A) 5 nm slice of an electron cryo-tomography reconstructed volume from a vitreous cryo-section of *E.coli* infected with bacteriophage T7. A' displays a select area diffraction pattern from A. B and C display an enhanced magnification view of a select phage infection site from A, with (C) and without (B) non-linear anisotropic denoising. (D) A surface rendered view of C. The red color denotes the empty viral capsid, green is the outer membrane of the bacterial envelope, yellow is the inner membrane, and purple indicates unidentified protein complexes that are associated with the infection site.

5.4.1 Sample preparation for Electron Cryo-Tomography of Vitreous Cryo-Sections

Proper vitrification is paramount in all electron cryo-tomography studies. For vitreous cryo-sectioning Dextran solutions have been used in the past for successful protection of the extracellular media[21]. However, in current protocols, Dextran has been introduced directly before freezing, often by resuspending the pellet of cells in a Dextran solution. These methods raise the concern that Dextran may still create an imbalanced solution or slight shock to the cells, although it theoretically cannot

111

penetrate into cells because of high molecular weight and branching properties. In our report, we have tested the effect of Dextran on bacterial cells in the normal growth media. By doing so, the cells can acclimate to the foreign substance during growth rather than presumably 'shocking' the cells directly before freezing. We conclude that because the cells are able to reach exponential log phase of the cell cycle, similar to the wild type conditions, the cells are not noticeably disturbed and suitable for high pressure freezing.

5.4.2 Electron Cryo-Tomography of Bacteriophage T7 infecting *E.coli*

Within the reconstructed tomography volumes of the T7 infection preparation we visualized actively infecting phages associated with the outer membrane of the host *E.coli* cell. Three distinctive phenotypes were observed within the majority of the reconstructed volumes: A full capsid, an empty one, and a residual body. We base this observation on the fact that putative full capsid scatter the electrons more strongly, in turn creating a higher level of contrast in the resulting image then empty capsids. The next step would be to use high-resolution electron tomography to directly visualize the T7 genome within the capsid and possibly do some elegant averaging based to the highly repetitive nature of the phage's genome. A complication may be the conformational variability in the T7 capsid and proteins involved during infection. Multivariable statistical classification would be required to sort each conformation class in order to obtain the full spectrum of the infection cycle at high resolution.

We used the contrast level of the phage capsid to separate empty phages from full ones. At the highest contrast level, the phage is presumably not actively infecting and

the contrast level should be the same as an isolated, non-infecting, capsid. But as the genome is being transferred into the host cell, and for T7 it takes a bout ~10 minutes[24], the contrast will decrease with the amount of genome has been transferred. This would be a key localization tool or determining if the T7 phage is actively infecting the host cell. Of course if the contrast level is low then we can assume that the genome has been completely transferred and this is also corroborated with the T7 capsid structurally disassembling, which could explain the observation of partial, or smaller, capsid residual structures.

Interestingly, full T7 phage capsids appeared to resist section induced compression more than capsids that were empty (Fig. 5.5 insets). The difference in dimensions could be due to the presence of DNA with the capsid that provides a more stable capsid and therefore the compression rates would differ. Or, another possible explanation could be that the dimensions of empty capsids are different than filled capsids independent of mechanical sectioning. Once the genome is released the capsid would be structurally altered and appear 'compressed.' We have observed similar non-uniform compression levels in *Saccharomyces cerevisiae* 80S ribosomes[31]. In this study, the resistance to compression may be due to the structural support of the genome within the T7 capsid.

5.4.3 Bacteriophage T7 infection process

5.4.3.1 Absorption

In this report we have observed indications for a possible structure that aids in transferring T7 genome. In figure 7 we provide a schematic diagram that incorporates our observations into the bacteriophage T7 infection scheme.

In figure 5 we believe that the T7 phage in panels B and C is in an early conformation of its infections cycle. Specifically, that in this state the phage has presumably not released its pore forming tail components into the host cell membranes and therefore we wouldn't expect the membranes to be pinched. After initial screening done by the T7 tail fibers reversibly binding to lipopolysacchardes (LPS) on the surface of the host cell, the phage irreversibly binds to a cellular component that has yet to be described. The T7 related phage T5 for instance, targets the envelope protein FhuA for irreversible binding[25]. Subsequently a myriad of protein complexes, which include gp14, 15, and 16, are ejected from the virion on the surface and into the outer membrane of the host cell[26].

The ability to resolve protein complexes associated with the host envelope in single sub-volumes is the result of the thin vitreous cryo-section and quality of the tomographic alignment and reconstruction. In the future it would be helpful to average sub-volumes of phage-host interaction sites in order to improve the resolution and subsequent interpretation; however, a very robust classification method must be used in order to sort all of the conformations into unique classes.

5.4.3.2 Channel Formation

Both Fig. 5.5 and Fig. 5.6 show empty capsids presumably in the latter stages of infection and putative proteins complexes can be seen on the surface and within the host cell membranes. These protein complexes may be a combination of the gp proteins involved in creating a genome-transferring complex. Due to the fact that there is not a suitable method for labeling or localizing proteins and macromolecular complexes in vitreous cryo-sections, it is difficult to speculate which proteins are involved in T7 phage genome transfer purely from observational data. In the near future we hope to combine these observational results with both biochemistry, in the form of yeast-two hybrid to probe for the interaction between T7 proteins and host cell outer membrane receptors[27, 28] and immuno labeling of tokyushu thawed cryo sections to localize the proteins involved in creating a possible trans-membrane protein channel.

In some areas of infection we observed the outer bacterial envelope membrane to be pinched towards the inner membrane. Although this observation was not present at each infection site, it may provide an explanation for the success of T7 genome transfer. If the bacterial envelope is reduced to ~19 nm this would be sufficient for the intact tail, or associated proteins complexes, to bypass the bacterial envelope for genome transfer into the cell. A similar disruption of the host cell membranes has been seen for the marine podovirus P-SSP7 infection *Prochlorococcus marinus*[29]. In our study, the large number of viral conformations during infection could explain why this observation is not seen at each infection site.

A possible explanation for the membrane pinching may be due to the refolding of gp15 and 16. These proteins are very large and therefore are presumed not to exist in a tertiary structure as they exit the virion[13], but contain enough structural integrity to refold once ejected into the host's envelope, presumably because gp16 acts like a 'carpenters ruler.' A putative channel is then formed in the envelope and the genome is subsequently transferred. Although we didn't observe a full channel or tube like structure in the envelope of the host cell at the infection sites, we did observe proteins and proteins complexes that may contribute to the process of genome transfer. Whole cell electron cryo tomography of T7 infecting *E.coli* may be used to observe such structures in the future, albeit at limited resolving power. The presumably gp15/16 complex assists with the transfer of the genome into the host cell by a motor like process[30]. At the end of the genome, gp16 attached to the genome enters the cell and therefore the cellular envelope may resumes its original geometry, which could explain the non-pinched membrane state associated with the empty capsid infection sites.

As we have seen, electron cryo-tomography of vitreous cryo-sections allows a glimpse into the infection method of bacteriophage T7 in a close-to-native and fully hydrated condition.
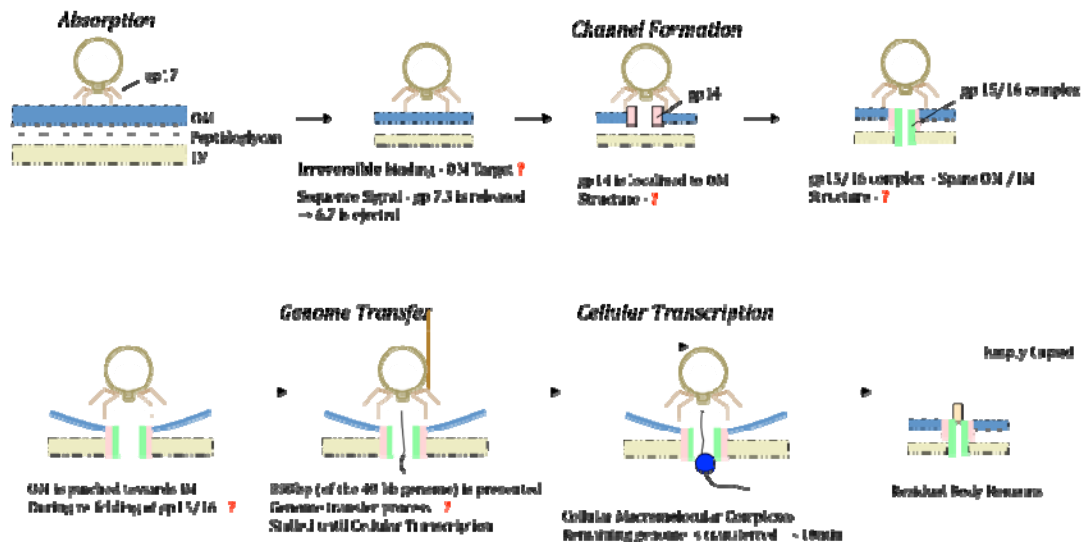
Figure 5.7: A schematic that shows bacteriophage T7 infection with the data presented incorporated.

Acknowledgements

References

1. Johnson J.E., and Chiu W. 2007 DNA packaging and delivery machines in tailed bacteriophages. *Curr. Opin. Struct. Biol.* **17**, 237-243.

2. Steven A.C., and Trus B.L. 1986. The structure of bacteriophage T7, pp. 1-35. In J.R. Harris and R.W. Horne (eds.) Electron Microscopy of Proteins, vol. 5: Viral Structure. Academic Press, New York.

3. Agirrezabala X., Martin-Benito J., Caston J.R., Miranda R., Valpuesta J.M., and Carrascosa, J.L. 2005 Maturation of phage T7 involves structural modification of both shell and inner core components. *EMBO J.* **24**, 3820-3829.

4. Serwer P., Wright E.T., Hakala K.W., and Weintraub S.T. 2008 Evidence for bacteriophage T7 tail extension during DNA injection. *BMC Research Notes* **1**, 36.

5. Kato H., Fujisawa H., and Minagawa, T. 1986 Subunit arrangement of the tail fiber of bacteriophage T3. *Virology* **153**, 80-86.

6. Steven A.C., Trus B.L., Maizel J.V., Unser M., Parry A.D., Wall J.S., Hainfld J.F., and Studier, F.W. 1988 Molecular substructure of a viral receptor-recognition protein. The gp17 tail-fiber of bacteriophage T7. *J. Mol. Biol.* **200**, 351-365.

7. Grayson P., and Molineux, I.J. 2007 Is phage DNA "injected" into cells − biologists and physicists can agree. *Curr. Opin. Microbiol.* **10**, 401-409.

8. Dreiseikelmann, B. 1994 Translocation of DNA across bacterial membranes. *Microbiology Reviews* **58**, 293-316.

9. Steven A.C., Trus B.L., Maizel J.V., Unser M., Parry D.A., Wall J.S., Hainfeld J.F., and Studier, F.W. 1988. Molecular substructure of a viral receptor-recognition protein. The gp17 tail-fiber of bacteriophage T7. *J. Mol. Biol.* **125**, 75-93.

10. Agirrezabala X., Martin-Benito J., Valle M., Gonzalez J.M., Valencia A., Valpuesta J.M., and Carrascosa, J.L. 2005. Structure of the connector of bacteriophage T7 at 8 Å resolution: Structural homologies of a basic component of a DNA translocating machinery. *J. Mol. Biol.* **347**, 895-902.

11. Molineux I.J. 2006 The T7 group. In: Calendar, R. (Ed.), The Bacteriophages. Oxford University Press, New York, pp. 277-301.

12. Molineux, I.J. 2006. Fifty-three years since Hershey and Chase; much ado about pressure but which pressure is it? *Virology* **344**, 221-229.

13. Molineux I.J. 2001 No syringes please, ejection of phage T7 DNA from the virion is enzyme driven. *Mol. Micro.* **40**, 1-8.

14. Lucic V., Forster F., and Baumeister W. 2005 Structural studies by electron tomography: From cells to molecules. *Annu. Rev. Biochem.* **74**, 833-65.

15. Al-Amoudi A., Diez D.C., Betts M.J., and Frangakis A.S. 2007 The molecular architecture of cadherins in native epidermal desmosomes. *Nature* **450**, 832-7.

16. Pierson J., Sani M., Tomova C., Godsave S., and Peters P.J. 2009 Towards visualization of nanomachines in their native cellular environment. *Histochem. Cell Biol.* **132**, 253-262.

17. Studer D., Graber W., Al-Amoudi A., and Eggli P. 2001 A new approach for cryofixation by high-pressure freezing. *J. Microsc.* **203**, 285-294.

18. Pierson J., Fernandez J.J., Bos E., Amini S., Gnaegi H., Vos M., Bel B., Adolfsen F., Carrascosa J.L., and Peters P.J. 2010 Improving the technique of vitreous cryo-sectioning for cryo-electron tomography: electrostatic charging for section attachment and implmentation of an anti-contamination glove box. *J. Struct. Biol.* **169**, 219-25.

19. Quispe J., Damiano J., Mick S.E., Nackashi D.P., Fellmann D., Ajero T.G., Carragher B., and Potter C.S. 2007 An Improved Holey Carbon Film for Cryo-Electron Microscopy. *Microscopy and Analysis* **13**, 365-371.

20. Kremer J.R., Mastronarde D.N., and McIntosh J.R. 1996 Computer visualization of three-dimensional image data using IMOD. *J. Struct. Biol.* **116**, 71-76.

21. Dubochet J., Adrian M., Chang J.J., Homo J.C., Lepault J., McDowall A.W., and Schultz P. 1988 Cryo-electron microscopy of vitrified specimens. *Q. Rev. Biophys.* **21**, 129-228.

22. Millen J.I., Pierson J., Kvam E., Olsen L.J., and Goldfarb D.S. 2008 The luminal N-Terminus of yeast Nvj1 is an inner nuclear membrane anchor. *Traffic* **9**, 1653-1664.

23. Frangakis A.S., and Hegerl, R. 2002. Noise reduction in electron tomographic reconstructions using nonlinear anisotropic diffusion. *J. Struct. Biol.* **135**, 239-50.

24. Garcia L.R., and Molineix, I.J. 1995. Rate of translocation of bacteriophage T7 DNA across the membranes of *Escherichia coli*. *J. Bacteriol.* **177**, 4066-4076.

25. Bohm J., Lambert O., Frangakis A.S., Letellier L., Baumeister W., and Rigaud J.L. 2001 FhuA-mediated phage genome transfer into liposomes: A cryo-electron tomography study. *Current Biology* **11**, 1168-1175.

26. Kemp P., Garcia L.R., and Molineux, I.J. 2005 Changes in bacteriophage T7 virion structure at the initiation of infection. *Virology* **340**, 307-317.

27. Bartel P.L., Roecklein J.A., SenGupta D., and Fields S. 1996 A protein linkage map of Escherichia coli bacteriophage T7. *Nature Genetics* **12**, 72-77.

28. Roucourt B., Lecoutere Chibeu A., Hertveldt K., Volckaert G., and Lavigne R. 2009 A procedure for systematic identification of bacteriophage-host interactions of *P. aeruginosa* phages. *Virology* **387**, 50-58.

29. Liu X., Zhang Q., Murata K., Baker M.L., Sullivan M.B., Fu C., Dougherty M.T., Schmid M.F., Osburne M.S., Chisholm S.W., and Chiu, W. 2010 Structural changes in a marine podovirus associated with release of its genome into *Prochlorococcus*. *Nat. Struct. Mol. Biol.* **17**, 830-6.

30. Chung-Yu C., Kemp P., and Molineux I.J. 2009 Gp15 and gp16 cooperate in translocating bacteriophage T7 DNA into the infected cell. *Virology* **15**, 176-86.

31. Pierson J., Ziese U., Sani M., and Peters P.J. Exploring vitreous cryo-section-induced compression at the macromolecular level using electron cryo-tomography; 80S yeast ribosomes appear unaffected. *J. Struct. Biol.* **173**, 345-9.

Summary and Discussion

Title: Electron Cryo-Tomography of Vitreous Cryo-Sections: Towards Imaging Biological Nanomachines in their Cellular Environment

The field of biological electron microcopy (EM) has evolved into a reliable imaging technique for examining the ultrastructure of cells and their constituents at molecular, and, in some cases, atomic[1, 2] resolution. Conventional EM techniques are being overshadowed by cryo-techniques, which ensure a more native cellular preparation method. In addition, electron tomography eliminates the projection problem of single EM images and adds a third dimension to the analysis. The cryo-preparation technique combined with tomography is currently the most suitable technique to enable a direct three-dimensional observation of cells and their constituents in a close-to-native environment. Although several aspects of cell biology have profited from information obtained by cryo-ET of plunge frozen whole cells preparations or isolated organelles or molecular complexes studies, the majority of cells are too large to freeze using conventional plunge freezing techniques. Therefore, the technique of vitreous cryo-sectioning was introduced to incorporate large cells and pieces of tissue that are too large for conventional freezing and imaging techniques.

As we have seen throughout this thesis, the technique of vitreous cryo-sectioning for electron cryo-tomography is a developing method that was difficult to implement in many EM labs. It requires a high level of dexterity for manipulating the thin ribbon of vitreous cryo sections and transferring it to an EM. In addition, the contamination levels within the microtome coat the equipment, EM grid, and sections with water

contamination in the form of ice crystals. In Chapter 3 we addressed these limitations; section attachment to the support film and contamination within the cryo-ultramicrotome. By altering the output of the electrode, normally used to ionize the surface of the diamond for better surface gliding properties of the vitreous cryo-sections, we developed a method to electrostatically attach sections to the EM support film. We illustrated the advantage of these novel developments by exploring the ultrastructure of the 80S *Saccharomyces cerevisiae* ribosome in a close-to-native, cellular environment. As a result of the novel methods developed, the technique of electron cryo-tomography of vitreous cryo-sectioning is becoming a more widely and reliable method for ultra structural cellular studies. At the current resolution limit of 4-5 nm, large macromolecular complexes like 80S ribosomes are easy to recognize. However as the resolution increases by an order of magnitude, the near future should allow a full comprehensive description of supramolecular architecture within cells.

Although the technique of vitreous cryo-sectioning is gaining importance it's still plagued by section-induced cutting artifacts, as we have seen in Chapter 4. It was thought that vitreous cryo-section induced compression affected the specimen in a homogeneous manner. In other words, if the cell would be compressed by a given value then all its intracellular components would be compressed by the same value. What we observed, however, was at the current resolution limit of 4-5 nm, large macromolecular complexes like the 80S ribosomes remained unaltered by section-induced compression. We concluded that cells and their constituents are not affected by the forces of section-induced compression in a uniform manner. Therefore, the technique of vitreous cryo-sectioning will remain valuable for exploring macromolecular landscapes for large cells and tissues that cannot be imaged *in toto*.

In Chapter 5 we applied the novel techniques from the previous studies to *Escherichia coli* cells that have been infected with bacteriophage T7. The main goal of this study was to visualize the structural components that are assembled by the phage in order to transfer its genome into the host cell, a feat that had never been achieved. In our resulting observations we found three distinct phenotypes of the capsid interacting with the cell. In the study we focused on empty capsids because they have assembled the genome transfer complex and expelled the majority of their genome into the host cell. We observe that at the infection site, the outer membrane of the bacterial envelope is pinched towards the inner membrane. We also observed proteins associated with the outer membrane and also within the envelope of the bacteria. Unfortunately the technique of vitreous cryo-sectioning lacks a protein localization method and therefore we cannot identify the proteins expelled by the bacteriophage. We conclude, however, that the phage must construct a complex of proteins that work together to reduce the distance of the cell membrane in order to transfer its genome.

As we have seen throughout this thesis, visualization by observation is the key to understanding biological ultrastructure and in turn providing evidence for function. For studying the entire spectrum of nanomachines in cells, most of which have dimensions smaller than the macromolecular complexes mentioned in this thesis (like the 80S ribosome and T7 bacteriophage), a number of methodological impediments must be addressed.

The most important aspect of cellular electron cryo-tomography of vitreous cryo-section is sample preparation. A non-intrusive technique, which is still in development, is focused ion-beam milling or micromachining of frozen hydrated

samples[3, 4]. In addition, novel techniques are being developed for self-pressurized freezing[5] that would potentially eliminate the need for introducing high-pressure externally. However both of these methods are still in development.

In addition to specimen preparation advancements, electron microscopy imaging techniques are also evolving. The spatial and temporal coherence of electron sources are improving, which in turn improves the signal-to-noise ratio in subsequent electron cryo-tomography images. The EM stage is more stable in recent machines, which improves tilt series acquisition by less stage-induced movements during tilting. Electron detection is moving into an exciting field of direct detection devices (DDD)[6], which may replace charge coupled device (CCD) cameras that have been routinely used for the past years. This would allow the electrons to be directly detected by the detector rather than passing through a phosphorescent scintillation screen which converts the electrons into a photonic image that can be transferred to the CCD camera by fiber optics or a lens system. Using DDDs reduces the amount of signal saturation and radiation damage of the camera therefore improving the signal-to-noise ratio and sensitivity of the camera.

As we have mentioned through this thesis, currently a technique for localizing proteins within vitreous cryo-sections is lacking. It's a major, maybe even the most considerable drawback of the technique. In recent years a developing technique called correlative light microscopy to electron microscopy[7, 8] is finding a cleaver solution around the absence of a labeling technique. It involves a cryo-light microscope, which is able to image vitreous samples with visible light. Using this method, proteins can be combined with a fluorescent label, frozen, and then screened using LM.

Subsequently the same sample can be imaged using EM and these two images can be correlated into a multi-resolution image in order to find back the protein of interest.

At the other spectrum, high-resolution density maps acquired from X-ray crystallography, NMR, and electron cryo microscopy combined with single particle analysis can be 'docked' into lower resolution EM density maps in order to create a multi-resolution density profile[9] for the macromolecular complexes of interest. This has become a very valuable technique for comparing different imaging modalities and combining each to determine the biological structure more accurately.

In its current state, electron cryo microscopy is a rapidly evolving imaging modality and continuously improving in both image quality and attainable resolution. With new developments the technique will be even more impressive for biological cellular structural determination. In the near future we hope to have the ability to map the spatial organization of various cellular components within the cell, and in a close-to-native state using electron cryo-tomography of vitreous cryo-sections.

References

1. Liu H., Jin L., Koh S.B., Atanasov I., Schein S., Wu L., and Zhou Z.H. 2010 Atomic structure of human adenovirus by cryo-EM reveals interactions among protein networks. *Science* **27**, 1038-43.

2. Zhang X., Jin L., Fang Q., Hui W.H., and Zhou Z.H. 2010 3.3Å cryo-EM structure of a non-enveloped virus reveals a priming mechanism for cell entry. *Cell* **141**, 472-82.

3. Marko M., Hsieh C.H., Schalek R., Frank J., and Mannella C. 2007 Focused-ion-beam thinning of frozen-hydrated biological specimens for cryoelectron microscopy. *Nature Meth.* **4**, 215-217.

4. Rigort A., Bäuerlein F.J., Leis A., Gruska M., Hoffmann C., Laugks T., Böhm U., Elbauer M., Gnaegi H., Baumeister W., and Plitzko J.M. 2010 Micromachining tools and correlative approaches for cellular cryo-electron tomography. *J. Struct. Biol.* **172**, 169-79.

5. Leunissen J.L., and Yi H. 2009 Self-pressurized rapid freezing (SPRF): a novel cryofixation method for specimen preparation in electron microscopy. *J. Microsc.* **235**, 25-35.

6. Milazzo A.C., Moldovan G., Lanman J., Jin L., Bouwer J.C., Klienfelder S., Peltier S., Ellisman M.H., Kirkland A.L., and Xuong N.H. 2010 Characterization of a direct detection device imaging camera for transmission electron microscopy. *Ultramicroscopy* **10**, 744-7.

7. Sartori A., Gatz R., Beck F., Rogort A., Baumeister W., and Plitzko J.M. 2007 Correlative microscopy: bridging the gap between fluorescence light microscopy and cryo-electron tomography. *J. Struct. Biol.* **160**, 135-45.

8. Van Driel L.F., Valentijn J.A., Valentijn K.M., Koning R., and Koster A.J. 2009 Tools for correlative cryo-fluorescence microscopy and cryo-electron tomography applied to whole mitochondria in human endothelial cells. *Eur. J. Cell Biol.* **88**, 669-84.

9. Stewart P.L., Fuller S.D., and Burnett, R.M. 1993 Difference imaging of adenovirus: Bridging the resolution gap between X-ray crystallography and electron microscopy. *EMBO J.* **12**, 2589-2599.

Nederlandse Samenvatting

Titel: Electronen cryo-tomografie (cryo-ET) van vitreuze coupes: Afbeelden van biologische nano-machines in hun cellulaire context.

De onderzoeksrichting van biologische elektronen microscopie (EM) heeft zich ontwikkeld tot een betrouwbare afbeeldingtechniek voor het bestuderen van de ultrastructuur en inhoud van cellen op moleculair, en in sommige gevallen zelfs, atomaire resolutie. Conventionele EM technieken worden overschaduwd door cryogene technieken waarbij een meer natuurlijke monster bereiding gewaarborgd wordt. Verder elimineert de tomografie techniek het projectie probleem van losse 2D afbeeldingen en voegt een derde dimensie toe aan de analyse. De cryogene sample bereidingsmethode in combinatie met tomografie is momenteel de meest geschikte techniek om de levende cel in drie dimensies te bestuderen in een zo natuurlijk mogelijke toestand. Ondanks dat een aantal voorbeelden binnen de celbiologie te noemen zijn waarbij succesvol gebruik is gemaakt van cryo-ET van "plunge-frozen" complete cellen of geïsoleerde cellulaire componenten of moleculaire complexen, blijft de grote meerderheid van de cellen te groot om in hun geheel goed te bevrizen en af te beelden met conventionele technieken. De techniek van cryo-snijden is geïntroduceerd om ook grote cellen en stukjes weefsel, normaale te groot voor conventioneel vriezen en afbeelden, beschikbaar te krijgen.

Zoals beschreven in dit proefschrift, is de het snijden van vitreuze coupes voor toepassing in cryo-ET een techniek in ontwikkeling die moeilijk op de meeste EM laboratoria te implementeren is. Deze techniek vereist een zeer hoge mate van handigheid in het manipuleren van uiterst dunne vitreuze coupes en het verplaatsen

van deze linten naar een EM grid. Bovendien zorgt vervuiling met ijs binnenin het ultramicrotoom ervoor dat alle interne onderdelen, EM grid en coupes bedekt worden met grote ijs kristallen. In hoofdstuk 3 zullen we deze begrenzingen bespreken: bevestiging van de vitreuze coupe aan de EM grid en contaminatie in de microtoom. Door het veranderen van de output van de elektrode, die normaal wordt gebruikt om het oppervlak van het diamant mes te ioniseren zodat de coupes beter glijden, hebben we een methode ontwikkeld om vitreuze coupes elektrostatisch aan een EM grid te bevestigen. We demonstreren de voordelen van deze nieuwe techniek door het 80S *Saccharomyces cerevisiae* ribosome te bestuderen in de bijna natuurlijke cellulaire omgeving. Als gevolg van deze verbeteringen voor de techniek van elektronen cryo-tomografie van vitreuze coupes, kan deze methode betrouwbaarder en op grotere schaal worden ingezet voor het bestuderen van de ultra-structuur van de cel. Bij een resolutie limiet van 4-5 nm zijn grote moleculaire complexen als het 80S ribosoom makkelijk te herkennen. Echter als de resolutie in de toekomst met een orde grootte kan verbeteren zou het ook mogelijk kunnen zijn om een meer omvattende beschrijving van de supramoleculaire architectuur van de cel te kunnen geven.

Ondanks dat de techniek van cryo-snijden vaker wordt toegepast, wordt deze nog steeds geplaagd door artefacten die ontstaan door het snijden, zoals we in hoofdstuk 4 hebben kunnen zien. De geldende theorieën gingen ervan uit dat de, door het snijden geïnduceerde, compressie van de coupe een homogeen proces was. Met andere woorden: als de cel met een bepaalde factor gecomprimeerd wordt, dan worden alle intracellulaire onderdelen met dezelfde factor gecomprimeerd. Wij observeerden echter dat bij de huidige 4-5 nm resolutie, grote macromoleculaire complexen als het 80S ribosoom na het cryo-snijden onveranderd bleef. Wij concludeerden hieruit dat

cellen en hun inhoud op een niet gelijkmatige manier beïnvloed worden door de krachten die tijdens het snijden optreden. Hierdoor blijft de techniek van cryo-snijden een waardevolle techniek om het macromoleculaire landschap van grote cellen en weefsel in kaart te brengen.

In hoofdstuk 5 hebben we de nieuwe technieken, zoals in de voorgaande hoofdstukken besproken, toegepast op T7 bacteriofaag geïnfecteerde E-coli cellen. Het doel van deze studie was om de macromoleculaire componenten, die betrokken zijn bij de injectie van het T7 viraal DNA in de cel, in kaart te brengen; iets wat tot op heden nog nooit is gelukt. In onze waarnemingen hebben we drie verschillende fenotypes gevonden van de interactie tussen kapsel en cel. In dit hoofdstuk focusseren we op de lege kapsels, omdat deze het volledige transfectie complex geassembleerd hebben en het merendeel van de genetische inhoud is uitgescheiden. We constateerden dat het buitenmembraan van de bacterie naar de binnenmembraan gebogen is op de locatie waar de infectie heeft plaatsgevonden. Ook konden we eiwit complexen zien binnen in het celmembraan. Helaas ontbreekt het met de techniek van cryo-snijden nog aan een eiwit lokalisatie methode waardoor we deze membraan geassocieerde eiwitten van de bacteriofaag niet konden identificeren. We concluderen desondanks dat het bacteriofaag een eiwit complex moet construeren dat in combinatie met de verkleinde membraan afstand samen moet werken om het genetisch materiaal te kunnen overdragen.

Zoals we hebben gezien in dit proefschrift is zichtbaar maken door observeren de sleutel voor het begrijpen van de biologische ultrastructuur welke op zijn beurt weer inzicht geeft in de functie. Echter om het gehele spectrum van alle nano-machines in

de cel in kaart te brengen, waarvan vele significant kleiner zijn dan de in dit proefschrift bestudeerde complexen, zal een aantal beperkingen van de methode, zoals vesmeldt in dit proefschrift aangepakt moeten worden.

Curriculum Vitae

Jason Pierson was born on December 21, 1981 in Grand Junction, Colorado, U.S.A. He received his bachelor degree *magna cum laude* from Western State College, Gunnison, Colorado, in 2004, where he majored in Molecular Biology and minored in Chemistry. He spent 2 years, from 2004 to 2006, at the University of Colorado, Boulder, as a professional research scientist under the guidance of Richard McIntosh and Daniela Nicastro. From 2006 to 2010 he worked as a Ph.D. candidate at The Netherlands Cancer Institute, Amsterdam, The Netherlands under the guidance of Professor Peter J. Peters. The work presented in this thesis was performed at The Netherlands Cancer Institute – Antoni van Leeuwenhoek Hospital in Amsterdam, The Netherlands.

In 2010 he accepted a position as Senior Applications Engineer for the Life Science TEM division at the FEI Company in Eindhoven, The Netherlands.

List of Publications

Bertin A., McMurray M., **Pierson J.**, Thai L., McDonald K., Zehr E., Peters P.J., Thorner J., and Nogales E. 2011 Three-dimensional ultrastrucutre of the septin filament network at the bud neck of Saccharomyces cerevisiae. *In Preparation.*

Pierson J., Rodriguez M.J., Fernandez, J.J., Carrascosa J.L., and Peters P.J. 2011 Direct visualization of the The Bacteriophage T7 infection process revealed using cryo electron tomography of vitreous cryo-sections. *In Preparation.*

Pierson J., Vos M., McIntosh J.R., and Peters P.J. 2011 Perspectives on Electron Cryo-Tomography of Vitreous Cryo-Sections. *J. Electron Microsc. In Press.*

Pierson J., Ziese U., Sani M., and Peters P.J. 2011 Exploring Vitreous Cryo-Section Induced Compression at the macromolecular level; 80S yeast ribosomes appear unaffected. Sub-Cellular Level. *J. Struct. Biol.***173(2)***,* 345-349.

Sani M., Houben E.N.G., Geurtsen J., **Pierson J**., De Punder K., Van Zon M., Wever B., Piersma S.R., Jimenez C.R., Daffe M., Appelmelk B.J., Bitter W., Van Wel N.D., and Peters P.J. 2010 Direct visualization by Cryo-EM of the mycobacterial capsular layer: a labile structure containing ESX-1-secreted proteins. *PLoS Pathog.* **5;6(3)**: e1000794.

Pierson J., Fernandez J.J., Bos E., Amini S., Gnaegi H., Vos M., Bel B., Adolfsen F., Carrascosa J.L., and Peters P.J. 2010 Improving the technique of vitreous cryo-sectioning for cryo-electron tomography: Electrostatic charging for section attachment and an Anti-contamination glove box. *J. Struct. Biol.* **169(2)**: 219-225.

Pierson J., Sani M., Tomova C., Godsave S., and Peters P.J. 2009 Towards visualization of nanomachines in their native cellular environment. *Histochem. Cell Biol.* **132**, 253-262.

Milen J., **Pierson J.**, Kvam E., Olsen L., and Goldfarb D.S. 2008 The luminal N-terminus of yeast Nvj1p is an inner nuclear membrane anchor. *Traffic.* **9**, 1653-64.

Pierson J., and Peters P.J. 2008 Immunogold labeling of thawed cryosections. *Methods Cell Biol.* **88**, 131-49.

Van der Wel N., Hava D., Houben D., Fluitsma D., Van Zon M., **Pierson J.**, Brenner M., and Peters P.J. 2007 *M. tuberculosis* and *M. leprae* translocate from the phagolysosome to the cytosol in myeloid cells. *Cell*. **129**, 1287-1298.

Ladinsky M.S., **Pierson J.,** and McIntosh J.R. 2006 Vitreous cryosectioning of cells, facilitated by a micromanipulator. *J. Microscopy*. **224**: 129-134.

Nicastro D., Schwartz C., **Pierson J.**, Gaudette R., Porter M.E., and McIntosh J.R. 2006 The molecular architecture of axonemes revealed by cryoelectron tomography. *Science*. **313**: 944-948.

Nicastro D., Austin II J., Schwartz C., **Pierson J**., Ladinsky M., Staehelin L.A., and McIntosh J.R. 2006 Macromolecular organization of chloroplast membranes. *Microsc. Microanal.* **12(supp 2)**, 38-39.

Nicastro D., Schwartz C., **Pierson J.**, Cho J.C., Giovannoni S.J., and McIntosh J.R. 2006 Three-dimensional structure of the tiny bacterium *Pelagibacter ubique* studied by cryo-electron tomography. *Microsc. Microanal.* **12(supp 2)**, 180–181.

Nicastro D., Austin II J., **Pierson J.**, Gaudette R., Schwartz C., Ladinksy M., Staehelin L.A., and McIntosh J.R. 2005 Visualizing the Macromolecular Organization of Chloroplast Membranes Using Cryo-Electron Tomography. *Microsc Microanal*. **11(Suppl 2)**, 150-151.